

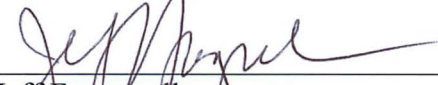
LONG-TERM MONITORING OF GEODYNAMIC SURFACE DEFORMATION
USING SAR INTERFEROMETRY


By


Wenyu Gong

RECOMMENDED:

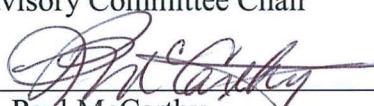

Dr. Donald Atwood


Dr. Jeff Freymueller

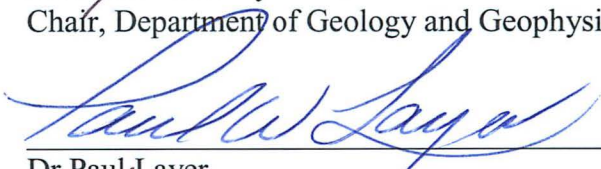

Dr. Zhong Lu

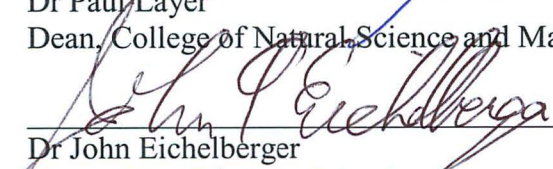

Dr. Peter Webley


Dr. Franz Meyer
Advisory Committee Chair


Dr. Paul McCarthy
Chair, Department of Geology and Geophysics

APPROVED:


Dr Paul Layer
Dean, College of Natural Science and Mathematics


Dr John Eichelberger
Dean of the Graduate School

4/21/14
Date

LONG-TERM MONITORING OF GEODYNAMIC SURFACE DEFORMATION
USING SAR INTERFEROMETRY

A
DISSERTATION

Presented to the faculty
of the University of Alaska Fairbanks

in Partial Fulfillment of the Requirements
for the Degree of

DOCTOR OF PHILOSOPHY

By
Wenyu Gong

Fairbanks, Alaska

May 2014

Abstract

Synthetic Aperture Radar Interferometry (InSAR) is a powerful tool to measure surface deformation and is well suited for surveying active volcanoes using historical and existing satellites. However, the value and applicability of InSAR for geodynamic monitoring problems is limited by the influence of temporal decorrelation and electromagnetic path delay variations in the atmosphere, both of which reduce the sensitivity and accuracy of the technique.

The aim of this PhD thesis research is: *how to optimize the quantity and quality of deformation signals extracted from InSAR stacks that contain only a low number of images in order to facilitate volcano monitoring and the study of their geophysical signatures.*

In particular, the focus is on methods of mitigating atmospheric artifacts in interferograms by combining time-series InSAR techniques and external atmospheric delay maps derived by Numerical Weather Prediction (NWP) models. In the first chapter of the thesis, the potential of the NWP Weather Research & Forecasting (WRF) model for InSAR data correction has been studied extensively. Forecasted atmospheric delays derived from operational High Resolution Rapid Refresh for the Alaska region (HRRR-AK) products have been compared to radiosonde measurements in the first chapter. The result suggests that the HRRR-AK operational products are a good data source for correcting atmospheric delays in spaceborne geodetic radar observations, if the geophysical signal to be observed is larger than 20 mm. In the second chapter, an advanced method for integrating NWP products into the time series InSAR workflow is developed. The efficiency of the algorithm is tested via simulated data experiments, which demonstrate the method outperforms other more conventional methods. In Chapter 3, a geophysical case study is performed by applying the developed algorithm to the active volcanoes of Unimak Island Alaska (Westdahl, Fisher and Shishaldin) for long term volcano deformation monitoring. The volcano source location at Westdahl is determined to be approx. 7 km below sea level and approx. 3.5 km north of the Westdahl

peak. This study demonstrates that Fisher caldera has had continuous subsidence over more than 10 years and there is no evident deformation signal around Shishaldin peak.

Table of Contents

	Page
Signature Page	i
Title Page	iii
Abstract.....	v
Table of Contents.....	vii
List of Figures.....	xi
List of Tables	xiii
Acknowledgements.....	xv
Introduction.....	1
Reference	4
Chapter 1 Performance of the High Resolution Atmospheric Model HRRR-AK for Correcting Geodetic Observations from Spaceborne Radars	5
1.1 Abstract.....	5
1.2 Introduction.....	6
1.3 Description of the Observations and Study Areas.....	8
1.3.1 Radiosonde Observations (RAOBS)	9
1.3.2 HRRR-AK Products and the Weather Research and Forecasting (WRF) Model ...	10
1.3.3 Climate Conditions of Study Areas	10
1.4 Theory of Atmospheric Effects on Radar Remote Sensing and Its Applications.....	11
1.4.1 From Atmospheric Observations to Total Signal Delay.....	11
1.4.2 Relevant Atmospheric Parameters from a Microwave Remote Sensing Perspective	14
1.5 Performance Analysis of HRRR-AK Predictions.....	15
1.5.1 Applied Mathematical Model for Comparative Analysis.....	15
1.5.1.1 Assessment of the Accuracy of Precipitable Water Vapor Predictions.....	16
1.5.1.2 Assessment of the Accuracy of Hydrostatic Delay Predictions	18
1.5.2 Results of Experiments	18

1.5.2.1 Performance of HRRR-AK as a Function of Model Lead Time	18
1.5.2.2 Statistics of HRRR-AK Products With Seasonal Effects	22
1.5.2.3 Performance of HRRR-AK Products as a Function of Time of Day.....	25
1.6 Discussion.....	27
1.6.1 Comparison with other NWP products in delay related components prediction.....	27
1.6.2 Summary of findings	28
1.6.3 Error sources in methodology of assessment.....	30
1.7 Conclusions and Suggestions	32
1.8 Acknowledgements.....	32
1.9 References.....	32
Chapter 2 Robust Atmospheric Filtering of InSAR Data Based on Numerical Weather Prediction Models	53
2.1 Abstract.....	53
2.2 Introduction.....	53
2.3 Spatial Variance of Time Series Interferograms.....	57
2.3.1 Relevant Background on InSAR Time Series Processing.....	57
2.3.2 Spatial Variance of Pre-processed Interferograms	60
2.3.2.1 Theory of Spatial Variance Composition	60
2.3.2.2 Stochastic Constraints for Atmospheric Filter Design	60
2.4 The Performance of NWPs in Predicting Atmospheric Phase Variance	61
2.4.1 Atmospheric Spatial Variance and Empirical Model	61
2.4.2 Real Data Analysis	62
2.4.2.1 Study Areas.....	62
2.4.2.2 APSs Isolation from Interferograms and NWP Products	63
2.4.2.3 Linear Regression Analysis of Spatial Atmospheric Variance.....	64
2.4.2.4 Variability of the Linear Scale Factor \hat{a}	64
2.4.3 Sub-conclusions.....	67
2.5 A Robust Optimal Atmospheric Phase Filter Based on NWP Data	67
2.5.1 Optimal Atmospheric Phase Filtering through Correlation Maximization	68

2.5.2 Performance Assessment Using Synthetic Data.....	69
2.5.2.1 Synthetic Data Preparation	69
2.5.2.2 Synthetic Data Processing Using the Optimal Atmospheric Phase Filter	71
2.5.3 Assessment of convergence properties	72
2.6 Conclusions.....	73
2.7 Acknowledgements.....	74
2.8 References.....	74
Chapter 3 Subtle Motion Long Term Monitoring of Unimak Island from 2003 to 2010 by Advanced Time Series SAR Interferometry	87
3.1 Abstract.....	87
3.2 Introduction and Motivation	88
3.3 Unimak Island and Its Previous Geodetic Studies.....	90
3.4 Techniques, Background and Data Processing.....	91
3.4.1 Advanced Time Series InSAR Processing Strategy	92
3.4.1.1 Phase Components Decomposition	92
3.4.1.2 Advanced Atmospheric Signal Mitigation	93
3.4.2 Small Baseline Time Series InSAR.....	95
3.5 Geophysical Study Based on InSAR Result.....	96
3.5.1 Comparison with In Situ Geodetic Measurement.....	96
3.5.1.1 Comparison with GPS Measurement Before 2001	97
3.5.1.2 Comparison with GPS Measurement After 2008	98
3.5.2 Comparison with Different PSI Parameter Setting.....	101
3.6 Source Model Inversion of Westdahl Volcano.....	102
3.7 Geophysical Discussion.....	107
3.8 Summary and Conclusions	109
3.9 Acknowledgement	110
3.10 References.....	110
Chapter 4 Conclusion and Future Work	129
4.1 Conclusions.....	129

4.2	Future Work and Improvements	131
4.3	References	133

List of Figures

	Page
Figure 1.1: Locations of the radiosonde stations across Alaska that are used in this research.....	39
Figure 1.2: Statistical analysis results of the effect of different HRRR-AK model lead times on the predictability of PWV at each of the test sites.	40
Figure 1.3: Statistical analysis results of the effect of different HRRR-AK model lead times on the accuracy of hydrostatic delay predictions at the five test sites ..	41
Figure 1.4: Examples of linear regression of HRRR-AK vs. RAOBS data for PWV and hydrostatic delay.....	42
Figure 1.5: Examples of vertical profiles of atmospheric parameters extracted from PABR summertime data pairs.	43
Figure 2.1: Regression lines per test site.	79
Figure 2.2: Linear relationship between DEM standard deviation σ_{DEM} and estimated scale factor \hat{a}	80
Figure 2.3: Empirical $(\sigma_{i,atm}^2)_{ifg,pred}$ with the predicated scale factor \hat{a} and the external $(\sigma_{i,atm}^2)_{nwp}$ vs. InSAR contained $(\sigma_{i,atm}^2)_{ifg}$	81
Figure 2.4: Example Synthetic data (black cross markers).....	82
Figure 2.5: Comparison of σ_i^2 , $\sigma_{i,defo}^2$ and its estimates $(\sigma_i^2)_{lp_ideal}$ and $(\sigma_i^2)_{lp_T}$	83
Figure 2.6: Dependence of convergence rate of the optimal phase filter algorithm on the quality of $(\sigma_{i,s-atm}^2)_{nwp}$	84
Figure 3.1: The location of the three studied volcanoes, Westdahl, Fisher and Shishaldin, and historical/current GPS sites in Unimak Island.....	114
Figure 3.2: Deformation time series from 2003 to 2010 reconstructed from PSI data processing	115
Figure 3.3: Velocity map provide from both PSI and SBAS method.....	116

Figure 3.4: Subsidence observed in the center of Fisher caldera.....	117
Figure 3.5: Shift in velocity computed from GPS and PSI with different spatial reference	118
Figure 3.6: Comparison of GPS and PSI LOS motion time series measurements around Westdahl.....	119
Figure 3.7: Comparison of GPS and PSI LOS motion time series measurements close to Shishaldin.....	120
Figure 3.8: The result of point source model inversion.....	121
Figure 3.9: Volume change estimates and temporal model.....	122
Figure 3.10: Magma refilling processing after an eruption of Westdahl.....	123

List of Tables

	Page
Table 1.1: Statistical analysis of one way zenith delay for several test sites in Alaska at 6 hour and 24 hours model lead time settings.	44
Table 1.2: RMS(bias) of difference (HRRR-AK minus RAOBS) at 6 hour and 24 hours model lead time settings.	45
Table 1.3: Statistical analysis of one way zenith delay of summer cases at 12 hour model lead time setting.....	46
Table 1.4: Statistical analysis of one way zenith delay of winter cases at 12 hour model lead time setting.....	47
Table 1.5: RMS (bias) of difference for winter and summertime acquisitions.	48
Table 1.6: Performance analyzes of daylight effects to simulation, 12UTC-night-time. .	49
Table 1.7: Performance analyzes of daylight effects to simulation, 00UTC-day-time. ...	50
Table 1.8: RMS (bias) of difference in different daylight condition cases.....	51
Table 1.9: Statistics adapted from previous studies of different NWP products in predicting delay-related parameters.	52
Table 2.1: Results of linear regression of spatial variance	85
Table 2.2: Results of linear regression of spatial variance using WRF 3.5 and two different model lead times for test sites Hawaii and Mexico City.	86
Table 3.1: Single master interferogram information.....	124
Table 3.2: GPS velocity (mm/year) in LOS direction during 1998 to 2001 and PSI velocity during 2003 to 2010.....	125
Table 3.3: Statistical analysis of the displacement residuals from PBO GPS and PSI in the overlap dates.....	126
Table 3.4: Time series of volcano source model inversion result from 2004 to 2010 with fixed horizontal location only.....	127
Table 3.5: Time series of volcano source model second inversion with fixed depth and fixed horizontal location.....	128

Acknowledgements

I had so much support from many people from research to daily life. Without you, I wouldn't have made it.

Foremost, I would like to express my greatest gratitude to my supervisor Dr. Franz Meyer, for his guidance, support, and encouragement. Discussion with him is always a source of inspiration and brought me a lot of fun. I express my thanks to Dr. Zhong Lu; it was his encouragement and reference letter that introduced me to UAF and I thank him for being my committee member. I would like to express thanks to my other committee members Dr. Jeff Freymueller, Dr. Peter Webley and Dr. Donald Atwood for their support in my research and guidance in the study. My gratitude is sent to my committee members again, for their patience to read through my thesis and their efforts to improve its quality.

I would like to thank Dr. Don Morton, Dr. Ramon Hanssen and Dr. Shizhuo Liu for providing me data, project collaboration and support on paper writing. I thank Nico Adam, Dr. Richard Bamler and Dr. Michael Eineder for hosting the trip to DLR, for helpful discussions, and for bringing me to the Oktoberfest. Also my thanks are sent to Dr. Chang Wook Lee for research collaboration and help when I was in Portland.

Also, I want to thank Yuning Fu, Fuhong Liu and Xuanye Ma for being patient in answering my numerous questions on geodesy, weather forecasting and mathematics. Furthermore, I want to thank all my former and present colleagues in the remote sensing group, geodesy group and the Geology & Geophysics department.

I also would like to thank Sarah Henton De Angelis for bringing me to the running activity, from which I benefit both physically and mentally. Thank David McAlpin for answering my all kinds of questions from geology to history and from Alaska to Florida. Also, I express my thanks to Judith Levy for great Alaskan adventures, Antje Thiele for the great memory of your Fairbanks stays, and Xiaoying Cong for her advice in many aspects and encouragements. Thank you, my Chinese girls from UAF Qingjia Li, Jinghui

Zheng, Yangqing Liu, Ting Xiao, Rong Zou and Yun Wang. They all have been a great accompaniment for these years.

I want to thank my boyfriend Ran Li for a decade of support. Finally, I want to devote this thesis to my parents in China with my deep gratitude for bringing me to the world, and everything they have done to raise me up.

Introduction

The main focus of this thesis research is to improve radar interferometry techniques for precision monitoring of geodynamic signals. Specifically, the research will focus on volcano deformation, which is one of three precursor signals indicating the potential of upcoming eruptions [Dzurisin, 2007].

Many volcanic eruptions are preceded by pronounced ground deformation in response to increasing pressure from magma chambers, or to the upward intrusion of magma [Dvorak and Dzurisin, 1997]. These phenomena are one of the main precursor indicators before an eruption begins. The other two indicators are deep and long period seismic signals and changes in magmatic carbon dioxide emission rates [Dzurisin, 2003]. Exact knowledge of the spatial surface deformation signal helps in determining the location and shape of the pressure source underneath the surface, allows quantification of the parameters of a volcano source model in a parameter inversion, and provides information about the internal eruption physics and dynamics of a volcano [Segall, 2010].

With the development of classical geodetic procedures, systematic measurements of ground deformation were initiated in the early 20th century in USA and Japan [Dzurisin, 2007]. In the decades, since the advent of spaceborne remote sensing, continued technological developments have turned Synthetic Aperture Radar interferometry (InSAR) remote sensing into a reliable and widely used geodetic technique that provides highly accurate observations of surface deformation at volcanoes in remote areas with high spatial resolution and large spatial coverage. Due to its independence from daylight and weather conditions, its predictable repetition cycle, and global observation strategy, InSAR distinguishes itself as a suitable tool to conduct a long time deformation monitoring over volcanoes across the world. InSAR represents uplift or subsidence movement associated with eruptions or magma intrusions as a phase change between repeated acquisitions that can be captured in interferograms. Advanced InSAR techniques can extract these motion signals with cm-accuracy [Hanssen, 2001], which can provide significant inputs for studying magma dynamics.

The value and applicability of InSAR for geodynamic monitoring problems is limited by the influence of temporal decorrelation, especially for non-urban areas. It is due to the unstable and complex ground coverage and electromagnetic path delay variations when signal propagates through atmosphere, both reducing the sensitivity and accuracy of the technique. Particularly problematic are seasonal changes of climatic conditions that can be significant on tall volcanic edifices and often limit the amount of useful data to images from similar seasons in order to make volcano monitoring feasible in sub-arctic environments [Lu and Freymueller, 1998].

This study will focus on *decorrelation* mitigation by advanced InSAR techniques and mitigation of *atmospheric artifacts* by incorporating external atmospheric fields, for the purpose of reconstructing the geodynamic motion history. In theoretical analyses and case studies, improvements in accuracy and precision of the extracted deformation signals will be quantified. Finally, the improved extracted deformation information will be used to quantify the parameters of volcano source models at selected study sites and evaluate their evolution.

In the first chapter, I made a quantitative study on the accuracy of using operational Numerical Weather Prediction (NWP) products for signal delay correction in satellite radar geodetic remote sensing. The study focuses on the temperate, subarctic and Arctic climate regions due to the prevalence of relevant geophysical signals in these areas, e.g. Alaskan volcanoes, and on High Resolution Rapid Refresh over the Alaska region (HRRR-AK) model atmospheric delay products. The performance of the HRRR-AK products for correcting absolute atmospheric range delays in radar signals is assessed by comparing them to radiosonde observations. The study suggests that the HRRR-AK operational products are a good data source for spaceborne geodetic radar observations atmospheric delay correction, if the geophysical signal to be observed is larger than 20mm.

In Chapter 2, I analyze the capability of NWP models in producing realistic information about the statistical properties of atmospheric phase signals in InSAR data. The main achieved findings are: (1) that NWPs are able to robustly predict statistical

properties of atmospheric phase screens; and (2) that NWP's underestimate these statistical properties by a scaling factor that depends on the area's surface topography but not on its climatic conditions. Based on these findings, a new concept for atmospheric mitigation, using NWP-derived statistical parameters to condition the design of an optimal atmospheric phase filter, is developed. The study shows that this filter concept outperforms other more conventional filtering methods.

In the final chapter, I processed a seven year time series of Environment Advanced Synthetic Aperture Radar (ENVISAT ASAR) radar images over Unimak Island, Alaska in order to analyze volcanic signatures on this island. The method developed in Chapter 2, is applied for data processing. Data processing was assisted by using auxiliary numerical predicted radar signal delay maps to optimally distinguish the deformation signals from atmospheric contaminations. The reconstructed deformation time series maps are compared with historical and current GPS measurements as well as Small Baseline Subset (SBAS) InSAR technique results for quality assessment and geophysical interpretation. The results show that Westdahl Volcano is still inflating but at a lower rate than in the period before 2001. It also indicates that the volcano source is located approx. 3.5 north of Westdahl peak, which agrees with previous GPS results [*Mann and Freymueller, 2003*]. The deformation found at Fisher caldera is linear and constant in time. There is no evidence of deformation found around Shishaldin peak, but unexplained deformation signals were observed about east of Shishaldin and over the Tugamak range.

In the study of Chapter one, the HRRR-AK data was provided by the co-author Dr. Don Morton. My major contributions are on HRRR-AK data analyzing and statistical modeling. In the second chapter, the SAR data was provided by Dr. Ramon Hanssen and a part of the InSAR and NWP data were processed and analyzed by Dr. Shizhuo Liu. My contributions include InSAR and NWP data processing, the statistical modeling and the algorithms design and corresponding evaluation of the optimal atmospheric phase filter in time series InSAR techniques. In the third chapter, Dr. Chong Wook Lee processed SAR data with the SBAS approach. I was mainly working on the Persistent Scatterer InSAR (PSI) data processing with the optimal atmospheric filter developed in the second

chapter, comparing PSI measurements with results from SBAS and validating with historical and current GPS records, as well as the geophysical interpretation and inversion. All the co-authors for these three manuscripts have contributed to paper revision and putted effort into improving the quality of presented researches.

References

- Dvorak, J. J., and D. Dzurisin (1997), Volcano geodesy: The search for magma reservoirs and the formation of eruptive vents, *Review of Geophysics*, 35(3), 343-384.
- Dzurisin, D. (2003), A comprehensive approach to monitoring volcano deformation as a window on the eruption cycle, *Review of Geophysics*, vol 41, pg 1001 , 2003, 41(2).
- Dzurisin, D. (2007), *Volcano deformation : geodetic monitoring techniques*, xxxv, 441 p. pp., Springer-Praxis Berlin; New York; Chichester, UK.
- Hanssen, R. (2001), *Radar Interferometry: Data Interpretation and Error Analysis*, 1 ed., Kluwer Academic Publishers.
- Lu, Z., and J. Freymueller (1998), Synthetic aperture radar interferometry coherence analysis over Katmai volcano group, Alaska, *Journal of Geophysical Research*, 103(B12), 29887-29894.
- Mann, D., and J. Freymueller (2003), Volcanic and tectonic deformation on Unimak Island in the Aleutian Arc, Alaska, *Journal of Geophysical Research*, 108(B2), 2108.
- Segall, P. (2010), *Earthquake and volcano deformation*, xxiii, 432 pp, Princeton University Press, Princeton, N.J.

Chapter 1 Performance of the High Resolution Atmospheric Model HRRR-AK for Correcting Geodetic Observations from Spaceborne Radars ¹

1.1 Abstract

Atmospheric phase delays are considered to be one of the main performance limitations for high-quality satellite radar techniques, especially when applied to ground deformation monitoring. Numerical weather prediction (NWP) models are widely seen as a promising tool for the mitigation of atmospheric delays as they can provide knowledge of the atmospheric conditions at the time of Synthetic Aperture Radar (SAR) data acquisition. However, a thorough statistical analysis of the performance of using NWP production in radar signal correction is missing to date. This study provides a quantitative analysis of the accuracy in using operational NWP products for signal delay correction in satellite radar geodetic remote sensing. The study focuses on the temperate, subarctic and Arctic climate regions due to a prevalence of relevant geophysical signals in these areas. In this study, the operational High Resolution Rapid Refresh over the Alaska region (HRRR-AK) model is used and evaluated. Five test sites were selected over Alaska (AK), USA, covering a wide range of climatic regimes that are commonly encountered in high latitude regions. The performance of the HRRR-AK NWP model for correcting absolute atmospheric range delays of radar signals is assessed by comparing to radiosonde observations. The average estimation accuracy for the one-way zenith total atmospheric delay from 24 hour simulations was calculated to be better than ~14 mm. This suggests that the HRRR-AK operational products are a good data source for spaceborne geodetic radar observations atmospheric delay correction, if the geophysical signal to be observed is larger than 20 mm.

¹ Gong, W., F. J. Meyer, P. Webley, and D. Morton (2013), Performance of the high resolution atmospheric model HRRR-AK for correcting geodetic observations from spaceborne radars, *Journal of Geophysical Research: Atmospheres*, 2013JD020170.

1.2 Introduction

Fine resolution and repeatable geodetic measurements are required to precisely measure movements and deformations of the Earth's surface that are triggered by various geophysical phenomena including volcanoes [Dzurisin, 2007; Lu *et al.*, 2010], permafrost [Liu *et al.*, 2010], earthquakes [Segall, 2010; Wei *et al.*, 2010], tidal motion [Eineder *et al.*, 2011], and ground water extraction [Kampes, 2005]. Precise knowledge of the magnitude and spatial patterns of these surface deformation signals allows determination and quantification of geophysical parameters [Segall, 2010] and will improve our understanding of the dynamics of the earth's interior [Sleep and Fujita, 1997].

Despite a large number of successful case studies, the performance and applicability of synthetic aperture radar (SAR) as a geodetic measurement tool is limited by the influence of electromagnetic path delay variations when the signal is propagating through the atmosphere [Richter and Hitney, 1980]. While atmospheric delays can be decomposed into two parts, tropospheric delays and ionospheric delay [Hanssen, 2001; Resch, 1980], this study is focusing on the mitigation of tropospheric delays only.

The majority of the research on atmospheric mitigation methods for geodetic radar remote sensing observations has so far focused on the correction of Interferometric SAR (InSAR) observations. InSAR techniques measure the spatial and temporal derivative of the SAR signal phase in order to extract surface deformation. Due to the double differencing procedure, atmospheric artifacts in InSAR data are mainly caused by the spatio-temporal variation of atmospheric water vapor while other atmospheric delay components largely cancel out. Mitigation methods often rely on water vapor measurements from external sources, such as dense networks of Global Positioning System (GPS) stations [Li, Fielding, Cross, *et al.*, 2006; Onn and Zebker, 2006; Xu *et al.*, 2011] and spaceborne multispectral scanners [Li *et al.*, 2009]. Alternative methods are using time series of SAR imagery to filter atmospheric artifacts based on the spatio-temporal statistics of atmospheric water vapor distributions [Berardino *et al.*, 2002; Ferretti *et al.*, 2001]. Besides InSAR, geodetic observations have also been derived using tracking techniques or the recently developed absolute ranging method. Tracking

methods identify and track features or noise patterns through sequences of images to determine surface motion. With high resolution radar systems, tracking methods [Eineder *et al.*, 2011] can detect range changes at the centimeter level, requiring accurate atmospheric correction to produce reliable surface motion measurements. The absolute ranging technique has become applicable since the launch of the TerraSAR-X radar system and allows for the retrieval of precise absolute range measurements between satellite and ground. Absolute ranging can measure geodetic signals like tectonic deformation from only one image but requires precise correction for absolute atmospheric delay for the method to succeed [Eineder *et al.*, 2011].

In the past few years, Numerical Weather Prediction (NWP) simulations have become a novel data source for atmospheric correction of remote sensing data. Many studies have analyzed the merit of NWPs for atmospheric correction of InSAR data [Foster *et al.*, 2013; Fournier *et al.*, 2011; Gong *et al.*, 2010; Webley *et al.*, 2002] and have found that NWPs are often able to correct for effects related to atmospheric stratification [Liu and Hanssen, 2009]. However, results are inconclusive when it comes to correcting for atmospheric turbulence patterns. While only few studies have addressed the correction of atmospheric delays for absolute ranging and tracking techniques, some of them demonstrated up to 3.2 cm ranging accuracy in slant range when using European Centre for Medium-Range Weather Forecasts (ECMWF) for absolute range phase correction [Cong *et al.*, 2012]. In all studies, more thorough statistical analyses are necessary to quantify the performance of NWPs under a range of atmospheric conditions. The goal of our study is the qualification and quantification of the correction performance of the High Resolution Rapid Refresh (HRRR) over the Alaska region (HRRR-AK) based on the Weather Research and Forecasting (WRF) model. HRRR-AK performance is analyzed by a comparison of its predictions to a large number of radiosonde observations (RAOBS) acquired over five test sites in high-latitude regions twice a day and for sixteen months. Predictions and observations are compared using statistical methods, and differences between them are analyzed for their dependence on the model lead time, time of day, season, as well as geographic and climatologic properties of the test sites. Study

areas have been defined within Alaska, USA, for three reasons: (1) Alaska provides a large number of geophysical signals including volcanoes, glacier and tectonic motion and is therefore a natural test site for geodetic observations from space; (2) as arctic and subarctic environments are more and more becoming the focus of many radar-based remote sensing studies, this study is relevant to a large number of geophysical research questions; and (3) with the HRRR-AK, an operational high-resolution NWP is available for Alaska. HRRR-AK is the Alaska-centered adaptation of the 48 contiguous United States High Resolution Rapid Refresh (HRRR) operational atmospheric model. The HRRR-AK model is developed, maintained and run at the University of Alaska Fairbanks' Arctic Region Supercomputing Center (ARSC) [ARSC, 2012] and model outputs are publicly available (<http://weather.arsc.edu/HRRR/>).

A short description of RAOBS and the fundamental features of HRRR-AK, as well as the climate conditions of study sites are introduced in Section 1.3. A brief description of converting atmospheric physical parameters into total atmospheric delay and Precipitable Water Vapor (PWV) delay is provided in Section 1.4. In Section 1.5, the experiments focusing on determining the accuracy of using HRRR-AK products for atmospheric signal mitigations in various radar techniques are presented and discussed. The last sections discuss and summarize the presented work, compare results of this study to other related findings, and draw conclusions on the performance of operational HRRR-AK data for radar signal delay correction.

1.3 Description of the Observations and Study Areas

The HRRR-AK simulations and radiosonde data used in this study cover a time span from June 2010 to September 2011. In this section, it will provide a brief introduction to the radiosondes used in this study; the principles of HRRR-AK simulations together with their set-up environment and parameterization; climatological details and locations of five test sites across Alaska chosen for this research that cover a wide range of climatic conditions, which are routinely encountered in polar and sub-polar regions.

1.3.1 Radiosonde Observations (RAOBS)

Radiosondes provide in-situ observations of the vertical profile of many meteorological variables during their rise through the atmosphere. These variables include atmospheric pressure, temperature, wind speed, and relative humidity [NWS, 2010]. Typically, radiosondes are released twice a day at 00:00 UTC (15:00 Alaska Standard Time (AKST) in winter, 16:00 Alaska Daylight Time (ADKT) in summer) and 12:00 UTC (03:00 AKST and 04:00 ADKT) [NWS, 2010]. In our research, radiosonde data was retrieved from the University of Wyoming's Department of Atmospheric Science [UW, 2012].

The locations of the five radiosonde launch sites used in this study are shown in Figure 1.1 with their corresponding International Civil Aviation Organization (ICAO) location codes (four letter code). From north to south, site PABR is located north of Barrow, site PAFA is located southwest of Fairbanks, PANC is to the west of Anchorage, PASN is located in the southeast of St. Paul Island, and PANT is southwest of Annette Island. Two types of radiosondes were used during our studied time span. VIZ II B radiosondes were used at PABR (indicated by a gray dot in Figure 1.1), while the rest of our test sites (indicated by black dots in Figure 1.1) were using the VIZ Mark IIs GPS microsonde (VIZ Mark IIs for short in Figure 1.1) [Morton and Malingowski, 2012]. Both types of radiosondes are very similar in design and are using the same pressure, temperature and humidity sensors for recording the atmospheric conditions. Due to this similarity, we will refer to all radiosondes as VIZ radiosondes in the remainder of the paper.

The radiosonde types used in this study have been reported to produce PWV with an accuracy of $\sigma_{RAOBS,PWV} = 1-2\text{ mm}$ [Niell *et al.*, 2001]. In Arctic regions, the reported accuracy of PWV measurements in Barrow, Alaska is $\sigma_{RAOBS,PWV} \leq 1\text{ mm}$ by comparing VIZ observation to GPS products [Mattioli *et al.*, 2007]. Several studies have reported inaccurate records of VIZ radiosondes in the upper troposphere, when temperatures are extremely cold [Wang and Zhang, 2008]. For InSAR observations, where atmospheric

delay signals are primarily dependent on water vapor distributions, measurement errors in the upper troposphere can be largely ignored due to the low proportion of total water vapor in upper troposphere [Chen *et al.*, 1999]. England *et al.* [1993] have observed distinctive differences in moisture measurements above 8000 meters above sea level (ASL) among different radiosonde systems. Hence, only the first 8000 meters ASL of radiosonde data are used for the NWP performance analysis in this research.

1.3.2 HRRR-AK Products and the Weather Research and Forecasting (WRF) Model

The HRRR-AK, which is publicly available for Alaska, <http://weather.arsc.edu/HRRR/>, is initialized with the highly assimilated Rapid Refresh (RAP) data and uses the WRF 3.2 system for 24 hour atmospheric condition forecasting with 3 km lateral resolution and 51 vertical layers [ARSC, 2012]. The WRF model is a numerical weather prediction and atmospheric simulation system that has been designed for advancing the understanding and prediction of mesoscale weather systems both in research and in operational applications [Skamarock *et al.*, 2008]. WRF belongs to the latest generation mesoscale weather prediction models. Four 24-hour HRRR-AK forecasts are produced by ARSC per day providing atmospheric conditions at user defined time steps [ARSC, 2012]. The meteorological initialization data, RAP, is provided by National Oceanic and Atmospheric Administration (NOAA) and is an hourly updated operational weather prediction system covering North America with 13-km lateral resolution and 50 vertical layers [NOAA, 2012]. The 11 km Alaska North American Mesoscale (NAM) model has also been utilized to extend lateral boundary conditions beyond the RAP forecast period. The combination of availability, high lateral and vertical resolution, and rapid temporal refresh rates makes HRRR-AK the ideal data set for model-based atmospheric correction of radar remote sensing data in an operational setting.

1.3.3 Climate Conditions of Study Areas

The spatial distribution of the radiosonde test sites was chosen to represent a wide

range of climate/weather conditions in Arctic and subarctic environments in order to provide a performance assessment of HRRR-AK that are representative for most high latitude regions. The sites provided a range of meteorological challenges that allowed for testing the robustness of HRRR-AK predictions for several climatic regions.

According to the classification by the Alaska Climate Research Center (ACRC) [Bieniek *et al.*, 2012], Alaska can be generally divided into four climate regions as highlighted in Figure 1.1 (gray capital letters). These are (i) the Arctic region, (ii) the interior region, (iii) the west coast region, and (iv) the south central/south east region. The dominating factor that differs among these climate regions is the seasonal change of solar radiation, atmospheric moisture conditions, the local topography, and the presence or absence of nearby ocean bodies [Benson *et al.*, 1983]. Stafford, *et al.*[2000] summarized the climate properties of the above mentioned four climate zones. They state that the Arctic climate region, where station PABR is located, can be considered as the coldest and driest with average annual temperatures below 0 °C and the majority of precipitation coming from snow [Searby, 1968]. The interior climate region where Station PAFA is located is characterized as a highly continental climate of meteorological extremes, with high temperatures ranging from below -40 °C in the local winter to above +30 °C during local AK summer. PASN is located in the Bering Sea, which is considered to be a transitional zone of continental and coastal climates. The two radiosonde stations PANC and PANT are both located in the south central/south eastern climate region that are reported generally wet all year with annual mean temperatures between 0°C - 5°C and are affected by both oceanic and subarctic climates [Peel *et al.*, 2007].

1.4 Theory of Atmospheric Effects on Radar Remote Sensing and Its Applications

1.4.1 From Atmospheric Observations to Total Signal Delay

For microwave remote sensing in geodetic applications, the atmosphere is considered an error source that biases measurements of the range between sensor and earth surface. The atmospheric delay L_{los} that is experienced by a microwave signal is equivalent to the integral of refractivity along the signal's line-of-sight (LOS) [Smith and Weintraub,

1953]. Under the assumption of a spatially smooth atmosphere, L_{los} can be calculated from the zenith delay L using the signal's incidence angle θ_{inc} according to $L_{los} = L / \cos \theta_{inc}$. As radiosondes measure the vertical profile of atmospheric conditions, vertical delay measurements L are used to assess the performance of HRRR-AK through a direct comparison of $L_{HRRR-AK}$ and L_{RAOBS} .

The zenith delay L can be further numerically approximated as a function of pressure (P , in hPa), water vapor pressure (e , in hPa) as well as temperature (T , in K) integrated along height h [Smith and Weintraub, 1953], resulting in Eq. (1.1), where $k_1 = 77.6 k/hPa$, $k'_2 = 23.3 k/hPa$, and $k_3 = 3.75 \times 10^5 k^2/hPa$ [Smith and Weintraub, 1953; Davis *et al.*, 1985]. The vapor pressure e can be computed from water vapor mixing ratio Q and pressure P [UK Meteorological Office, 1991], both of which are standard outputs of HRRR-AK and RAOBS.

$$L = 10^{-6} \int \left(\underbrace{k_1 \frac{P}{T}}_{Hydro.} + \underbrace{k'_2 \frac{e}{T} + k_3 \frac{e}{T^2}}_{Wet} \right) dh \quad (1.1)$$

The first term on the right side of Eq. (1.1) is the so-called *hydrostatic* delay (hydro., L_{hydro}), while the second and third term in Eq. (1.1) are the *wet* delay terms (L_{wet}) related to the presence of water vapor. L_{hydro} in the zenith direction can alternatively be calculated from the local gravity g_m in m/s^2 , and surface pressure P_s in hPa as shown in Eq. (1.2) [Davis *et al.*, 1985; Hanssen, 2001], in which $R_d = 287.053 [J \cdot K^{-1} kg^{-1}]$. $L_{hydro} \approx 2.27 \cdot P_s$ in mm with average local gravity $g_m \sim 9.8 m/s^2$ in Alaska. Eq. (1.2) utilizes the fact that the vertical atmospheric profiles of pressure P and temperature T are known and stable. This allows us to calculate L_{hydro} without requiring numerical integration, reducing the required computational effort.

$$L_{hydro} = 10^{-6} \int k_1 \frac{P}{T} dh = 10^{-6} \cdot k_1 \cdot \frac{R_d}{g_m} \cdot P_s \quad (1.2)$$

An alternative method of calculating the zenith wet delay (ZWD) term L_{wet} in Eq. (1.1) is using PWV fields combined with a projection function Π . In Eq. (1.3) Π can be considered a dimensionless factor that is mapping PWV into zenith delays. Values for Π were determined from laboratory experiments [Bevis *et al.*, 1992]. Computing L_{wet} via the projection function makes it easier to compare our findings to findings of other researchers that have often analyzed PWV fields from various sources and their potential for atmospheric correction. For instance, when cloud coverage is not obstructing the atmosphere underneath, PWV fields obtained from multi-spectral remote sensing, e.g. Moderate Resolution Imaging Spectroradiometer (MODIS) and Medium Resolution Imaging Spectrometer (MERIS), were used to correct microwave remote sensing signal delays in previous studies [Li, Muller, Cross *et al.*, 2009; Meyer *et al.*, 2008].

We integrate vapor pressure and temperature in the vertical to obtain PWV and convert PWV to L_{wet} via Eq. (1.3). Relying on PWV, rather than the vapor and temperature profiles, ensures that the methods applied here can be used globally for any NWP or satellite derived atmospheric information, which often only provide PWV and not profile measurements.

$$L_{wet} = 10^{-6} \int (k_2' \frac{e}{T} + k_3 \frac{e}{T^2}) dh = \Pi^{-1} PWV \quad (1.3)$$

PWV is derived from predictions of the HRRR-AK system via Eq. (1.4) and the performance of these predictions is analyzed through a comparison to RAOBS [Hanssen, 2001; Bevis *et al.*, 1992].

$$PWV = \frac{1}{\rho_l} \int \left(\frac{e}{R_v \cdot T} \right) \cdot dh \quad (1.4)$$

The variable ρ_l in Eq. (1.4) is the density of liquid water, $R_v = 461.524 [J \cdot K^{-1} kg^{-1}]$ is the gas constant for water vapor and vapor pressure e was computed via $e = P \cdot \frac{Q}{0.62197 + Q}$. Therefore, the PWV field is used together with the zenith delay

components zenith wet delay L_{wet} (ZWD) and hydrostatic delay L_{hydro} (ZHD) to assess the performance of the reconstructed atmospheric delay field from HRRR-AK.

1.4.2 Relevant Atmospheric Parameters from a Microwave Remote Sensing Perspective

The atmospheric phase screen that is observed in a SAR interferogram corresponds to the delay difference between two generally uncorrelated states of the atmosphere at two acquisition times [Hanssen, 2001]. It also corresponds to the combination of two different atmospheric signal composites that can be distinguished by their physical origin:

- 1) Turbulent mixing, resulting from turbulent convective processes in the atmosphere, creates three-dimensional heterogeneity in the refractivity field.
- 2) Vertical stratification is the result of different vertical refractivity profiles at the two SAR acquisitions. Stratification affects mountainous terrain and creates phase signatures that are correlated with topography.

As a double-differencing method, InSAR is sensitive to spatial (meters to kilometres) and temporal (days to years) variations of atmospheric delays. Hence, the atmospheric signals with temporal-spatial correlation lengths comparable to the InSAR sensitivity range can cause relevant errors in InSAR observations. In current advanced radar interferometry techniques, the predominant part of the atmospheric signal in InSAR is caused by the turbulent space-time variation of water vapor in the lower troposphere [Hanssen, 2001]. Therefore, the performance of HRRR-AK for the correction of InSAR data is defined by its ability to predict atmospheric water vapor delays, while the quality of hydrostatic delay predictions is of only secondary importance.

Circumstances are different when working with SAR geolocation techniques like tracking methods and absolute ranging. For these methods, the hydrostatic delay plays the leading role in atmospheric interferences, being approx. 10 - 100 times greater than the wet delay, depending on the weather conditions. For example, the amount of hydrostatic

delay can be as much as 2.3 m at sea level, while the wet delay only amounts to about 0.3 ~ 0.4 m in some extreme cases [*Eineder et al.*, 2011; *Hanssen*, 2001].

Hence the significance of the two terms in Eq. (1.1) depends on the radar remote sensing applications. In the following analysis of error budgets, the uncertainty of the predicted wet delay will be used to analyze its effects on SAR interferometry, while the error in the one way zenith total delay (ZTD) is derived to analyze atmospheric correction of tracking and absolute ranging techniques.

1.5 Performance Analysis of HRRR-AK Predictions

In order to assess the accuracy of using HRRR-AK in the mitigation of atmospheric delays from radar remote sensing data, experiments were performed where a large number of HRRR-AK simulations were compared to the corresponding atmosphere profiles derived from RAOBS measurements. In the analysis, the HRRR-AK products were grouped according to a set of modeling and environmental parameters to determine the influence of these parameters on HRRR-AK accuracy. These grouping parameters include (i) model lead time, (ii) season of data acquisition, and (iii) sunlight (solar radiation) conditions.

1.5.1 Applied Mathematical Model for Comparative Analysis

By evaluating the agreement between PWV products from RAOBS and HRRR-AK simulations via linear relationship assumptions, the uncertainty σ_{pwv} of PWV products was determined and propagated to determine the wet delay uncertainty $\sigma_{L,wet}$ using Eq.(1.5) and assuming a fixed value of Π^{-1} .

$$\sigma_{L,wet} = \Pi^{-1} \sigma_{pwv} \quad (1.5)$$

Similarly, the accuracy $\sigma_{L,hydro}$ of hydrostatic delay predictions was determined using linear regression analysis of HRRR-AK-simulated and RAOBS-observed hydrostatic delays computed via Eq. (1.2). Combing the error contributions from the hydrostatic and wet delay together, the error budget of the ZTD σ_L can be expressed

following Eq. (1.6).

$$\sigma_L = \left(\sigma_{L,wet}^2 + \sigma_{L,hydro}^2 \right)^{1/2} = \left[\left(\Pi^{-1} \sigma_{pwv} \right)^2 + \sigma_{L,hydro}^2 \right]^{1/2} \quad (1.6)$$

While Eq. (1.6) describes atmospheric delay errors in a single SAR acquisition, the differential delay information in an interferogram can be calculated from Eq. (1.6) via

$$\sigma_{L,ifg} = \sqrt{2} \cdot \sigma_L \quad (1.7)$$

To be able to compare RAOBS-observed and HRRR-AK simulated atmospheric data, the vertical RAOBS profiles were additionally resampled to match the vertical levels of the HRRR-AK model using linear interpolation methods.

1.5.1.1 Assessment of the Accuracy of Precipitable Water Vapor Predictions

Both RAOBS and HRRR-AK delays were integrated along the vertical to provide pairs of integrated PWV products. For comparison and statistical analysis, a linear relationship between HRRR-AK-simulated ($PWV_{HRRR-AK}$) and radiosonde-observed (PWV_{RAOBS}) PWV products was assumed and applied. Using linear regression models for such analysis has been suggested in previous studies [Li, Muller, Cross, *et al.*, 2006; Niell *et al.*, 2001], where free regression models were used to describe and analyze the relationship of radiosonde observations and multispectral remote sensing PWV measurements. In contrast to these studies, we applied a slightly modified approach that recognizes the physical properties of PWV measurements that prohibit negative values of PWV. Hence, in our analysis, the linear regression lines are forced through (0, 0) to guarantee physically meaningful results (Eq.(1.8)).

$$PWV_{HRRR-AK} = a \cdot PWV_{RAOBS} \quad (1.8)$$

The best fitting regression model was found using a least-squares fitting approach, where the radiosonde measurements were assumed error free and the best fitting regression slope \hat{a} is found from Eq. (1.9)

$$\hat{a} = \arg \min_a \left(\|PWV_{HRRR-AK} - a \cdot PWV_{RAOBS}\|^2 \right) \quad (1.9)$$

Moreover, we apply robust regression techniques where outliers among the RAOBS are identified and discarded to provide unbiased estimates of HRRR-AK performance. Most outliers were caused by instrument failures in the upper troposphere. In a pre-processing step, we also discard radiosonde records with large data gaps below 8000m.

In addition to the estimated slope \hat{a} , a set of statistical parameters that describe the quality of the fitting model are derived. The coefficient of determination R^2 is used in this study to determine the goodness of fit between HRRR-AK and RAOBS data. It is calculated according to Eq. (1.10).

$$R^2 = 1 - \frac{\sum_i (PWV_{HRRR-AK,i} - f_i)^2}{\sum_{i=1}^{i=N} (PWV_{HRRR-AK,i} - \mu(PWV_{HRRR-AK}))^2} \quad (1.10)$$

where N is the total number of data pairs, $f_i = \hat{a} \cdot PWV_{RAOBS,i}$, and $\mu(\cdot)$ is the arithmetic mean. The standard deviation $\hat{\sigma}_{\hat{a}}$ of the slope estimate is also analyzed. $\hat{\sigma}_{\hat{a}}$ expresses how well the slope is defined and additionally allows to statistically compare the slope estimates at different locations or derived from different parameter settings in NWP simulations.

A third parameter computed is the root-mean-square (RMS) of the residuals σ_{res} (see Eq. (1.11)). σ_{res} is used to express the uncertainty of the PWV products due to random noise. Here we assume that non-linear systematic errors of RAOBS measurements or HRRR-AK model can be ignored, such that σ_{res} can be considered as the error bound for the evaluated parameters, $\sigma_{pwv} \hat{=} \sigma_{res}$.

$$\sigma_{res} = \sqrt{\frac{\sum_i (PWV_{HRRR-AK,i} - f_i)^2}{N-1}} \quad (1.11)$$

The above outlined parameters only provide a full description of HRRR-AK performance if (1) the relationship between RAOBS and HRRR-AK parameters is linear and (2) if forcing our regression lines through zero does not result in non-stationary residuals. To avoid a misrepresentation of model performance, the RMS (σ_{rms}) and bias (μ_{rms}) of the *point-by-point differences* between RAOBS and HRRR-AK observations are calculated in addition to the above parameters. These additional parameters are free of linearity assumptions and allow for identifying non-stationary biases in the model predictions.

1.5.1.2 Assessment of the Accuracy of Hydrostatic Delay Predictions

After resampling to identical vertical sampling locations, the pressure information of the bottommost layer of both HRRR-AK and RAOBS is extracted and used as surface pressure to derive the hydrostatic delay from HRRR-AK ($Hydro_{HRRR-AK}$) and RAOBS ($Hydro_{RAOBS}$) via Eq. (1.2). A linear relationship, identical to the one described by Eq. (1.8), is assumed and applied for analyzing the quality of hydrostatic delay predictions ($PWW_{HRRR-AK}$ and PWW_{RAOBS} are replaced with $Hydro_{HRRR-AK}$ and $Hydro_{RAOBS}$, respectively, in Eq. (1.8)). Again, several parameters are used to describe the quality of the regression model including computing the estimated slope \hat{a} coefficient and its uncertainty $\hat{\sigma}_{\hat{a}}$, R^2 , and σ_{res} (used as the uncertainty of HRRR-AK hydrostatic delay products, assuming $\sigma_{L,hydro} = \sigma_{res}$) as well as the RMS (σ_{rms}) and the bias (μ_{rms}) of the point-by-point differences.

1.5.2 Results of Experiments

1.5.2.1 Performance of HRRR-AK as a Function of Model Lead Time

Several HRRR-AK model runs with model lead times of 6 hours, 12 hours, 18 hours and 24 hours were computed and compared to RAOBS observations. Model lead time is the period from the model start time to the time stamp for which the model output is retrieved. Weather models need enough time to "spin up" from an initial state - often derived by interpolating from coarser to finer domains - to one in which the meteorology

has fully developed within the finer, computational domain [Skamarock, 2004]. For example, it is said typical model runs start with no precipitation and need some spin-up time to introduce it in a stable way. Choosing the appropriate model lead time is critical: If the lead time is chosen too short, the model may not have reached steady state, reducing the quality of the model output. Similarly, if the model lead time is selected too long, the quality of the model output may decrease as errors accumulated in capturing the large scale structure [Wang *et al.*, 2011]. In order to determine if the optimal model lead time depends on the local climatic conditions, the data were analyzed for each of our test sites separately. With this setup, more than 600 HRRR-AK/RAOBS combinations were available for each experiment providing an excellent data base for statistical analysis.

Figure 1.2 shows the influence of model lead time on PWV estimates by plotting correlation coefficient R_{pwv}^2 (Figure 1.2a) and estimated slope coefficient \hat{a}_{pwv} together with $\hat{\sigma}_{\hat{a},pwv}$ (Figure 1.2b). In Figure 1.2a, a value close to one represents perfect linearity between HRRR-AK and RAOBS-derived total PWV. The overall R_{pwv}^2 values at all five sub-test sites are larger than 0.9 for all forecast periods, indicating a good agreement between PWV products from HRRR-AK and radiosonde observations. While the agreement to a linear relationship is good in all cases, the estimated slope values \hat{a} show some variation with model lead time and location (see Figure 1.2b). From an analysis of Figure 1.2b we can conclude that (i) the value of \hat{a}_{pwv} is always larger than 1 indicating that HRRR-AK is overestimating water vapor content relative to RAOBS measurements; (ii) for all five stations, we observed a slight, yet statistically insignificant, reduction of \hat{a}_{pwv} when increasing the forecast simulation length, which indicates the HRRR-AK is slowly getting drier. The error bars in Figure 1.2b indicate the magnitude of $\hat{\sigma}_{\hat{a}}$, which is changing very little with model lead time.

The study shows that overall ability of HRRR-AK to predict the water vapor field is not significantly degrading with increasing forecast length. The very stable R_{pwv}^2 and

\hat{a}_{pww} (Figure 1.2) parameters show that the model does not develop a bias with time.

The same linear regression procedures were also applied to assess the quality of hydrostatic delay products. The estimated R_{hydro}^2 and slope coefficients \hat{a}_{hydro} of hydrostatic delay products as well as corresponding uncertainties $\hat{\sigma}_{\hat{a},hydro}$ are shown in Figure 1.3. In Figure 1.3a, the R_{hydro}^2 values calculated from five test sites are larger than 0.93 for all model lead times and locations, indicating a well-behaved linear relationship between RAOBS-observed and HRRR-AK-simulated hydrostatic delays. In Figure 1.3b, \hat{a}_{hydro} values are shown to be statistically identical to 1 and statistically independent on model lead time (tested at the 95% confidence level).

More details on the derived HRRR-AK prediction performance are summarized in Table 1.1, showing the statistical parameters for all five stations at 6 hour and 24 hour forecast periods. In addition to the station-by-station analysis, a sixth segment is added at the bottom of the table that shows the average HRRR-AK performance across all test sites. σ_{pww} in Table 1.1 is calculated from the RMS of the residuals σ_{res} assuming a linear regression model (see Eq. (1.11)). The wet delay accuracy $\sigma_{L,wet}$ in Table 1.1 was calculated based on Eq. (1.5). $\sigma_{L,wet}$ is less than 13 mm, when using products at 6 hour forecast period, and only increases slightly when increasing model lead time to 24 hours. The statistics of the hydrostatic delay (two sub-columns in column 5 of Table 1.1) show that the uncertainty of one way hydrostatic delay predictions $\sigma_{L,hydro}$ is always less than 5.40 mm and shows only a little dependence on model lead time. Considering that the hydrostatic delay could be as large as 2.30 m at sea level, these numbers show that L_{hydro} can be estimated with a relative error of 0.3% from HRRR-AK products in high latitude regions.

As shown by column 6 in Table 1.1, the variation of total atmospheric delay uncertainty σ_L with forecast period time is small. Together with $\sigma_{L,wet}$ and $\sigma_{L,hydro}$, the

overall σ_L determined via Eq. (1.6) at 6 hours model lead time ranges from $9.00\text{mm} \leq \sigma_L \leq 13.20\text{mm}$. For a 24 hour forecast duration, σ_L is very similar with $10\text{mm} \leq \sigma_L \leq 14.30\text{mm}$. Comparing column 4 and 6 in Table 1.1, the major source of error in the HRRR-AK simulations is the model's relatively limited handling of PWV.

The wet and total delay performance of HRRR-AK shows dependence on test site with dryer climates showing better performance than more humid climates (see last column of Table 1.1 for the range of atmospheric moisture across test sites). This is a direct consequence of the model's limited performance in predicting PWV and is, as such, in line with expectations.

To supplement the information in Table 1.1, which represents the deviation of HRRR-AK from a linear regression model, Table 1.2 adds the model-free point-by-point statistics for further analysis. As σ_L is almost entirely driven by errors in PWV, only the point-by-point statistics ($\sigma_{wet,rms}$ and $\mu_{wet,rms}$) of the wet delay are shown. The results in Table 1.2 show a significant reduction of model bias from 6 hours to 24 hours model lead time, indicating that the model is getting drier when the model lead time is increased. This is consistent with the results based on regression analysis, for which a decrease in slope with increasing lead time was reported. RMS values reported in Table 1.2 are slightly larger than their regression-based counterparts in Table 1.1. This is expected as they include the full bias between observations and model while the regression-based variables only include residual biases after a best fitting regression line was removed. Hence, regression-based and regression-free error analyses are consistent.

Taken together, when applying HRRR-AK to compensate for atmospheric effects in radar signals across the Alaska region, absolute geodetic range measurements can be obtained with an accuracy of better than 14.3 mm (max. σ_L in Table 1.1, PASN 24 hours products). Assuming a spatially stationary process, we can furthermore conclude that for the studied climate conditions InSAR atmospheric delay errors can be corrected with a residual error of better than $\sigma_{L,ifg} = \sqrt{2} \cdot \sigma_L = 20.2\text{mm}$. Most of the residual atmospheric

errors are due to the model's limited ability to predict $\sigma_{L,wet}$. This finding is in good agreement with other studies where NWP predictions were compared to PWV maps from InSAR and spaceborne multispectral scanners [Liu and Hanssen, 2009]. Due to the limited dependence on model lead time, only the HRRR-AK 12 hours products paired with corresponding RAOBS will be used for evaluating and analyzing seasonal influences and effects from sunlight condition on HRRR-AK performance.

1.5.2.2 Statistics of HRRR-AK Products With Seasonal Effects

The quality of HRRR-AK products was also evaluated according to the seasonal dependence. Considering the special climate conditions of high latitude areas, where both spring and autumn are very short, we divided the annual climate into two parts, (1) the winter season with snow from November to May, and (2) the summer season from June to October based on a study of snowmelt dates in Barrow, AK [Stone *et al.*, 2002].

For performance analysis, regression models were calculated from HRRR-AK/RAOBS comparisons for all five stations and for local AK winter and summer periods separately. In addition to the station-by-station analysis, also the average seasonal dependence of HRRR-AK across *all* test sites was calculated. The detailed statistics of the local AK summer analyses are listed in Table 1.3 and local AK winter cases are shown in Table 1.4. In both tables, column 2 and 3 address PWV and wet delays, while column 4 analyzes hydrostatic delay, and the total delays as well as the corresponding PWV ranges at the study sites are shown in last two columns.

In Table 1.3, the coefficient of determination R_{pwv}^2 of PWV regressions is larger than 0.75 for all five local AK summer cases. This indicates that the linear model of Eq. (1.8) explains at least three quarter of variance in all the data pairs. σ_{pwv} in the local AK summer time varies strongly throughout our five test sites with the maximum of $\sigma_{pwv} \leq 2.76$ mm observed for PABR, corresponding to $\sigma_{L,wet} \leq 18.00$ mm. Site PANC presents the best PWV performance of all local AK summer time cases, producing

smallest σ_{pwv} , and $\sigma_{L,wet}$. Considering the relative high humidity condition in this region [Stafford *et al.*, 2000], PANC indicates the highest relative PWV accuracy of all analyzed HRRR-AK products. The regression of hydrostatic delay in Table 1.3 shows excellent fit with R_{hydro}^2 larger than 0.92 and $\sigma_{L,hydro}$ smaller than 4.27 mm. By integrating the uncertainty of wet delay and hydrostatic delay together via Eq. (1.6), the total delay uncertainty σ_L for all local summer cases is ranging between 12.47mm and 18.16mm, which is worse than the all year average performance of the model shown in Table 1.1.

Table 1.4 shows the results of the HRRR-AK/RAOBS comparison during local AK winter conditions. Due to the dryer conditions during the winter months, the HRRR-AK-simulated PWV products have smaller absolute errors with $0.57\text{mm} \leq \sigma_{pwv} \leq 1.41\text{mm}$, corresponding to $3.17\text{mm} \leq \sigma_{L,wet} \leq 9.14\text{mm}$. The simulated hydrostatic delay is again of high accuracy with $\sigma_{L,hydro} \leq 4.70\text{mm}$, leading to an estimated σ_L of less than 10.30mm.

Differences between local AK wintertime and summertime performance are pronounced in particular for the predicted wet delay component. Model overestimation (expressed by $\hat{a}_{pwv} > 1$) at sites PABR and PASN, as well as the residual signal variance σ_{pwv} at all test sites are larger during the local AK summer, where more water vapor is present in the atmosphere [Picon *et al.*, 2003].

The highest σ_{pwv} is observed in the local AK summertime for station PABR, whose water vapor field regression is shown in Figure 1.4a. It can be seen that, while significant noise exists about the regression line, the relationship between RAOBS and HRRR-AK still maintains a good linear correlation. Also, only a few outliers (points outside 95% prediction bound) are present even in this worst case scenario.

To further investigate the cause for the limited PWV estimation performance of HRRR-AK, the atmospheric parameters that contribute to the wet delay were evaluated, including vapor mixing ratio Q_v , temperature T , and pressure P (cf. Eq. (1.4)). The

vertical profiles of Q_v , T and P at PABR for local AK summer cases are plotted in Figure 1.5a-c respectively. Figure 1.5a, shows the residual of Q_v after subtraction of RAOBS measurements from HRRR-AK predictions for a large number of observation epochs (gray solid thin lines). The mean value profile of these Q_v residuals (solid black line in Figure 1.5a) indicates that HRRR-AK is underestimating RAOBS-observed Q_v near the ground and slightly overestimates Q_v in higher altitudes. The standard deviation profile of the Q_v residuals (dashed black line) shows large noise levels in the lower troposphere where stronger differences between HRRR-AK predictions and RAOBS can be observed. As the standard deviation of the residuals is larger than the mean for all height levels, no significant biases can be shown for HRRR-AK-derived Q_v data. In Figure 1.5b, vertical profiles of atmospheric temperature T are shown. The mean value profile shows a noticeable but statistically insignificant underestimation of T close to the ground and unbiased performance at higher altitudes. Pressure profiles (Figure 1.5c) demonstrate an overestimation across many height levels. Especially at near ground level, the residual mean is slightly larger than residual standard deviation suggesting a statistically significant overestimation. It is likely that the overestimation of Q_v and P led to estimated slope value of $\hat{a}_{pww} > 1$ and increases the uncertainty of PWV products of HRRR-AK (Table 1.3 column 2 and 3).

In contrast to the wet delay predictions, the hydrostatic delay data shows no dependence on season. Regression slopes as well as residual delay variance $\sigma_{L,hydro}$ are statistically identical for local AK summer and winter. $\sigma_{L,hydro}$ is the largest for local winter data pairs at station PANT (shown in Figure 1.4b). The tight grouping about the best fitting regression line (see Figure 1.4b) shows small errors of HRRR-AK in predicting hydrostatic delay.

Comparing term σ_L in Table 1.3 and Table 1.4, an evident seasonal dependence can be observed. This dependence comes from the $\sigma_{L,wet}$ in local AK summer cases being approx. 1.5 ~ 2 times larger than in local AK winter. Overall, the one way total delays in

zenith direction among the five test sites can be predicted with accuracy better than 10.5 mm in the local AK wintertime and better than 18.2 mm in local AK summer periods.

The point-by-point statistics are listed in Table 1.5. Comparing the average total delay accuracy in summer (15.70 mm; last row Table 1.3) and in winter (8.16 mm; last row Table 1.4) with statistics in the last column of Table 1.5 (17.79 mm in summer and 8.74 in winter), shows consistency between the regression-based and the regression-free statistics.

Note that regression slopes estimated for hydrostatic delay are always statistically identical to 1 (95% confidence limit) while the slopes for wet delays \hat{a}_{pwv} are all statistically larger than 1 (with exception of wintertime data for station PABR). *Li, Muller, Cross, et al.* [2006] reported similar overestimating behavior when comparing PWV products from optical remote sensing to RAOBS observations and GPS products comparing RAOBS by *Mattioli et al.* [2007]. This may indicate that the differences between HRRR-AK and RAOBS data are caused by the RAOBS observations rather than the atmospheric model. However, further experiments are needed to confirm this conclusion.

1.5.2.3 Performance of HRRR-AK Products as a Function of Time of Day

Kuo and Sun [1976] concluded that the atmosphere is usually stable at all vertical levels during the night, while during daytime, shortwave solar radiation is leading to unstable atmospheric conditions. This diurnal variation may cause a variation of HRRR-AK performance with time of day.

Additionally, most microwave remote sensing systems operate in sun synchronous orbits with mean local times in descending mode of either around 10:00 am (10:00 pm for ascending), e.g. Environmental Satellite (ENVISAT), or around $\sim 6:00$ am (6:00 pm for ascending), e.g. for TerraSAR-X and Cosmo-SkyMed. Hence, a study of daylight effects on the performance of HRRR-AK is useful to pre-determine achievable atmospheric correction accuracies for microwave remote sensing systems with different

acquisition modes.

For this study, the data stack has been grouped into two categories: (i) night time data pairs (12UTC, 03AKST) and (ii) day time data pairs (00UTC, 15AKST). Due to the effects of the midnight sun on regions above the Arctic Circle (latitude higher than 66.56 degree in north hemisphere), both test site PABR with latitude 71.3 degree and PAFA at latitude 65° North are suffering difficulty to classify data pairs acquired at different daylight condition. Hence, to keep the simplicity of grouping the RAOBS and HRRR-AK data pairs from different sunlight conditions, only the lower latitude stations, including PANC, PASN and PANT, were selected for this study, for which variations of sunrise and sunset times are less. A 12 hours model lead time was used and the statistics of PWV and radar signal delay products were computed and listed in Table 1.6 (nighttime cases) and Table 1.7 (daytime cases).

Both nighttime and daytime data show good linear correlation behavior with R_{pwv}^2 and R_{hydro}^2 values larger than 0.9. There is no statistically significant effect of sunlight on the uncertainty of one way total delay σ_L measurements (95% confidence level). While there are no effects on the total delay regression parameters, significant effects on the estimated PWV regression slopes \hat{a}_{pwv} and minor effects on the estimation uncertainty of wet delays $\sigma_{L,wet}$ can be observed. Slopes \hat{a}_{pwv} are larger and $\sigma_{L,wet}$ increases during daytime. In contrast to the wet delay components, the computed $\sigma_{L,hydro}$ is slightly smaller for the day time cases.

The point-by-point statistics of daylight effects are listed in Table 1.8. It shows that, on average, biases of the ZWD are about 4mm higher during day time than at night while ZHD biases are similar for day and night time conditions. This leads to ZTD day time biases that exceed nighttime biases by about 3 mm. RMS values show very similar behavior, with daytime RMS values exceeding nighttime values by 4 mm and 3 mm for ZWD and ZTD, respectively. The results from regression-based and point-by-point

analyses are again consistent, indicating that the regression approach did not introduce errors in our performance parameters.

1.6 Discussion

1.6.1 Comparison with other NWP products in delay related components prediction

To investigate the performance of HRRR-AK relative to other NWP systems, we conducted a literature research of studies that assessed the performance of NWPs for signal delay correction. Four major global meteorological data were used in the identified studies (listed in column one in Table 1.9), including (1) reanalysis products from the European Centre for Medium-Range Weather Forecasts (ECMWF) (e.g., ERA-Interim reanalysis products from ECMWF) [Cong *et al.*, 2012], (2) the National Centers for Environmental Prediction-National Center for Atmospheric Research (NCEP-NCAR) Reanalysis I (NCEP-I), (3) the NCEP-Department of Energy (DOE) reanalysis II (NCEP-II), and (4) initial boundary conditions generated from the Meteorological Assimilation Data Ingest Systems (MADIS) via the assimilation system, e.g. Local Analysis and Prediction System (LAPS) [Foster *et al.*, 2013].

In some of the studies, the meteorological data were fed into various NWP models as initial boundary conditions to produce ‘customized’ simulations, e.g. studies conducted by Pacione *et al.* [2001], Behrend *et al.* [2002], and Foster *et al.* [2013] as well as HRRR-AK (Table 1.9). The other identified case studies, however, focused on the performance assessment of global meteorological data without customized refinements, e.g. the studies from Bock and Nuret [2009] and Cong *et al.* [2012]. The main NWP model that was used in these studies is the National Center for Atmospheric Research-PennState Mesoscale Model Version 5 (MM5).

A comparison of HRRR-AK with other systems is complicated by the fact that previous studies used very inconsistent analysis parameters. As summarized in Table 1.9 column one, a wide range of parameters was used to analyze NWP performance including PWV, ZWD and ZTD values. Also, for performance analysis, the studied

NWPs were compared to a range of reference data including GPS products and Very Long Baseline Interferometry (VLBI) (see column three of Table 1.9 for information on applied reference data). Moreover, two types of statistics are listed in column five of Table 1.9 including the standard deviation of difference between model and reference data marked by superscript ‘c’, while the rest were computed using the root-mean-square of differences. Additionally, the data time span of every study is listed in column six of Table 1.9 to help in understanding the representativeness of statistics from different studies.

To facilitate a comparison of our results to these published data, the findings from our study are listed in Table 1.9 (see last three rows). We are listing the winter-summer statistics using 12 hours model lead times as well as the average HRRR_AK model performance of the 24 hours model lead time results (see numbers in brackets in the last three rows of Table 1.9). All HRRR-AK results in Table 1.9 have already been listed in previous tables. The bias of HRRR-AK PWV estimation is about the same level as NCEP-I and significantly better than that of most other reported models. The overall bias of HRRR-AK in ZWD and ZTD products is similar to other models initialized by ECMWF inputs. The average RMS of HRRR-AK simulation was found to be superior to the RMS of most of the other models shown in Table 1.9. Hence, the performance parameters found for HRRR-AK appear realistic in nature and indicate a slightly improved quality of HRRR-AK compared to similar models.

1.6.2 Summary of findings

In order to provide a thorough statistical analysis of the performance of the NWP HRRR-AK for atmospheric correction of microwave remote sensing data, this study performed a comparative analysis of atmospheric data from RAOBS measurements with predictions from the HRRR-AK model. Within this research, five test sites were selected over Alaska, to cover a wide range of climate types of subarctic and Arctic regions in the US. The performance of HRRR-AK in atmospheric artifacts correction for radar signals was assessed by comparing atmospheric parameters from HRRR-AK simulations and radiosonde observations, including vertical precipitable water vapor (PWV) and absolute

signal delays (see Section 1.4.2 and Section 1.5.1). The HRRR-AK accuracy analysis was based on linear regression models, point-by-point comparisons and utilized error propagation techniques. To assess how the model set-up parameters and physical conditions affect the HRRR-AK performance, a series of experiments were designed, analyzing the dependence of prediction performance on model lead times, seasonal effects, as well as sunlight conditions. Our analysis shows that HRRR-AK overestimates the amount of PWV compared to ROABS observations, indicated by significant deviations of best-fitting linear regression slopes from 1 (Eq.(1.8)). Uncertainties due to bias ($\mu_{wet,rms}$) and random errors of wet delay shows a significant reduction of model bias from 6 hours to 24 hours (Table 1.2), indicating the model getting drier when increasing model forecast period. Hence, a pre-calibration of HRRR-AK products is suggested that is able to reduce this bias. Uncertainties due to random errors (Table 1.1) showed only little dependency on model lead time. Both the accuracy of simulated PWV delays $\sigma_{L,wet}$ as well as absolute signal delays σ_L showed no significant change with changing model lead times.

At a model lead time of 24 hours, the uncertainties σ_{pwv} from random errors computed from HRRR-AK can be predicted with accuracies varying between 1.62mm and 2.08mm at different test sites. At 6 hours lead time, σ_{pwv} is slightly smaller and ranges from 1.31 mm to 2.0 mm (see Table 1.1). This is within the accuracy level of radiosonde observation itself (1~2 mm) [Niell *et al.*, 2001]. The observed σ_{pwv} corresponds to wet delay uncertainties of $\sigma_{L,wet} \leq 13.51mm$ for all tested model lead times. The uncertainty of the hydrostatic delay $\sigma_{L,hydro}$ was determined to be less than 5.4mm independent of climate region. Although hydrostatic delays dominate the total delay along the radar propagation path, its impact on the uncertainty of the one-way ZWD is relatively small compared to the wet delay influence $\sigma_{L,wet}$. In summary, for different tested sets and model lead times setting σ_L from random errors can be simulated with an accuracy of better than 14.3 mm (Table 1.1) with 90% of the errors

contributed by water vapor.

An analysis of seasonal influences on HRRR-AK performance used only data with model lead times of 12 hours and found that the overall accuracy of one way total delay predictions in all climate conditions during the local AK winter time (< 10.3 mm) is better than the one in local summer (< 18.2 mm) as shown in Table 1.3 and Table 1.4. The regression slope analysis showed that for all regions (with the exception of wintertime data at site PABR) regression slopes were statistically significantly larger than 1, together with the bias listed in Table 1.5 indicating a PWV overestimation of HRRR-AK relative to RAOBS data. Similar estimation biases were reported in previous studies [Li, Muller, Cross, *et al.*, 2006; Mattioli *et al.*, 2007]. The causes for the observed PWV overestimation were further analyzed by examining the vertical profiles of the predicted atmospheric parameters Q_v , P , and T (see Figure 1.5). These analyses suggest that biases in water vapor mixing ratios Q_v and pressure P are the main reasons for model errors.

An assessment of the dependencies of HRRR-AK performance on sunlight conditions was conducted using stations PANC, PASN, and PANT, which were selected due to their geographic locations. From this study, both daytime and nighttime data showed good linear correlation with RAOBS observations for both PWV and hydrostatic delay predictions (Table 1.6 and Table 1.7). The estimated average total delay error σ_L from random errors in the nighttime stack was ~ 1 mm smaller than the daytime data.

Regarding the dependence of HRRR-AK on climate conditions, test site PANT, which is the southernmost test site with highest average water vapor records, shows slightly worse linear correlation to RAOBS measurements. This is further evidence that humidity has significant influence on HRRR-AK performance. However further studies are necessary to study this relationship.

1.6.3 Error sources in methodology of assessment

Besides the limitations inherent in the HRRR-AK product itself, there are methodology-related issues that may lead to an overestimation of the total HRRR-AK error budget in this study:

- 1) *Timing error in data comparison.* The output of the HRRR-AK model can be considered as an instantaneous product that provides simulations of the atmosphere at user defined time steps. However, the radiosonde is recording atmospheric data over time while the balloon is rising from the ground to 15 km ASL. This ascent can take up to 1 hour [Niell et al., 2001]. This short timing inconsistency may introduce errors mostly into measurements of the highly turbulent atmospheric water vapor.
- 2) *Drifting of the radiosonde balloon.* The previous records show that radiosonde can drift as far as 200 km from the point of balloon release [NWS, 2010] as winds may lead to a tilted flight path rather than a rise in zenith direction. As the resolution grid of the HRRR-AK model is 3 km in lateral direction, this may lead to a drift through several model pixels. Since the atmosphere can be considered spatially smooth and the wind speed is much lower near the ground, the introduced errors may not be significant.
- 3) *Inaccurate topography records between radiosonde and numerical weather simulations.* Disagreements between the height of the bottom most layer in the HRRR-AK model and the recorded topography height in RAOBS data will introduce residuals in surface pressure estimates that increase the uncertainty of simulated zenith hydrostatic delays. As no significant biases of hydrostatic delays were found, we assume that this error was insignificant for our test sites.
- 4) *Errors introduced by the projection parameter Π .* Π is a projection parameter whose value weakly and inversely depends on the atmospheric surface temperature (see Eq. (1.3)). Despite this dependency, a fixed value of $\Pi = 6.5$ was used in this study, corresponding to a surface temperature of 5°C [Bevis et al., 1992]. Specifically for Alaskan regions with highly variable and deviating climatic conditions, using a constant value for Π could lead to biases. For instance, Π is about 7.2 during the winter period of PABR, which could lead to an underestimation of PWV for this area. Given the low humidity conditions during Alaska winters, biases of ZWD in the winter season related to errors in Π are still relatively small, e.g. less than 0.5mm for PABR during winter days with surface temperature of -30°C .

1.7 Conclusions and Suggestions

Overall, the HRRR-AK products with less than 24 hours model lead time can be used for calibrating atmospheric delays in spaceborne SAR systems with an average residual error of less than ~13 mm (Table 1.1 last row) to 14 mm (Table 1.2 last column). These results are valid for sub-arctic and arctic conditions. The main performance limitation stems from inaccurate PWV delay predictions while the error contribution of hydrostatic delay components is small. Consequently, absolute ranging and correlation-based deformation measurements can be corrected with an average residual error of less than ~13 to 14 mm. Differential ZTD in InSAR data can be corrected with residual errors of about 20 mm (Eq.(1.7)). Atmospheric correction using HRRR-AK data promises better performance during winter months (e.g., from November to May) compared to the period from June to October (summer). For Alaska-type climates, the performance difference between winter and summer is about a factor of 2 (see Tables 1.3 and 1.4). The weak correlation between non-systematic errors in ZTD and sunlight conditions suggests that the HRRR-AK product would provide statistically equal performance for atmospheric delay correction in ascending imagery and descending imagery.

1.8 Acknowledgements

This work was support by the NASA Headquarters under the NASA Earth and Space Science Fellowship Program - Grant NNX10AO70H. HRRR-AK data was provided by the Arctic Region Supercomputing Center at the University of Alaska Fairbanks. We thank Julie Malingowski, NOAA National Weather Service for providing valuable radiosonde stations information.

1.9 References

- ARSC (2012), ARSC High Resolution Rapid Refresh (HRRR), Arctic Region Supercomputing Center <http://weather.arsc.edu/HRRR/>.
- Behrend, D., R. Haas, D. Pino, L. P. Gradinarsky, S. J. Keihm, W. Schwarz, L. Cucurull, and A. Rius (2002), MM5 derived ZWDs compared to observational results from

- VLBI, GPS and WVR, *Physics and Chemistry of the Earth, Parts A/B/C*, 27(4-5), 301-308.
- Benson, C., S. A. Bowling, and G. Weller (1983), Urban climates in Alaska, *Enviroments*, 15(2), 23-26.
- Berardino, P., G. Fornaro, R. Lanari, and E. Sansosti (2002), A new algorithm for surface deformation monitoring based on small baseline differential SAR interferograms, *IEEE Transaction of Geosciences and Remote Sensing*, 40(11), 2375-2383.
- Bevis, M., S. Businger, T. A. Herring, C. Rocken, R. A. Anthes, and R. H. Ware (1992), GPS meteorology: Remote sensing of atmospheric water vapor using the global Positioning System, *Journal of Geophysical Research*, 97(D14), 15787-15801.
- Bieniek, P. A., U. S. Bhatt, R. L. Thoman, H. Angeloff, J. Partain, J. Papineau, F. Fritsch, E. Holloway, J. E. Walsh, C. Daly, M. Shulski, G. Hufford, D. F. Hill, S. Calos and R. Gens (2012), Climate divisions for alaska based on objective methods, *Journal of Applied Meteorology and Climatology*, 51(7), 1276-1289.
- Bock, O., and M. Nuret (2009), Verification of NWP Model analyses and Radiosonde humidity data with GPS precipitable water vapor estimates during AMMA, *Weather and Forecasting*, 24(4), 1085-1101.
- Chen, M. H., R. B. Rood, and W. G. Read (1999), Seasonal variations of upper tropospheric water vapor and high clouds observed from satellites, *Journal of Geophysics Research: Atmosphere*, 104(D6), 6193-6197.
- Cong, X., U. Balss, M. Eineder, and T. Fritz (2012), Imaging geodesy: Centimeter-level ranging accuracy with TerraSAR-X: An Update, *IEEE Geoscience and Remote Sensing Letters*, 9(5), 948-952.
- Davis, J. L., T. A. Herring, I. I. Shapiro, A. E. E. Rogers, and G. Elgered (1985), Geodesy by Radio Interferometry - Effects of atmospheric Modeling Errors on Estimates of Baseline Length, *Radio Science*, 20(6), 1593-1607.
- Dzurisin, D. (2007), *Volcano deformation : geodetic monitoring techniques*, 441 p. pp., Springer-Praxis Berlin; New York; Chichester, UK.

- Eineder, M., C. Minet, P. Steigenberger, X. Cong, and T. Fritz (2011), Imaging geodesy: Toward centimeter-level ranging accuracy with TerraSAR-X, *IEEE Transaction of Geosciences and Remote Sensing*, 49(2), 661-671.
- England, M. N., F. J. Schmidlin, and J. M. Johansson (1993), Atmospheric moisture measurements - a microwave radiometer - Radiosonde comparison, *IEEE Transaction of Geosciences and Remote Sensing*, 31(2), 389-398.
- Ferretti, A., C. Prati, and F. Rocca (2001), Permanent scatterers in SAR interferometry, *IEEE Transaction of Geosciences and Remote Sensing*, 39(1), 8-20.
- Foster, J., J. Kealy, T. Cherubini, S. Businger, Z. Lu, and M. Murphy (2013), The utility of atmospheric analyses for the mitigation of artifacts in InSAR, *Journal of Geophysical Research: Solid Earth*, 118(2), 748-758.
- Fournier, T., M. E. Pritchard, and N. Finnegan (2011), Accounting for atmospheric delays in InSAR data in a search for long-wavelength deformation in South America, *IEEE Transaction of Geosciences and Remote Sensing*, 49(10), 3856-3867.
- Gong, W., F. Meyer, P. Webley, and Z. Lu (2010), Tropospheric correction of InSAR time-series with the weather research forecasting model: an application to volcanic deformation monitoring, in *American Geophysical Union, Fall Meeting 2010*, edited, pp. abstract #G52A-08, San Francisco.
- UK Meteorological Office (1991), *Meteorological glossary*, 6th ed., 335 p. pp., HMSO, London.
- Hanssen, R. (2001), *Radar Interferometry: Data Interpretation and Error Analysis*, 1 ed., Kluwer Academic Publishers.
- Kampes, B. M. (2005), Displacement parameter estimation using Permanent Scatterer Interferometry, PhD Thesis, Delft University of Technology.
- Kuo, H. L., and W. Y. Sun (1976), Convection in the Lower Atmosphere and its Effects, *Journal of the Atmospheric Sciences*, 33(1), 21-40.
- Li, Z., E. J. Fielding, P. Cross, and J. Muller (2006), Interferometric synthetic aperture radar atmospheric correction: GPS topography-dependent turbulence model, *Journal of Geophysical Research: Solid Earth*, 111(B2), B02404.

- Li, Z., E. J. Fielding, P. Cross, and R. Preusker (2009), Advanced InSAR atmospheric correction: MERIS/MODIS combination and stacked water vapour models, *International Journal of Remote Sensing*, 30(13), 3343-3363.
- Li, Z., J. P. Muller, P. Cross, P. Albert, J. Fischer, and R. Bennartz (2006), Assessment of the potential of MERIS near-infrared water vapour products to correct ASAR interferometric measurements, *International Journal of Remote Sensing*, 27(2), 349-365.
- Liu, L., T. Zhang, and J. Wahr (2010), InSAR measurements of surface deformation over permafrost on the North Slope of Alaska, *Journal of Geophysical Research: Earth Surface*, 115(F3), F03023.
- Liu, S., and R. Hanssen (2009), The Atmospheric phase screen: Characteristics and estimation, in *The Troposphere, Ionosphere, GPS, and Interferometric Radar Workshop*, Pasadena, CA, USA.
- Lu, Z., D. Dzurisin, J. Biggs, C. Wicks, and S. McNutt (2010), Ground surface deformation patterns, magma supply, and magma storage at Okmok volcano, Alaska, from InSAR analysis: 1. Intereruption deformation, 1997–2008, *Journal of Geophysical Research: Solid Earth*, 115(B5), B00B02.
- Mattioli, V., E. R. Westwater, D. Cimini, J. C. Liljegren, B. M. Lesht, S. I. Gutman, and F. J. Schmidlin (2007), Analysis of Radiosonde and ground-based remotely sensed PWV data from the 2004 North Slope of Alaska Arctic winter radiometric experiment, *Journal of Atmospheric and Oceanic Technology*, 24(3), 415-431.
- Meyer, F., R. Bamler, R. Leinweber, and J. Fischer (2008), A comparative analysis of tropospheric water vapor measurements from MERIS and SAR, paper presented at IEEE International Geoscience and Remote Sensing Symposium, Boston, USA.
- Morton, D., and J. Malingowski (2012), Personal communications in radiosonde equipments in Alaska, edited.
- Niell, A. E., A. J. Coster, F. S. Solheim, V. B. Mendes, P. C. Toor, R. B. Langley, and C. A. Upham (2001), Comparison of measurements of atmospheric wet delay by

- Radiosonde, water vapor radiometer, GPS, and VLBI, *Journal of Atmospheric and Oceanic Technology*, 18(6), 830-850.
- NOAA (2012), Rapid Refresh (RR), Earth system research laboratory, <http://rapidrefresh.noaa.gov/>.
- NWS (2010), Operations and services upper air program NWSPD 10-14 Rawinsonde observations, Department of Commerce, NOAA, <http://www.nws.noaa.gov/directives/>
- Onn, F., and H. A. Zebker (2006), Correction for interferometric synthetic aperture radar atmospheric phase artifacts using time series of zenith wet delay observations from a GPS network, *Journal of Geophysical Research: Solid Earth*, 111(B9), B09102.
- Pacione, R., C. Sciarretta, F. Vespe, C. Faccani, R. Ferretti, E. Fionda, C. Ferraro, and A. Nardi (2001), GPS meteorology: validation and comparisons with ground-based microwave radiometer and mesoscale model for the Italian GPS permanent stations, *Physics and Chemistry of the Earth, Part A: Solid Earth and Geodesy*, 26(3), 139-145.
- Peel, M. C., B. L. Finlayson, and T. A. McMahon (2007), Updated world map of the Koppen-Geiger climate classification, *Hydrol Earth Syst Sc*, 11(5), 1633-1644.
- Picon, L., R. Roca, S. Serrar, J. L. Monge, and M. Desbois (2003), A new METEOSAT “water vapor” archive for climate studies, *Journal of Geophysical Research: Atmospheres*, 108(D10), 4301.
- Resch, G. M. (1980), *Water vapor- The wet blanket of Microwave Interferometry* 265-282 pp., Academic Press, New York.
- Richter, J. H., and H. V. Hitney (1980), *The effects of atmospheric refractivity on microwave propagation*, Academic Press, New York.
- Searby, H. W. (1968), *Climates of the States: Alaska*, 22 pp, U.S. Department of Commerce.
- Segall, P. (2010), *Earthquake and volcano deformation*, xxiii, 432 p., [438] p. of plates pp., Princeton University Press, Princeton, N.J.
- Skamarock, W. C. (2004), Evaluating mesoscale NWP models using kinetic energy spectra, *Mon Weather Rev*, 132(12), 3019-3032.

- Skamarock, W. C., J. B. Klemp, J. Dudhia, D. O. Gill, M. Barker, K. G. Duda, X. Y. Huang, W. Wang, and J. G. Powers (2008), A description of the Advanced Research (WRF) Version 3, pp82-83 pp, National Center for Atmospheric Research.
- Sleep, N. H., and K. Fujita (1997), *Principles of geophysics*, xviii, 586 pp, Blackwell Science, Malden, Mass., USA.
- Smith, E. K., and S. Weintraub (1953), The constants in the equation for atmospheric refractive Index at radio frequencies, *Proceedings of the IRE*, 41(8), 1035-1037.
- Stafford, J. M., G. Wendler, and J. Curtis (2000), Temperature and precipitation of Alaska: 50 year trend analysis, *Theor Appl Climatol*, 67(1-2), 33-44.
- Stone, R. S., E. G. Dutton, J. M. Harris, and D. Longenecker (2002), Earlier spring snowmelt in northern Alaska as an indicator of climate change, *Journal of Geophysical Research: Atmosphere*, 107(D10).
- UW (2012), Atmospheric Sounding, University of Wyoming, College of Engineering, Dept. of Atmospheric Science, <http://weather.uwyo.edu/upperair/sounding.html>.
- Wang, C., D. Wilson, T. Haack, P. Clark, H. Lean, and R. Marshall (2011), Effects of initial and boundary conditions of mesoscale models on simulated atmospheric refractivity, *Journal of Applied Meteorology and Climatology*, 51(1), 115-132.
- Wang, J., and L. Zhang (2008), Systematic errors in global Radiosonde precipitable water data from comparisons with ground-based GPS measurements, *Journal of Climate*, 21(10), 2218-2238.
- Webley, P. W., R. M. Bingley, A. H. Dodson, G. Wadge, S. J. Waugh, and I. N. James (2002), Atmospheric water vapour correction to InSAR surface motion measurements on mountains: results from a dense GPS network on Mount Etna, *Physics and Chemistry of the Earth*, 27(4-5), 363-370.
- Wei, M., D. Sandwell, and B. Smith-Konter (2010), Optimal combination of InSAR and GPS for measuring interseismic crustal deformation, *Advances in Space Research*, 46(2), 236-249.

Xu, W. B., Z. W. Li, X. L. Ding, and J. J. Zhu (2011), Interpolating atmospheric water vapor delay by incorporating terrain elevation information, *Journal of Geodesy*, 85(9), 555-564.

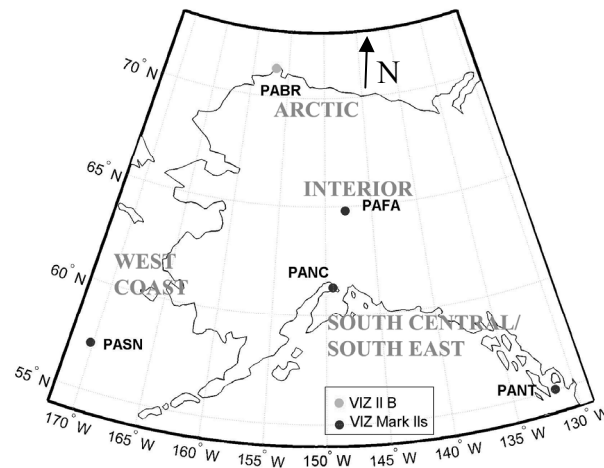


Figure 1.1 Locations of the radiosonde stations across Alaska that are used in this research. The four-letter codes printed in bold are the ICAO indicators of the observations stations. The gray dot indicates the station using a VIZ II B radiosonde during the study period while black dots represent stations that were using VIZ Mark IIs GPS microsondes. The classified climate regions in Alaska are listed in gray capital letters.

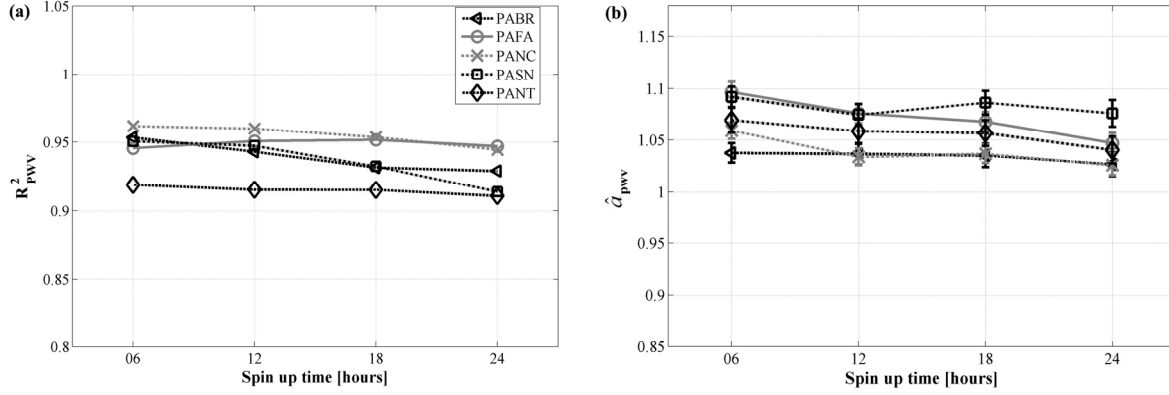


Figure 1.2 Statistical analysis results of the effect of different HRRR-AK model lead times on the predictability of PWV at each of the test sites. To calculate these statistics, HRRR-AK-derived PWV were compared to radiosonde observations at every station: (a) variation of correlation coefficient R^2_{PWV} ; (b) variation of \hat{a}_{PWV} and corresponding $\hat{\sigma}_{\hat{a}_{PWV}}$ shown as error bars. Black dashed line with left triangle for PABR; gray bold line with circle for PAFA; gray dashed line with cross for PANC; black dashed line with square for PASN; black dashed line with black diamond for PANT.

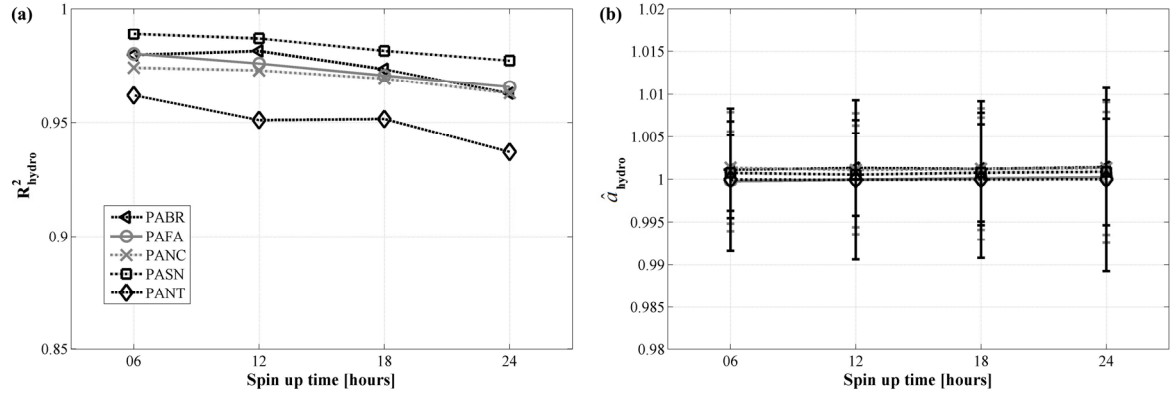


Figure 1.3 Statistical analysis results of the effect of different HRRR-AK model lead times on the accuracy of hydrostatic delay predictions at the five test sites: (a) variation of correlation coefficient R^2_{hydro} ; (b) variation of \hat{a}_{hydro} and corresponding $\hat{\sigma}_{\hat{a}_{hydro}}$ shown as error bars. Black dashed line with left triangle for PABR; gray bold line with circle for PAFA; gray dashed line with cross for PANC; black dashed line with square for PASN; black dashed line with black diamond for PANT.

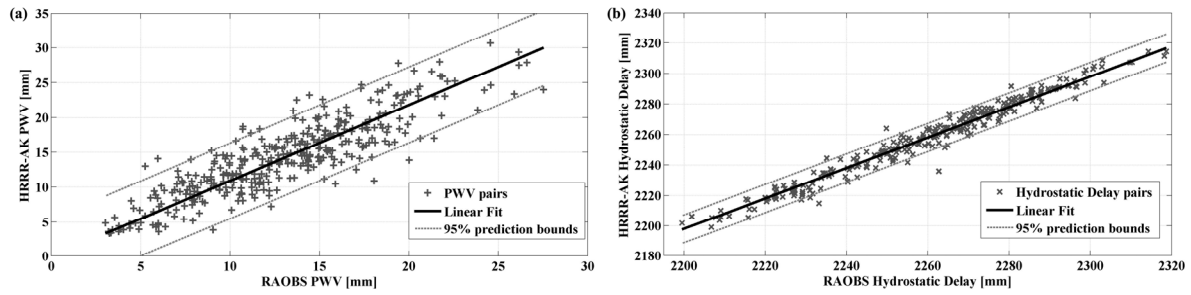


Figure 1.4 Examples of linear regression of HRRR-AK vs. RAOBS data for PWV and hydrostatic delay. (a) Linear regression of PWV data pairs at station PABR over summer period; (b) Linear regression of hydrostatic delay data pairs at station PANT over winter period.

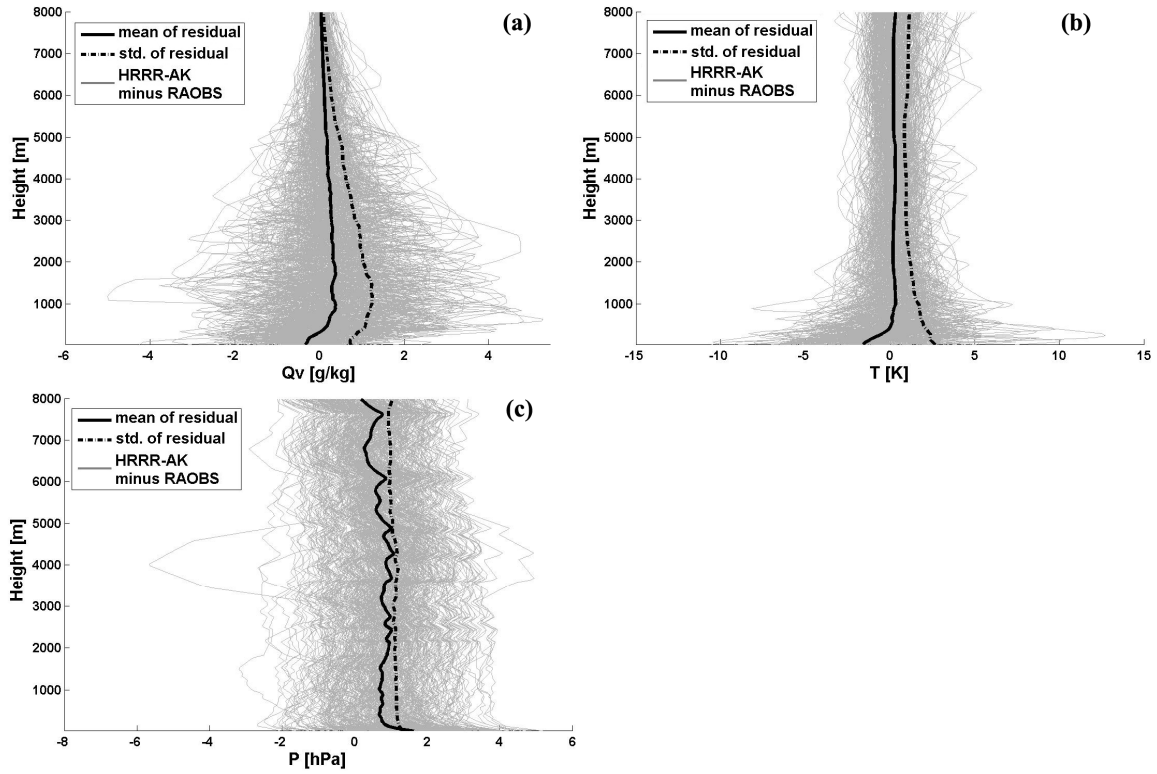


Figure 1.5 Examples of vertical profiles of atmospheric parameters extracted from PABR summertime data pairs. (a) Vertical profile of Q_v ; (b) Vertical profile of T ; (c) Vertical profile of P . Gray thin lines show the residuals of HRRR-AK simulated atmospheric parameters minus RAOBS corresponding records. Black solid lines are computed from the mean of residuals at corresponding height and black dashed lines are the standard deviation of residuals.

Table 1.1 Statistical analysis of one way zenith delay for several test sites in Alaska at 6 hour and 24 hour model lead time settings. Statistics are relative to a linear best fitting regression model.

Site name	Lead time [hour]	PWV ^a		Wet delay	Hydrostatic delay		Total delay	PWV range [mm] Min ~ Max (mean) ^c
		\hat{a}_{pwv}	σ_{pwv} [mm]		\hat{a}_{hydro}	$\sigma_{L,hydro}$ [mm]		
PABR	6	1.04	1.31	8.48	1.00	3.14	9.04	1.06~27.53 (8.58)
	24	1.03	1.62	10.55	1.00	4.43	11.44	
PAFA	6	1.10	1.90	12.38	1.00	3.65	12.90	1.09~30.88 (12.12)
	24	1.05	1.80	11.71	1.00	4.72	12.63	
PANC	6	1.06	1.47	9.56	1.00	4.09	10.40	0.81~33.74 (12.83)
	24	1.03	1.72	11.19	1.00	4.88	12.20	
PASN	6	1.09	1.62	10.53	1.00	3.19	11.00	1.72~34.73 (11.93)
	24	1.08	2.08	13.51	1.00	4.63	14.29	
PANT	6	1.07	1.91	12.41	1.00	4.23	13.11	1.50~37.03 (14.57)
	24	1.04	1.99	12.95	1.00	5.36	14.02	
All	6	/	1.66	10.77	/	3.69	11.39	/
	24	/	1.85	12.00	/	4.81	12.93	

^a The first row of the table denotes the main columns. For example, column 3 is presenting PWV statistics while \hat{a}_{pwv} and σ_{pwv} will be referred as sub-column of column 3 (the same as following tables).

^b $\sigma_{L,wet}$, uncertainty of one way zenith wet delay was calculated via Eq. (1.5)

^c PWV conditions computed from radiosonde observations (the same as following tables)

Table 1.2 RMS(bias) of difference (HRRR-AK minus RAOBS) at 6 hour and 24 hour model lead time settings. The rows show RMS(bias) values of PWV for every analysed test site, overall PWV RMS(bias) for all test sites, overall RMS(bias) of delay components (unit, mm) (the same as Table 1.5 and Table 1.8): Zenith Wet Delay (ZWD), Zenith Hydrostatic Delay (ZHD) and Zenith Total Delay (ZTD)

	PABR	PAFA	PANC	PASN	PANT	All	All ZWD	All ZHD	All ZTD
6	1.36	2.35	1.71	2.05	2.21	1.97	12.79	4.19	13.46
hour	(0.31)	(1.34)	(0.87)	(1.19)	(1.18)	(0.98)	(6.37)	(1.34)	(7.71)
24	1.65	1.92	1.76	2.32	2.09	1.96	12.72	5.29	13.78
hour	(0.25)	(0.74)	(0.46)	(1.03)	(0.69)	(0.63)	(4.10)	(1.78)	(5.88)

Table 1.3 Statistical analysis of one way zenith delay of summer cases at 12 hour model lead time setting.

Site name	PWV			Wet delay	Hydrostatic delay			Total delay	PWV range [mm]
	\hat{a}_{pwv}	R^2_{pwv}	σ_{pwv} [mm]	$\sigma_{L,wet}$ [mm]	\hat{a}_{hydro}	R^2_{hydro}	$\sigma_{L,hydro}$ [mm]	σ_L [mm]	Min ~ Max (mean)
PABR	1.09	0.75	2.76	17.91	1.00	0.97	2.99	18.16	3.04 ~ 27.53 (12.94)
PAFA	1.08	0.78	2.36	15.32	1.00	0.96	3.43	15.70	3.77 ~ 30.88 (17.62)
PANC	1.04	0.85	1.84	11.96	1.00	0.97	3.54	12.47	4.94 ~ 33.10 (18.28)
PASN	1.08	0.85	2.29	14.89	1.00	0.98	3.29	15.25	6.00 ~ 34.73 (16.65)
PANT	1.06	0.78	2.45	15.91	1.00	0.92	4.27	16.47	6.61 ~ 37.55 (18.67)
All	\	\	2.35	15.30	\	\	3.35	15.70	\

Table 1.4 Statistical analysis of one way zenith delay of winter cases at 12 hour model lead time setting.

Site name	PWV			Wet delay	Hydrostatic delay			Total delay	PWV range [mm] Min ~ Max (mean)
	\hat{a}_{pwv}	R^2_{pwv}	σ_{pwv} [mm]	$\sigma_{L,wet}$ [mm]	\hat{a}_{hydro}	R^2_{hydro}	$\sigma_{L,hydro}$ [mm]	σ_L [mm]	
PABR	0.98	0.95	0.57	3.71	1.00	0.99	2.90	4.71	1.06 ~ 15.11 (4.21)
PAFA	1.08	0.92	0.94	6.13	1.00	0.99	4.01	7.33	1.10 ~ 18.20 (4.94)
PANC	1.04	0.91	1.05	6.84	1.00	0.98	4.50	8.19	0.81 ~ 22.59 (6.31)
PASN	1.05	0.86	1.31	8.54	1.00	0.99	3.77	9.33	1.69 ~ 23.86 (6.63)
PANT	1.06	0.90	1.41	9.14	1.00	0.97	4.70	10.27	1.50 ~ 21.20 (9.44)
All	\	\	1.09	7.10	\	\	4.02	8.16	\

Table 1.5 RMS (bias) of difference for winter and summertime acquisitions (HRRR-AK 12 hours products minus RAOBS).

	PABR	PAFA	PANC	PASN	PANT	All	All ZWD	All ZHD	All ZTD
Local	0.58	1.04	1.10	1.37	1.53	1.16	7.57	4.38	8.74
Winter	(-0.09)	(0.40)	(0.33)	(0.44)	(0.60)	(0.33)	(2.16)	(0.16)	(2.33)
Local	3.01	2.78	1.97	2.69	2.70	2.65	17.25	4.34	17.79
Summer	(1.35)	(1.66)	(0.85)	(1.47)	(1.30)	(1.33)	(8.61)	(2.30)	(10.92)

Table 1.6 Performance analyses of daylight effects to simulation, 12UTC (03AKST) night-time.

Site name	PWV			Wet delay $\sigma_{L,wet}$ [mm]	Hydrostatic delay			Total delay σ_L [mm]	PWV range [mm] Min ~ Max (mean)
	\hat{a}_{pwv}	R^2_{pwv}	σ_{pwv} [mm]		\hat{a}_{hydro}	R^2_{hydro}	$\sigma_{L,hydro}$ [mm]		
PANC	1.01	0.97	1.39	9.04	1.00	0.97	4.23	9.98	0.81~32.50 (13.29)
PASN	1.05	0.96	1.57	10.18	1.00	0.99	3.81	10.87	1.85~33.24 (12.45)
PANT	1.02	0.93	1.82	11.80	1.00	0.94	5.13	12.87	1.88~37.55 (15.08)
All	\	\	1.59	10.36	\	\	4.42	11.26	\

Table 1.7 Performance analyses of daylight effects to simulation, 00UTC (15AKST) day-time.

Site name	PWV			Wet delay	Hydrostatic delay			Total delay	PWV range [mm]
	\hat{a}_{pwv}	R^2_{pwv}	σ_{pwv} [mm]	$\sigma_{L,wet}$ [mm]	\hat{a}_{hydro}	R^2_{hydro}	$\sigma_{L,hydro}$ [mm]	σ_L [mm]	Min ~ Max (mean)
PANC	1.06	0.96	1.50	9.74	1.00	0.98	4.03	10.54	1.05~33.10 (12.35)
PASN	1.11	0.94	1.75	11.40	1.00	0.99	3.33	11.87	1.69~34.73 (11.35)
PANT	1.10	0.91	2.05	13.35	1.00	0.96	4.40	14.06	1.50~37.05 (14.15)
All	\	\	1.78	11.56	\	\	3.96	12.22	\

Table 1.8 RMS (bias) of difference in different daylight condition cases (HRRR-AK 12 hours products minus RAOBS); ZWD: Zenith Wet Delay; ZHD: Zenith Hydrostatic Delay; ZTD: Zenith Total delay.

	PANC	PASN	PANT	All	All ZWD	All ZHD	All ZTD
Day time	1.74 (0.92)	2.28 (1.35)	2.54 (1.47)	2.15 (1.10)	14.01 (7.15)	4.21 (0.68)	14.97 (7.83)
Night time	1.39 (0.20)	1.70 (0.65)	1.85 (0.49)	1.66 (0.49)	10.80 (3.21)	4.84 (1.73)	11.80 (4.94)

Table 1.9 Statistics (bias and RMS difference or standard deviation of difference) adapted from previous studies of different NWP products in predicting delay-related parameters, including PWV, ZWD and ZTD. RMS and bias computed from model minus reference data (unit, mm). Last three rows are the statistics of HRRR-AK listed as winter performance-summer performance (average performance).

Initial Data / study field	NWP model	Ref. data	Bias	Standard dev. / RMS	Time-span	Literature source
ECMWF/PWV	MM5	GPS	4.0-5.6	2.3 - 6.7 ^c	July - Oct., 1999	Table 5 [Pacione <i>et al.</i> , 2001]
ECMWF/PWV ^a	\	GPS	0	3.4 ^c	2005-2007	Table 4 [Bock and Nuret, 2009]
NCEP-I/PWV ^a	\	GPS	0.7	5.4 ^c	2005-2007	Table 4 [Bock and Nuret, 2009]
NCEP-II/PWV ^a	\	GPS	2.2	5.3 ^c	2005-2007	Table 4 [Bock and Nuret, 2009]
ECMWF/ZWD	MM5	GPS	2.7	14.3	1999	Table 3 [Behrend <i>et al.</i> , 2002]
ECMWF/ZWD	MM5	VLBI ^d	10.3	14.3	1999	Table 3 [Behrend <i>et al.</i> , 2002]
ECMWF/ZTD ^b	\	GPS	\	9.5 – 13.0 ^c	Jan. 2008–Mar. 2010	Section 3 [Cong <i>et al.</i> , 2012]
MADIS/ZTD	MM5\LAPS	GPS	10.5	14.3 ^c	Jun. 2004 - Aug. 2007	Table 1 [Foster <i>et al.</i> , 2013]
<i>RAP or NAM /PWV</i>	<i>WRF</i>	<i>RAOBS</i>	<i>0.33-1.33 (0.63)</i>	<i>1.16-2.65 (1.96)</i>	<i>Jun.2010 – Sep. 2011</i>	<i>HRRR-AK</i>
<i>RAP or NAM /ZWD</i>	<i>WRF</i>	<i>RAOBS</i>	<i>2.16-8.61 (4.10)</i>	<i>7.57-17.25 (12.72)</i>	<i>Jun.2010 – Sep. 2011</i>	<i>HRRR-AK</i>
<i>RAP or NAM /ZTD</i>	<i>WRF</i>	<i>RAOBS</i>	<i>2.33-10.92 (5.88)</i>	<i>8.74-17.79 (13.78)</i>	<i>Jun.2010 – Sep. 2011</i>	<i>HRRR-AK</i>

^a The statistics of 6-hourly model outputs and the original unit was kg/m² that has been converted to mm [Bevis *et al.*, 1992].

^b The bias of difference and NWP simulate model is not available and its standard deviation listed is as winter-summer.

^c Standard deviation of difference and the others is RMS.

^dVery-Long-Baseline Interferometry (VLBI).

Chapter 2 Robust Atmospheric Filtering of InSAR Data Based on Numerical Weather Prediction Models ²

2.1 Abstract

Finding robust solutions for the mitigation of atmospheric phase delay patterns from Synthetic Aperture Radar Interferometry (InSAR) observations is currently one of the most active research topics in radar remote sensing. Recently, many studies have analyzed the performance of numerical weather prediction (NWP) models for this task, yet, despite significant efforts that were put into optimizing model parameterizations, most of these studies conclude that current NWPs are not able to robustly reproduce the atmospheric phase delay structures that affect SAR interferograms.

Despite these previous findings, we have revisited the application of NWPs for atmospheric correction using a different analysis strategy. In contrast to earlier studies, which assessed the quality of NWP-derived phase screen data, we have studied NWPs from a statistical angle by analyzing whether they are able to provide realistic information about the statistical properties of atmospheric phase signals in InSAR data. The two main findings of this study are: (1) that NWPs are indeed able to robustly predict statistical properties of atmospheric phase screens; and (2) that NWPs underestimate these statistical properties by a scaling factor that depends on the area's surface topography but not on its climatic conditions. Based on these findings, we developed a new concept for atmospheric mitigation that is using NWP-derived statistical parameters to condition the design of an optimal atmospheric phase filter. We found that this filter concept outperforms other more conventional filtering methods.

2.2 Introduction

Synthetic Aperture Radar (SAR) Interferometry (InSAR) is recognized as an

² Gong W., Meyer J. F., Liu S. Z., and Hanssen R., Robust Atmospheric Filtering of InSAR Data based on Numerical Weather Prediction Models, manuscript prepared for submission to IEEE Transactions on Geoscience and Remote Sensing

important technique for the observation of surface deformation over large areas and long time spans. The capacity of InSAR has been demonstrated extensively in the last decade by a wealth of test studies where InSAR was used for monitoring a multitude of geophysical deformation signals [Amelung *et al.*, 2000; Fielding *et al.*, 1998; Hoffmann *et al.*, 2001; Hooper *et al.*, 2004; Lu *et al.*, 2000; Meyer *et al.*, 2007; Ryder *et al.*, 2007; Singhroy *et al.*, 2007; Wright *et al.*, 2003]. While these studies showcase the great potential of this technology, they also indicate that the performance and reliability of InSAR is limited by the influence of the neutral atmosphere on InSAR phase observables.

In differential interferograms, for which topography-related phase components were already removed, the task of atmospheric mitigation basically corresponds to the separation of atmospheric and deformation-related phase components. For this separation to succeed, the spatio-temporal properties of the atmospheric and deformation-related signals have to differ in some aspects. Furthermore, some information about either the deformation or the atmospheric signal needs to be available to design a separation concept. In geophysical applications, where the surface deformation is often unknown, two types of atmospheric information are integrated to enable this separation: (1) spatially explicit atmospheric phase delay maps or; (2) statistical parameters expressing the spatial and/or temporal properties of the atmospheric delay.

Over the past decade, numerous solutions for the problem at hand have been proposed that can be grouped into the previously mentioned two categories: To derive *statistical information about the atmosphere* (category 1), it is usually assumed that the atmospheric signal is uncorrelated in time (as SAR images are usually acquired with more than 1 day time separation) [Emardson *et al.*, 2003]. Furthermore, it is assumed that the atmospheric signal is an isotropic Gaussian process [Wei *et al.*, 2010], whose correlation length can be described by the slope of its power spectral density (often derived using Kolmogorov's theory of turbulent gases) [Knospe and Jonsson, 2010]. Based on these concepts, spatio-temporal filters are designed and applied to redundantly sampled stacks of SAR data for atmospheric signal mitigation [Berardino *et al.*, 2002; Ferretti *et al.*, 2001; Hanssen, 2001; Hooper *et al.*, 2012]. There are several issues with this approach: (1) the

assumption of isotropic Gaussian behavior is very simplistic and typically violated; (2) while Kolmogorov's theory is a reasonable approach to describe the spatial correlation properties of atmospheric signals, it does not provide information about their variance and co-variance. Hence, the influence of varying weather patterns cannot be modeled without additional information; (3) the previously outlined information is insufficient to determine the optimal length (in time) of the atmospheric filter. This issue is most severe if the temporal sampling realized by a SAR data stack is low. In this case, an incorrect filter length can lead to severe biases in the estimated surface deformation signals.

Explicit atmospheric phase delay maps (category 2) for compensation of atmospheric distortions have been derived using external sensors such as Global Positioning System (GPS) stations [Webley *et al.*, 2002; Xu *et al.*, 2011] or observations from the spaceborne multi-spectral scanners Moderate-Resolution Imaging Spectroradiometer (MODIS) [Li *et al.*, 2005] and Medium Resolution Imaging Spectrometer (MERIS) [Li *et al.*, 2009; Meyer *et al.*, 2008]. GPS-based methods usually are limited by a sparse spatial distribution of observation points (GPS), leading to undersampling of small scale atmospheric patterns. Methods based on multi-spectral scanners suffer from a large temporal difference between the acquisitions of the individual sensors (MODIS), or from dependencies on cloud-free conditions (MODIS and MERIS). Recently, Numerical Weather Prediction (NWP) models were added as a means to derive atmospheric phase delay maps (PSU/NCAR Mesoscale Model(MM5) [Puysegur *et al.*, 2007]; Weather Research and Forecasting Model (WRF) [Liu, 2012]; and Global atmospheric models [Doin *et al.*, 2009]). These studies were motivated by recent improvements in the quality of NWP and by the all-time and all-weather capability of their data. While NWP were applied successfully in isolated test cases, the overall conclusion from existing literature [Foster *et al.*, 2013; Fournier *et al.*, 2011] is that current NWP are not able to robustly reproduce the atmospheric phase delay structures that affect SAR interferograms.

To improve upon the current situation, we have revisited the application of NWP. The selection of NWP was motivated by the fact that weather model data is the only weather information that is available at reasonable resolution, at any time, and for any

location. Our study had two main goals: (1) The identification of signal properties in NWP data that are well correlated with the atmospheric signals in interferograms and, (2) the development of algorithms that enable the utilization of these signal properties for atmospheric correction.

Through an extensive analysis of NWP data properties and through an assessment of these properties from an InSAR perspective, we have arrived at the following important and previously unanticipated conclusions: (1) While NWPs are often unable to provide reliable explicit phase delay information at the required accuracy, *NWPs do provide robust information about the statistical properties of atmospheric phase screens (APS) in InSAR data*. This study marks the first time that this capacity of NWPs was discovered; (2) with tested numerical prediction system, *NWP underestimate these statistical properties* by a scaling factor that depends on the area's surface topography but not on its climatic conditions; (3) a *new NWP-based optimal phase filter* was developed that can robustly utilize potentially biased NWP-derived statistical information for atmospheric phase correction; (4) *this new filter concept outperforms other conventionally applied filtering approaches*; and (5) *limited weather modeling skills are required* for using our filtering technique as the statistical approach is less dependent on spatial resolution. For instance, high resolution (in space and time) operational weather forecasting data of the 3 – 5 km grid class is becoming more and more operationally available (e.g., data of the High Resolution Rapid Refresh (HRRR) [Weygandt, 2009] or HRRR-AK models [ARSC, 2012]) and is usually sufficient for our approach.

The remainder of the paper is structured as follows: Some theory about the core issues in atmospheric correction of InSAR data is presented in Section 2.3 using the example of single master InSAR time series processing. An analysis of the performance of NWPs for predicting statistical properties of atmospheric phase screens follows in Section 2.4. Herein, the specifics of the analyzed NWP and proof for the ability of NWPs to predict the spatial variance of atmospheric phase screens are presented in Section 2.4. A concept for the utilization of the (potentially biased) statistics information in atmospheric phase filtering and the performance of this concept is analyzed in Section

2.5. A summary of the main findings together with a discussion of their significance can be found in Section 2.6. A set of acknowledgements conclude the paper.

2.3 Spatial Variance of Time Series Interferograms

2.3.1 Relevant Background on InSAR Time Series Processing

Let $\phi_{p,i}$ be the unwrapped differential interferometric (d-InSAR) phase for scatter p in interferogram i that is composed from SAR echoes acquired at different time ($\psi_{p,i}(t_1)$ and $\psi_{p,i}(t_2)$) that can be decomposed into following signal elements [Hanssen, 2001]

$$\begin{aligned}\phi_{p,i}(\Delta t, B) &= [\psi_{p,i}(t_1) - \psi_{p,i}(t_2)] - \phi_{p,i,topo}(B) \\ &= \phi_{p,i,\Delta topo}(B) + \phi_{p,i,defo}(\Delta t) + \phi_{p,i,orbit} + \phi_{p,i,atm}(\Delta t) + \phi_{p,i,noise}\end{aligned}\quad (2.1)$$

in which $\phi_{p,i,\Delta topo}(B)$ is the (baseline-dependent) topography residual after subtracting a best available digital elevation model (DEM), $\phi_{p,i,defo}(\Delta t)$ is the (temporal baseline dependent) phase contributed by the scatterer's movement along the line-of-sight (LOS) direction, $\phi_{p,i,orbit}$ is the phase introduced by inaccuracies in the satellite orbits, $\phi_{p,i,atm}(\Delta t)$ is the difference in atmospheric delay at the two image acquisition times that can be further decomposed into slave component $\phi_{p,i,s-atm}$ and master component $\phi_{p,i,m-atm}$, and $\phi_{p,i,noise}$ is the phase noise term (e.g., system thermal noise and decorrelation noise). In geophysical applications, where temporal baselines are long to emphasize surface deformation, the d-InSAR phase is decorrelated in most pixels and can only be analyzed at a few so called phase stable scatterers. At the location of these scatterers, phase noise $\phi_{p,i,noise}$ is small by definition and is therefore ignored in the following considerations.

It is the goal of d-InSAR time series analysis to extract $\phi_{p,i,defo}(\Delta t)$ from the phase signal $\phi_{p,i}(\Delta t, B)$ of N interferograms (see Eq. (2.1)). Two different d-InSAR processing methodologies have been developed to achieve this goal that, among other things, differ in the strategies that are applied for selecting suitable interferograms: In Persistent

Scatterer Interferometry (PSI) [Ferretti *et al.*, 2000; Hooper *et al.*, 2012] interferograms are formed between one unique master image and all other images in a SAR data stack, while in Short Baselines Subset (SBAS) InSAR [Lanari *et al.*, 2007] interferograms are selected from all possible image pairs based on their spatial and temporal baselines. Out of these two choices, we focus on PSI-type methods for the following explanations. Note, however, that the developed theory is largely independent of the chosen d-InSAR time series analysis method.

In PSI, we construct a single-master stack of N interferograms from a time series of $N+1$ SAR acquisitions. The phase $\phi_{p,i}(\Delta t, B)$ of these interferograms is referenced to the acquisition time t_0 of the master image. For simplicity, we define $t_0 = 0$ resulting in $\Delta t = t$. We separate $\phi_{p,i,\Delta topo}(B)$ from $\phi_{p,i,defo}(t)$ using their different dependencies on t and B . We also remove $\phi_{p,i,orbit}$ by detrending all interferograms using a best fitting plane. Hence, after these processing steps, the pre-processed interferograms reduce to:

$$\tilde{\phi}_{p,i}(t) = \phi_{p,i,defo}(t) + \phi_{p,i,atm}(t) + \varepsilon_i \quad (2.2)$$

where ε_i is a nuisance term containing residuals of the largely eliminated signals $\phi_{p,i,\Delta topo}(B)$, $\phi_{p,i,orbit}$, and $\phi_{p,i,noise}$. In the single master image stack, the atmospheric signal $\phi_{p,i,atm}(t)$ in the N interferograms is correlated, as all interferograms contain the atmospheric signal of the master image $\phi_{p,i,m-atm}$. This correlation is commonly removed by estimating and subtracting $\phi_{p,i,m-atm}$ from $\tilde{\phi}_{p,i}(t)$ following one of the approaches described in [e.g., Hooper *et al.*, 2012; Kampes, 2006] and resulting in

$$\begin{aligned} \tilde{\phi}_{p,i}(t) &= \tilde{\phi}_{p,i}(t) - \hat{\phi}_{p,i,m-atm}(t) + \varepsilon_i \\ &= \phi_{p,i,defo}(t) + \phi_{p,i,s-atm}(t) + \varepsilon'_i \end{aligned} \quad (2.3)$$

with $\varepsilon'_i = \varepsilon_i + (\phi_{p,i,m-atm} - \hat{\phi}_{p,i,m-atm})$.

To estimate $\phi_{p,i,defo}(t)$ from $\tilde{\phi}_{p,i}$, we usually use the fact that, in most cases,

$\phi_{p,i,defo}(t)$ is correlated across the N interferograms, while $\phi_{p,i,s-atm}(t)$ is statistically independent in time. Under these circumstances, the reconstruction of $\phi_{p,i,defo}(t)$ becomes a signal processing problem in time domain that can be solved by applying a temporal low-pass filter of length T to $\tilde{\phi}_{p,i}(t)$.

$$\hat{\phi}_{p,i,defo}(t) = (\tilde{\phi}_{p,i}(t))_{lp} = \sum_{\tau=0}^t \tilde{\phi}_{p,i}(\tau) \cdot g(t-\tau, T) \quad (2.4)$$

The output of the low pass filter in Eq. (2.4) is considered a good estimate of $\phi_{p,i,defo}(t)$, while the high pass signal $(\tilde{\phi}_{p,i})_{hp}$ is an estimate of the atmospheric signal $\hat{\phi}_{p,i,s-atm}(t)$ under the condition that ε'_i is small.

The problem with this approach is that some information on the correlation length of $\phi_{p,i,defo}(t)$ is needed to appropriately parameterize the shape and length of the applied low-pass filter in Eq. (2.4). In many cases, such information is not available and setting up the parameters of the low-pass filter becomes difficult. In fact, defining the parameters of the temporal low-pass filter has been identified as one of the main issues in PSI processing [Alshawaf, 2013].

Alternative approaches for removing $\phi_{p,i,s-atm}(t)$ from $\tilde{\phi}_{p,i}(t)$ usually involve the integration of external information about the atmospheric state during image acquisition time produced by NWP [Wadge et al., 2002]. These approaches use external atmospheric phase maps from a diverse set of sources to derive an estimate $\hat{\phi}_{p,i,s-atm}(t)$ of the atmospheric phase delay and reduce it from the data. So far, none of the developed methodologies have proven reliable or accurate enough for operational atmospheric correction [Foster et al., 2013; Fournier et al., 2011].

In the following we will develop an alternative idea for atmospheric correction that is based on using NWP produced external knowledge about the *statistical properties* of the atmospheric delay as a prior for determining filtering parameters in Eq. (2.4).

2.3.2 Spatial Variance of Pre-processed Interferograms

2.3.2.1 Theory of Spatial Variance Composition

Let us assume that $\tilde{\phi}_{p,i}(t)$ is the spatially unwrapped interferometric phase at phase stable scatterer p after removal of $\phi_{p,i,\Delta topo}(B)$ and $\phi_{p,i,orbit}$. Let us also assume that we have M phase stable scatterers in N pre-processed single master interferograms and that $\tilde{\phi}_{p,i} \forall p$ resembles a Gaussian process with zero spatial mean, whose signal power can be described by its spatial variance σ_i^2 . We will use σ_*^2 to denote the spatial variance of the individual phase components in interferogram i , computed from all M phase stable scatterers in the interferogram.

In most situations the ground deformation signal is physically decoupled from the atmospheric phase delay patterns and we can assume that the phase components $\phi_{p,i,defo}(t)$ and $\phi_{p,i,s-atm}(t)$ are statistically independent. If we further assume that ε'_i in Eq. (2.3) is negligible, then the spatial phase variance of interferogram i (σ_i^2) can be written as:

$$\begin{aligned}\sigma_i^2 &= \frac{1}{M} \sum_{p=1}^M \tilde{\phi}_{p,i}^2(t) \\ &= \frac{1}{M} \sum_{p=1}^M (\phi_{p,i,defo}^2(t) + \phi_{p,i,s-atm}^2(t)) \\ &= \sigma_{i,defo}^2 + \sigma_{i,s-atm}^2\end{aligned}\tag{2.5}$$

In Eq. (2.5), $\sigma_{i,defo}^2$ corresponds to the ground motion variance time series indicating changes in the deformation signal with time. If multiple independent deformation sources exist in a study area, $\sigma_{i,defo}^2$ is the superposition of the contributions from every source.

2.3.2.2 Stochastic Constraints for Atmospheric Filter Design

The estimation problem in Eq. (2.4) is the identification of the temporal low-pass filter $g(t-\tau, T)$ that correctly recovers $\sigma_{i,defo}^2$ from σ_i^2 . Hence, available statistical

information about either $\phi_{p,i,defo}(t)$ or $\phi_{p,i,s-atm}(t)$ can be used to constrain $g(t-\tau, T)$ and condition the estimation problem in Eq. (2.4). As in geophysical applications of InSAR, $\phi_{p,i,defo}(t)$ and its statistical properties are often unknown, we propose that prior information about $\sigma_{i,s-atmo}^2$ should be used to constrain $g(t-\tau, T)$.

External information about the atmospheric phase delay patterns in image acquisition can be obtained from various sources, most of which are highlighted in Section 2.2. Due to reasons explained in the same section, we consider NWP models as the most appropriate external source of atmospheric information. Hence, in the following section, we analyze if NWPs are capable of providing reliable information about $\sigma_{p,i,s-atm}^2$ in order to support the atmospheric filtering process in Eq. (2.4).

2.4 The Performance of NWPs in Predicting Atmospheric Phase Variance

2.4.1 Atmospheric Spatial Variance and Empirical Model

In order to determine if NWPs can provide reliable information about $\sigma_{p,i,s-atm}^2$, we improve the approach proposed in [Gong *et al.*, 2011] that analyze linear correlations between atmospheric signal spatial variance derived from SAR interferograms $(\sigma_{i,atm}^2)_{ifg}$ and NWP products $(\sigma_{i,atm}^2)_{nwp}$.

$$(\sigma_{i,atm}^2)_{nwp} = a \cdot (\sigma_{i,atm}^2)_{ifg} + \xi_i \quad (2.6)$$

Parameter a in Eq. (2.6) is the slope coefficient of the best fitting linear regression line and ξ_i is the model residual that is assumed unbiased and Gaussian distributed. In contrast to conventional regression analyses, Eq. (2.6) has no offset parameter in order to avoid negative values on the right side of Eq. (2.6) that hold no physical meaning. We estimate the slope coefficient \hat{a} using least-squares regression analysis and calculate the coefficient of determination R^2 to evaluate the NWP performance. If $\hat{a} \approx 1$, the NWP reproduces the same power as the equivalent atmospheric signal observed by SAR. R^2

allows us to quantify the goodness of fit between $(\sigma_{i,atm}^2)_{ifg}$ and $(\sigma_{i,atm}^2)_{nwp}$. We apply regression analysis to several test sites around the globe to establish whether or not NWP's are able to estimate $\sigma_{p,i,s-atm}^2$.

2.4.2 Real Data Analysis

We re-analyze the study results of *Liu* [2012], who investigated the performance of NWP to predict the spatial patterns of APS by comparing InSAR- and NWP-derived atmospheric phase delay signals over four test sites, including Mexico City, Mexico, the Big Island in Hawaii, USA, The Netherlands and a test site in south Australia (South Aus.). From their results, *Liu* [2012] suggested limited pixel-wise correlation between interferogram-derived and predicted APS. In contrast to the study by *Liu* [2012], we analyzed their data for the accuracy of the captured atmospheric phase variance.

To maintain an equivalent atmospheric signal, both NWP and interferometric APS data were processed to identical resolutions. Also, both data were detrended using a linear regression surface. Due to the presence of strong surface subsidence signals in and around the test site at Mexico City [*Osmanoğlu et al.*, 2011], affected areas were masked out during processing.

2.4.2.1 Study Areas

The study areas were selected to be geographically distanced from each other and represent unique climate and topography conditions. They can be categorized into two main groups based on their terrain properties, including (1) flat regions (South Australia and the Netherlands) and (2) mountain regions (Big Island in Hawaii and scenes over Mexico City). In the flat regions, the captured atmospheric signal is dominated by turbulent mixing processes in the atmosphere, while in mountain areas, differences in the vertical refractivity profiles during acquisition of master and slave image can add topography-correlated signals to the observed interferometric phase [*Hanssen*, 2001]. The detailed topography and climate conditions of all test sites are well described in *Liu* [2012]. As an indicator of the level topographic variation within each test site, the

standard deviation of surface topography σ_{DEM} was calculated from Space Shuttle Topography Mission (SRTM) Digital Elevation Models (DEMs) covering the SAR frames. σ_{DEM} is listed in the last column of Table 2.1.

2.4.2.2 APSs Isolation from Interferograms and NWP Products

Environment Satellite (ENVISAT) Advance SAR (ASAR) images in descending orbit direction acquired between 2003 and 2009 were processed, together with SRTM DEM information and precise orbit information provide by European Space Agency (ESA), to generate unwrapped differential atmospheric phase screens (APSs). There are six to nine InSAR APSs per test sites as listed in the Table 2.1. The acquisition times of SLCs favor the October to April time period due to the preferable coherence conditions during the local winter season of test sites. The baseline criteria for interferograms selection were set to limit perpendicular baselines to $|B_{\perp}| < 300$ m and temporal baselines to $|B_t| < 70$ days in order to minimize non-atmospheric signal components, maximize coherence, and ease phase unwrapping [Liu, 2012]. Multi-looking was applied both before and after phase unwrapping: The prior one (25px in azimuth and 5px in range) is for improving unwrapping quality, while the second multi-looking is performed to match the resolution of the NWP outputs at 1 km. Spatial phase ramps were removed to reduce orbit residual. Examples and more details on the APS processing procedure can be found in [Liu, 2012].

Three dimensional (3D) atmospheric models for all test sites were simulated using the WRF model (version 3.1), which generates 3D fields of the main atmospheric parameters temperature, total pressure, partial water vapor pressure and cloud water physical parameters every 10 minutes. Final Analyses (FNL) data, provided by the National Centers for Environment (NCEP), were used as initial boundary conditions for all WRF runs [UCAR, 2013a]. A simple four nests domain forecast initialized at 27 km and nested down to 1 km in lateral sampling was applied. Furthermore, the system was set up to generate 3D atmospheric data with 28 vertical layers and at 10 minute time steps. The details of the WRF physical parameterization can be found in Liu [2012]. The refractivity

index of each grid cell is computed from the predicted 3D atmospheric parameter fields using an approach published in *Liu* [2012] and *Hanssen* [2001]. The 2D atmospheric signal delay map is obtained from an integration of the refractivity profiles along the satellite's line-of-sight direction. Finally, a deramping is applied to the WRF delay maps to maintain signal equivalency to InSAR derived APS. The detrended delay maps from InSAR and NWP are used to compute $(\sigma_{i,atm}^2)_{ifg}$ and $(\sigma_{i,atm}^2)_{nwp}$.

2.4.2.3 Linear Regression Analysis of Spatial Atmospheric Variance

A least-squares regression model was applied to all computed $(\sigma_{i,atm}^2)_{ifg}$ and $(\sigma_{i,atm}^2)_{nwp}$ data pairs at every test site. The best fitting regression slopes, computed according to Eq. (2.6), are shown in Figure 2.1. The results for scale factor \hat{a} and goodness of fit parameter R^2 per site are shown in Table 2.1.

Table 2.1 and Figure 2.1 reveal two main relevant findings: (1) The plots in Figure 2.1 and the R^2 values in Table 2.1 indicate excellent correlation between $(\sigma_{i,atm}^2)_{ifg}$ and $(\sigma_{i,atm}^2)_{nwp}$, with a minimum 67% of the data being explained by Eq. (2.6) for all four sub-test sites. This fair correlation indicates that *the NWP model is providing reliable information about the statistical properties of atmospheric phase screens affecting InSAR data.* (2) While the data show a significant linear relationship between $(\sigma_{i,atm}^2)_{ifg}$ and $(\sigma_{i,atm}^2)_{nwp}$, the estimated regression slope \hat{a} is (1) usually smaller than 1 (indicating an underestimation of the atmospheric variance by WRF) and (2) differs for different test sites. To investigate the causes for the observed behavior, we analyze \hat{a} further in the following section.

2.4.2.4 Variability of the Linear Scale Factor \hat{a}

(1) Dependence of \hat{a} on scene parameters

Comparing the value of slope coefficient estimates and DEM standard deviation, Table 2.1 indicates that the estimated slope values \hat{a} correlates with the amount of

topography at the test sites (quantified by the DEM standard deviation σ_{DEM}). Hence, a second ordinary linear regression analysis

$$\hat{a} = \hat{a}_{topo} \cdot \sigma_{DEM} + \hat{a}_0 \quad (2.7)$$

was carried out to further analyze this relationship. The regression results are plotted in Figure 2.2. It is evident from the regression parameters (R^2 value of approx. 0.9) that there is a significant linear relationship between \hat{a} and σ_{DEM} . The best fitting regression line (gray line in Figure 2.2) has a slope of $\hat{a}_{topo} = 0.63$ and an intercept of $\hat{a}_0 = 0.37$. Hence, in the absence of topography ($\sigma_{DEM} \approx 0$), the parameter \hat{a} of Eq. (2.6) is expected to be $\hat{a} = 0.37$ increasing linearly from there with $\hat{a}_{topo} \cdot \sigma_{DEM}$. Hence, according to these results, the underestimation behavior of the NWP is particularly pronounced for the turbulent delay components of APS, which dominate in flat terrains. The positive value of \hat{a}_{topo} indicates that underestimation is less pronounced for stratified delay signals, which increase in importance with increasing σ_{DEM} . Note that the uncertainties of the slope estimates \hat{a} (determined from Eq. (2.6)) were used for solving Eq. (2.7) and are plotted in Figure 2.2 as error bars.

Based on the derived dependence described in Eq. (2.7) and the known information of σ_{DEM} , the predicted scale factor \hat{a} can be computed for every test site. Together with external $(\sigma_{i,atm}^2)_{nwp}$, it is further applied to predict the empirical value of InSAR atmospheric spatial variance $((\sigma_{i,atm}^2)_{ifg,pred})$ regardless of test sites location as shown in Figure 2.3. This allows us to plot all measurements together and compare them directly. The gray dashed line (non-biased line through origin) is the optimal fit of the data pairs, and it has coefficient of determination R^2 of 0.66 that indicates a fair linear fit to non-biased line. The result suggests its usefulness of the empirical model (Eq. (2.7)) as a tool for $(\sigma_{i,atm}^2)_{ifg,pred}$ prediction based on the knowledge of the NWP simulated $(\sigma_{i,atm}^2)_{nwp}$ and the terrain condition within the study area.

(2) Dependence on NWP parameterization

In previous research [Skamarock, 2004], it was shown that the performance of NWP models for producing small scale atmospheric turbulence signals can depend on the model parameterization. To study the sensitivity of our correlation parameter \hat{a} to changes of model parameters we conducted re-runs of the NWP model over the test sites Hawaii and Mexico City. In a first re-run, we used a new version of WRF (version 3.5 instead of 3.1) for calculating $(\sigma_{i,atm}^2)_{nwp}$. WRF 3.5 differs from earlier version in many aspects of physics, dynamics, initialization, nesting and nudging processing as well as some bugs have been fixed [UCAR, 2013b], which might affect the model behavior. For this test, the same boundary condition, model parameterizations, and model forecast periods (4-11 hours depending on test site) that were applied in WRF 3.1 runs were used.

The results of this analysis are listed in Table 2.2. From the R^2 values at both test sites, we can confirm the previously noted linear correlation between $(\sigma_{i,atm}^2)_{ifg}$ and $(\sigma_{i,atm}^2)_{nwp}$. Compared to the results listed in Table 2.1, the estimated scale factors in this re-run are slightly smaller and the R^2 values are improved when using the updated model.

In a second set of re-runs, we increased the model lead times from 4 - 11 hours to 16 - 28 hours in addition to changing the model version to WRF v3.5. As before, physical parameter settings and boundary conditions remained unchanged. The regression results for these simulations are listed in the second column of Table 2.2. From Table 2.2 we observe a decrease of estimated slope values with increasing model forecasting period. Considering the major contribution of atmospheric phase only interferograms is from the wet delay [Hanssen, 2001], as shown in Table 2.2 the longer forecast period provides smaller slope estimates that indicates NWP simulated wet delay component is getting less with the increasing of model lead times, which also confirms our previous results [Gong *et al.*, 2013].

These results show that the exact value of scale factor \hat{a} does depend on the model

parameterization. Hence, when attempting to use NWP-derived APS information in atmospheric correction of InSAR data, it is important to use the same model setup for all NWP runs associated with a given data stack. A change of model setup will degrade the correlation between $(\sigma_{i,atm}^2)_{ifg}$ and $(\sigma_{i,atm}^2)_{nwp}$ and, hence, reduce the usefulness of NWP data.

2.4.3 Sub-conclusions

Our results show that NWP models can provide valuable information about the statistical properties of APS captured in InSAR data. We have shown that there is a linear relationship between $(\sigma_{i,atm}^2)_{ifg}$ and $(\sigma_{i,atm}^2)_{nwp}$ that is robust across a wide range of test sites. We have also shown that the regression slope \hat{a} is not a fixed value but rather depends on the surface topography of the area of interest and on the parameterization of the used NWP model. Hence, while NWPs like WRF are able to robustly describe the temporal variation of $(\sigma_{i,atm}^2)_{ifg}$ within a data stack, there is an unknown scaling factor that needs to be estimated when we attempt to predict $(\sigma_{i,atm}^2)_{ifg}$ from $(\sigma_{i,atm}^2)_{nwp}$.

For all tested parameterizations, NWP is consistently underestimating $(\sigma_{i,atm}^2)_{ifg}$ (corresponding to $\hat{a} < 1$) mostly due to an underestimation of the turbulence component of atmospheric delay. Further tests are needed to understand the underestimation phenomenon in NWP fine resolution products observed in this study.

2.5 A Robust Optimal Atmospheric Phase Filter Based on NWP Data

Based on the results presented in Section 2.4, a concept for the utilization of statistical atmospheric information in atmospheric phase filtering is introduced in this section.

To conduct a separation of atmospheric and motion-related phase component in an optimized way, the shape of filter kernel in Eq. (2.4) is a key point. As mentioned in Section 2.2, determining the proper design of the temporal atmospheric phase filter without making unjust assumptions about the temporal behavior of the motion signal

remains a difficult issue. Hence, in our approach, we interpret atmospheric phase filtering as the process of accurately extracting $\phi_{p,i,defo}$ from the phase $\tilde{\phi}_{p,i}$ of post processed interferograms. Following this paradigm, we propose to constrain the parameter of the temporal low-pass filter $g(t-\tau, T)$ in Eq. (2.4) using NWP-produced atmospheric variance information $(\sigma_{i,atm}^2)_{nwp}$. In the following, we describe how NWP data can be integrated into solving Eq. (2.4) given the sub-conclusions in Section 2.2.

2.5.1 Optimal Atmospheric Phase Filtering through Correlation Maximization

For simplicity, we use a temporal low-pass filter of Gaussian shape in Eq. (2.4), reducing the optimization problem in Eq. (2.4) to the estimation of the filter length parameter T that optimizes the separation of $\phi_{p,i,defo}$ from $\tilde{\phi}_{p,i}(t)$ given $(\sigma_{i,atm}^2)_{nwp}$. Here, filter length T corresponds to the half width of the kernel. To avoid confusion, hereafter T will be referred to as window size of the Gaussian low pass filter.

Following the pre-processing steps in Sections 2.3 and 2.4, the phase time series $\tilde{\phi}_{p,i}$ is derived (see Eq. (2.3)). For a time series of N interferograms, we find the optimal global window length \hat{T} of the atmospheric phase filter $g(t-\tau, \hat{T})$ by searching for the parameters \hat{T} and \hat{a}_T that optimize the linear correlation between spatial variance $(\sigma_i^2)_{hp}$ of high passed signal $(\tilde{\phi}_{p,i})_{hp}$ and $(\sigma_{i,s-atm}^2)_{nwp}$ as shown in Eq. (2.8).

$$(\sigma_i^2)_{hp} = \frac{1}{M} \sum_{p=1}^M \left[\tilde{\phi}_{p,i}(t) - \sum_{\tau=0}^t \tilde{\phi}_{p,i}(\tau) \cdot g(t-\tau, \hat{T}) \right]^2 \quad (2.8)$$

Mathematically, we minimize the L2 norm of $\Delta\sigma_{atm}$ (Eq. (2.9b)) by applying a grid search over the parameters \hat{T} and \hat{a}_T constrained by Eq. (2.6) (Eq. (2.9a)).

$$\Delta\sigma_{atm} = (\sigma_{i,s-atm}^2)_{nwp} - \hat{a}_T \cdot (\sigma_i^2)_{hp} \quad (2.9a)$$

$$\|\Delta\sigma_{atm}\|_2 = \min (2.9b)$$

Note that the slope parameter a_T is treated as an unknown in the algorithm in response to our finding that a_T is not known a-priori.

The search space for T is bounded within $[T_l, T_u]$ that is gridded by the satellite revisiting time. The lower bound T_l is selected to be one satellite repeat cycle so that if images are acquired regularly, there are at least three samples within the window size of the Gaussian window. The upper bound T_u is selected to limit the numbers of iterations; e.g. 280 days is used in following experiment that can be other larger numbers. The window size within $[T_l, T_u]$ that satisfies Eq. (2.9) is \hat{T} . No error bounds are introduced for a_T as our experiments show that a_T generally converges quickly towards \hat{a}_T .

Using the proposed approach, three major products can be obtained: (1) the estimated deformation time series $\hat{\phi}_{p,i,defo}$; (2) the parameters of an optimal global low pass filter; and (3) an estimate of the phase variance time series $(\sigma_{i,defo}^2)_{ifg}$, which provides information on important temporal properties of the unknown deformation fields within the study area that can be useful for further post processing steps such as deformation filed modeling.

2.5.2 Performance Assessment Using Synthetic Data

To demonstrate and evaluate the performance of our optimal atmospheric phase filter (OAPF), we first report on simulated experiments. For this experiment, a stack of numerically simulated single master interferograms as well as synthetic NWP differential delay maps were created using the following approach.

2.5.2.1 Synthetic Data Preparation

The series of synthetic pre-processed interferogram (according to Eq. (2.3)) were generated based on the parameters of the current X-band spaceborne SAR system, TerraSAR-X, with 11 days revisiting time. A total of 5000 persistent scatterers spread

across an area of $1000 \times 1000 \text{ pixel}^2$ were simulated per image. If regularly sampled at 11 day intervals, the stack contains 74 interferograms spread over more than 2 years time span. To approximate real acquisition conditions, e.g. gaps in the time series, only 55 of the 74 images are used in the experiment.

Four independent motion fields with similar spatial correlation lengths but different motion intensity were simulated within the study area. The velocity of their linear deformation trends was kept within $\pm 1 \text{ cm/yr}$ to simulate small deformation conditions. The simulated interferometric phases were pre-processed according to Eq. (2.3) resulting in $\tilde{\phi}_{p,i}$.

Time series of simulated APS $\phi_{p,i,atm}(\Delta t)$ were generated using fractal theory [Kampes, 2006]. To obtain synthetic NWP products $(\phi_{p,i,s-atm})_{nwp}$, an atmospheric error signal $(\delta_{i,s-atm})$ was synthetically generated using a fractal algorithm such that $(\phi_{p,i,s-atm})_{nwp}$ is the summation of $\delta_{i,s-atm}$ and $\phi_{p,i,s-atm}$. Hence, $\delta_{i,s-atm}$ is spatial correlated rather than random noise and satisfies physical reality. Finally, $(\sigma_{i,s-atm}^2)_{nwp}$ is computed from $(\phi_{p,i,s-atm})_{nwp}$ and scaled to simulate the scale effect that was observed in the experiment of Section 2.4.

This data simulation approach is to guarantee the synthetic data reflects physical reality and is commensurate with the main steps in real data processing. The synthetically generated $(\sigma_{i,s-atm}^2)_{ifg}$ per pre-processed interferogram is similar to the real data shown in Section 2.4. For instance, the spatial phase variance $(\sigma_{i,s-atm}^2)_{ifg}$ for the Mexico case is ranging from 0.42 to 1.72 rad^2 for C-band interferograms [Liu, 2012], which is similar to the range of our simulated data (see Figure 2.4). In Figure 2.4, the best linear fit for $\sigma_{i,s-atm}^2$ and $(\sigma_{i,s-atm}^2)_{nwp}$ data pairs is denoted by dashed gray line with a scaling factor of 0.62 and R^2 is 0.69 for 55 images.

2.5.2.2 Synthetic Data Processing Using the Optimal Atmospheric Phase Filter

To evaluate the performance of the optimal atmospheric phase filter, we conduct two comparative analyses: First, we compare the filtered deformation time series $(\tilde{\phi}_{p,i})_{lp}$ produced by our optimal phase filter to the true deformation time series $\phi_{p,i,defo}$. However, as $\phi_{p,i,defo}$ cannot be estimated perfectly from a small number of noisy observations, a comparison of $(\tilde{\phi}_{p,i})_{lp}$ to $\phi_{p,i,defo}$ provides a slightly biased evaluation of the filter's performance.

Therefore, we perform a second, more realistic comparison that takes advantage of the fact that the true deformation time series $\phi_{p,i,defo}$ is known. Under these conditions, we can define an ideally filtered time series as the one that minimizes the mean-square-error (MSE) τ_{lp_ideal} :

$$\tau_{lp_ideal} = \frac{1}{M} \sum_{p=1}^M \left[\phi_{p,i,defo} - \sum_{\tau=0}^t \tilde{\phi}_{p,i}(\tau) \cdot g(t-\tau, \hat{T}_{ideal}) \right]^2 \quad (2.10)$$

Using Eq. (2.10), we can determine window size \hat{T}_{ideal} that is generating the best possible approximation of $\phi_{p,i,defo}$ based on the data in time series $\phi_{p,i}$. We denote the spatial variance of the low passed signal through ideal filter $g(t, \hat{T}_{ideal})$ as $(\sigma_i^2)_{lp_ideal}$. Our optimal filter performs ideally if its output is identical to $(\sigma_i^2)_{lp_ideal}$.

Figure 2.5 provides an example of a comparison of $(\sigma_i^2)_{lp_ideal}$ (black plus markers) and $(\sigma_i^2)_{lp_hat}$ (gray square markers). For completeness, also the true (noise free) deformation time series $\sigma_{i,defo}^2$ (gray solid line) and the variance of the original unfiltered data σ_i^2 (gray line with cross markers) are shown. Analysis of Figure 2.5 allows for a comparison of the overall performance of our optimal filter in estimating $\phi_{p,i,defo}(t)$ from

$\tilde{\phi}_{p,i}$. It can be seen that, despite the considerable contamination of the original time series with atmospheric signals, the optimal filter is effective in extracting $\phi_{p,i,defo}(t)$. Furthermore, the filter output $(\phi_{p,i})_{lp_{\hat{T}}}$ is almost identical to the ideal filter result defined by $(\phi_{p,i})_{lp_{T_{ideal}}}$. Thus, our optimal filter is capable of reconstructing the deformation time series with the assistance of $(\phi_{p,i,s-atm})_{nwp}$ without requiring any prior information about the properties of the deformation signal.

2.5.3 Assessment of convergence properties

As for any iterative process, convergence to the true solution is not guaranteed in our algorithm. In order to evaluate how robustly the algorithm converges to the correct solution for the sought filter parameter T , we have conducted an extensive Monte Carlo experiment [Metropolis and Ulam, 1949].

In these experiments, we define the filter parameter T to be successfully estimated, if the difference between the estimate \hat{T} produced by the optimal filter and the filter length T_{ideal} is less or equal 22 days ($|\hat{T} - T_{ideal}| \leq 22$ days). In numerical simulations we study the likelihood of convergence to the true solution as a function of the quality of the prior information $(\sigma_{i,s-atm}^2)_{nwp}$, quantified by the R^2 between data pairs of $(\sigma_{i,s-atm}^2)_{ifg}$ and $(\sigma_{i,s-atm}^2)_{nwp}$ (low R^2 corresponds to low quality prior information). We expect the likelihood of convergence to decrease with decreasing quality of $(\sigma_{i,s-atm}^2)_{nwp}$.

The results of the analysis are shown in Figure 2.6 that shows varying degrees of R^2 versus the likelihood of convergence given the above defined criterion (the left y-axis). For each R^2 condition, we generated 60 statistically independent stacks of synthetic data using the approach outlined in Section 2.2, and every marker in Figure 2.6 represents the average performance within these 60 data points. For instance, the R^2 value of 0.7 represents the average performance when $R^2 \in (0.6, 0.7]$. The gray dotted line with

circles shows the success rate in determining \hat{T} as a function of R^2 . The black dotted line with crosses shows the residual ratio Δ_{res} that indicates the difference between the output of the optimal filter and the ideal filter that is mathematically described by Eq. (2.11). There, $\tau_{lp_{\hat{T}}}$ and $\tau_{lp_{ideal}}$ are the mean-square-error between $\phi_{p,i,defo}$ and the output of the optimal phase filter and the ideal filter, respectively.

$$\Delta_{res} = \left| \tau_{lp_{\hat{T}}} - \tau_{lp_{ideal}} \right| / \tau_{lp_{ideal}} \quad (2.11)$$

For all analyzed conditions, the difference between the optimal filter and the ideal filter was less than 2%, indicating the NWP-aided optimal filtering approach doesn't introduce significant errors under current evaluation criteria. The black dotted line in Figure 2.6 also suggests that Δ_{res} is independent of R^2 (values of Δ_{res} are quantified on the second y-axis of Figure 2.6). However, as expected, Figure 2.6 shows that the convergence rate of the optimal phase filter does depend on R^2 . For example, the success rate is higher than 70%, if the R^2 between $(\sigma_{i,s-atm}^2)_{nwp}$ and $(\sigma_{i,s-atm}^2)_{ifg}$ is higher than 0.7.

2.6 Conclusions

This study investigated the InSAR data and NWP products over four test sites to evaluate the quality of NWP predicted atmospheric delay statistics and assessed performance of developed algorithms by analyzing the synthetic data sets. We addressed two interrelated scientific issues:

(1) Based on extensive comparisons of NWP and InSAR data with different climate and topography conditions, we determined that NWP models can provide valuable information about the statistical properties of APS captured in InSAR data. Specifically, we have shown that there is a linear relationship between $(\sigma_{i,atm}^2)_{ifg}$ and $(\sigma_{i,atm}^2)_{nwp}$ that is robust across a wide range of test sites. We have also shown that the slope \hat{a} of the best fitting regression line is usually smaller than 1, indicating an underestimation of $(\sigma_{i,atm}^2)_{ifg}$

by NWP, and that can \hat{a} additionally vary as a function of surface topography and NWP model parameterization.

(2) Based on these findings, we developed a *new NWP-based optimal atmospheric phase filter (OAPF)* that can robustly utilize potentially biased NWP-derived statistical information for atmospheric phase correction. We have determined the performance of this new filter concept and have shown that it comes very close to the theoretically achievable filter optimum. In extensive Monte Carlo simulations, we furthermore determined that the converging rate of the OAPF is higher than 70%, even if the quality of atmospheric prior information is low.

While our filter concept was exemplified using PS-InSAR concepts, the processing flow can be easily adjusted to other time series InSAR techniques like SBAS processing.

2.7 Acknowledgements

This work was support by the NASA Headquarters under the NASA Earth and Space Science Fellowship Program - Grant NNX10AO70H. We thank Prabu Dheenathayalan for supporting data exchange with partner studies. SAR data for this study was provided by ESA.

2.8 References

- Alshawaf, F. (2013), Fusion of InSAR, GNSS, and WRF data for building 2D maps of the propagation delay produced by the atmospheric water vapor, Karlsruhe Institute of Technology, Karlsruhe.
- Amelung, F., S. Jonsson, H. Zebker, and P. Segall (2000), Widespread uplift and 'trapdoor' faulting on Galapagos volcanoes observed with radar interferometry, *Nature*, 407(6807), 993-996.
- ARSC (2012), ARSC High Resolution Rapid Refresh (HRRR), edited, Arctic Region Supercomputing Center <http://weather.arsc.edu/HRRR/>.
- Berardino, P., G. Fornaro, R. Lanari, and E. Sansosti (2002), A new algorithm for surface deformation monitoring based on small baseline differential SAR interferograms, *IEEE Transaction on Geoscience and Remote Sensing*, 40(11), 2375-2383.

- Doin, M. P., C. Lasserre, G. Peltzer, O. Cavalie, and C. Doubre (2009), Corrections of stratified tropospheric delays in SAR interferometry: Validation with global atmospheric models, *Journal of Applied Geophysics*, 69(1), 35-50.
- Emardson, T. R., M. Simons, and F. H. Webb (2003), Neutral atmospheric delay in interferometric synthetic aperture radar applications: Statistical description and mitigation, *Journal of Geophysics Research: Solid Earth*, 108(B5).
- Ferretti, A., C. Prati, and F. Rocca (2000), Nonlinear subsidence rate estimation using permanent scatterers in differential SAR interferometry, *IEEE Transactions on Geoscience and Remote Sensing*, 38(5), 2202-2212.
- Ferretti, A., C. Prati, and F. Rocca (2001), Permanent scatterers in SAR interferometry, *IEEE Transactions on Geoscience and Remote Sensing*, 39(1), 8-20.
- Fielding, E. J., R. G. Blom, and R. M. Goldstein (1998), Rapid subsidence over oil fields measured by SAR interferometry, *Geophysical Research Letters*, 25(17), 3215-3218.
- Foster, J., J. Kealy, T. Cherubini, S. Businger, Z. Lu, and M. Murphy (2013), The utility of atmospheric analyses for the mitigation of artifacts in InSAR, *Journal of Geophysical Research: Solid Earth*, 118(2), 748-758.
- Fournier, T., M. E. Pritchard, and N. Finnegan (2011), Accounting for Atmospheric Delays in InSAR Data in a Search for Long-Wavelength Deformation in South America, *IEEE Transactions on Geoscience and Remote Sensing*, 49(10), 3856-3867.
- Gong, W., F. J. Meyer, and S. Liu (2011), Numerical Weather Model Assisted Time Series InSAR Processing for Geophysical Application, paper presented at ESA FRINGE Workshop, European Space Agency Frascati, Italy, 19-23 September
- Gong, W., F. J. Meyer, P. Webley, and D. Morton (2013), Performance of the high-resolution atmospheric model HRRR-AK for correcting geodetic observations from spaceborne radars, *Journal of Geophysical Research: Atmospheres*, 118(20), 2013JD020170.
- Hanssen, R. (2001), *Radar Interferometry: Data Interpretation and Error Analysis*, 1 ed.,

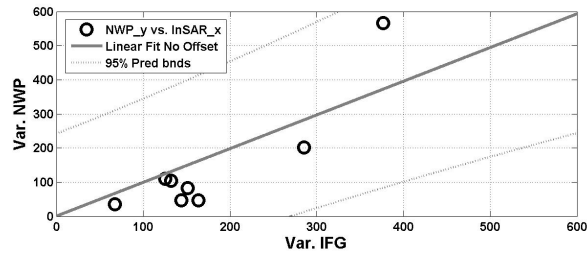
Kluwer Academic Publishers, Netherlands.

- Hoffmann, J., H. A. Zebker, D. L. Galloway, and F. Amelung (2001), Seasonal subsidence and rebound in Las Vegas Valley, Nevada, observed by synthetic aperture radar interferometry, *Water Resources Research*, 37(6), 1551-1566.
- Hooper, A., H. Zebker, P. Segall, and B. Kampes (2004), A new method for measuring deformation on volcanoes and other natural terrains using InSAR persistent scatterers, *Geophysical Research Letters*, 31(23).
- Hooper, A., D. Bekaert, K. Spaans, and M. Arikan (2012), Recent advances in SAR interferometry time series analysis for measuring crustal deformation, *Tectonophysics*, 514–517(0), 1-13.
- Kampes, B. (2006), *Radar interferometry: persistent scatterer technique*, 211 pp., Springer, Dordrecht, the Netherlands.
- Knospe, S. H. G., and S. Jonsson (2010), Covariance Estimation for dInSAR Surface Deformation Measurements in the Presence of Anisotropic Atmospheric Noise, *IEEE Transactions on Geoscience and Remote Sensing*, 48(4), 2057-2065.
- Lanari, R., F. Casu, M. Manzo, G. Zeni, P. Berardino, M. Manunta, and A. Pepe (2007), An Overview of the Small BAseline Subset Algorithm: A DInSAR Technique for Surface Deformation Analysis, in *Deformation and Gravity Change: Indicators of Isostasy, Tectonics, Volcanism, and Climate Change*, edited by D. Wolf and J. Fernández, pp. 637-661, Birkhäuser Basel.
- Li, Z., E. J. Fielding, P. Cross, and R. Preusker (2009), Advanced InSAR atmospheric correction: MERIS/MODIS combination and stacked water vapour models, *International Journal of Remote Sensing*, 30(13), 3343-3363.
- Li, Z., J. P. Muller, P. Cross, and E. J. Fielding (2005), Interferometric synthetic aperture radar (InSAR) atmospheric correction: GPS, moderate resolution Imaging spectroradiometer (MODIS), and InSAR integration, *Journal of Geophysical Research:Solid Earth*, 110(B3).
- Liu, S. (2012), *Satellite Radar Interferometry: estimation of atmospheric delay*, 203 pp, Delft University of Technology.

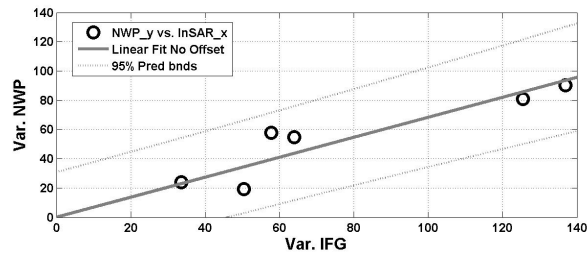
- Lu, Z., C. Wicks, D. Dzurisin, W. Thatcher, J. T. Freymueller, S. R. McNutt, and D. Mann (2000), Aseismic inflation of Westdahl Volcano, Alaska, revealed by satellite radar interferometry, *Geophysical Research Letter*, 27(11), 1567-1570.
- Metropolis, N.; Ulam, S. (1949). "The Monte Carlo Method", *Journal of the American Statistical Association*, 44 (247): 335–341. doi:10.2307/2280232
- Meyer, F.J, S. Gernhardt, and N. Adam (2007), Long-term and seasonal subsidence rates in urban areas from Persistent Scatterer Interferometry, paper presented at Urban Remote Sensing Joint Event, 2007, 11-13 April 2007.
- Meyer, F.J, R. Bamler, R. Leinweber, and J. Fischer (2008), A Comparative Analysis of Tropospheric Water Vapor Measurements from MERIS and SAR, paper presented at IEEE International Geoscience and Remote Sensing Symposium, Boston, USA.
- Osmanoğlu, B., T. H. Dixon, S. Wdowinski, E. Cabral-Cano, and Y. Jiang (2011), Mexico City subsidence observed with persistent scatterer InSAR, *International Journal of Applied Earth Observation and Geoinformation*, 13(1), 1-12.
- Puysegur, B., R. Michel, and J. P. Avouac (2007), Tropospheric phase delay in interferometric synthetic aperture radar estimated from meteorological model and multispectral imagery, *Journal of Geophysical Research: Solid Earth*, 112(B5).
- Ryder, I., B. Parsons, T. J. Wright, and G. J. Funning (2007), Post-seismic motion following the 1997 Manyi (Tibet) earthquake: InSAR observations and modelling, *Geophysical Journal International*, 169(3), 1009-1027.
- Singhroy, V., R. Couture, P. J. Alasset, and V. Poncos (2007), InSAR monitoring of landslides on permafrost terrain in Canada, paper presented at IEEE International Geoscience and Remote Sensing Symposium, Barcelona, Spain.
- Skamarock, W. C. (2004), Evaluating mesoscale NWP models using kinetic energy spectra, *Monthly Weather Review*, 132(12), 3019-3032.
- UCAR (2013a), NCEP FNL Operational Model Global Tropospheric Analyses, continuing from July 1999, <http://rda.ucar.edu/datasets/ds083.2/>.
- UCAR (2013b), WRF Model Version 3.5: Updates, in *WRF users page*,

<http://www.mmm.ucar.edu/wrf/users/wrfv3.5/updates-3.5.html>.

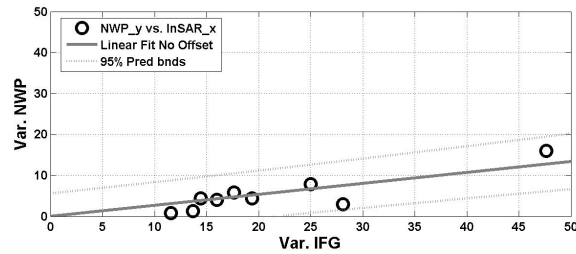
- Wadge, G., P. W. Webley, I. N. James, R. Bingley, A. Dodson, S. Waugh, T. Veneboer, G. Puglisi, M. Mattia, D. Baker, S. C. Edwards, S. J. Edwards, P. J. Clarke (2002), Atmospheric models, GPS and InSAR measurements of the tropospheric water vapour field over Mount Etna, *Geophysical Research Letters*, 29(19).
- Webley, P. W., R. M. Bingley, A. H. Dodson, G. Wadge, S. J. Waugh, and I. N. James (2002), Atmospheric water vapour correction to InSAR surface motion measurements on mountains: results from a dense GPS network on Mount Etna, *Physics and Chemistry of the Earth*, 27(4-5), 363-370.
- Wei, M., D. Sandwell, and B. Smith-Konter (2010), Optimal combination of InSAR and GPS for measuring interseismic crustal deformation, *Advances in Space Research*, 46(2), 236-249.
- Weygandt, S. S., T. G. Smirnova, S. G. Benjamin, K. J. Brundage, S. R. Sahm, C. R. Alexander, and B. E. Schwartz (2009), The High Resolution Rapid Refresh (HRRR): an hourly updated convection resolving model utilizing radar reflectivity assimilation from the RUC / RR, in *23rd Conference on Weather Analysis and Forecasting/19th Conference on Numerical Weather Prediction*, edited.
- Wright, T. J., Z. Lu, and C. Wicks (2003), Source model for the M w 6.7, 23 October 2002, Nenana Mountain Earthquake (Alaska) from InSAR, *Geophysical Research Letter*, 30(18), 1974.
- Xu, W. B., Z. W. Li, X. L. Ding, and J. J. Zhu (2011), Interpolating atmospheric water vapor delay by incorporating terrain elevation information, *Journal of Geodesy*, 85(9), 555-564.



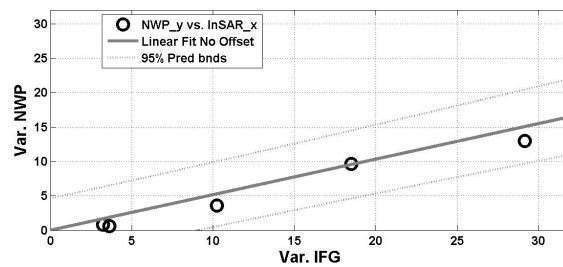
(a) Hawaii case



(b) Mexico Case



(c) Netherland case



(d) Southern Australia case

Figure 2.1 Regression lines per test site; x-axes denotes spatial variance (Var.) of atmospheric signal in Interferogram (IFG.) and y-axes denotes the one in NWP products; from (a) to (d), each plot demonstrates the regression result at the corresponding test site; bold dark gray line denotes the best linear fit; black circles are the data pairs and dashed light gray lines are the 95% prediction bounds for the linear fit

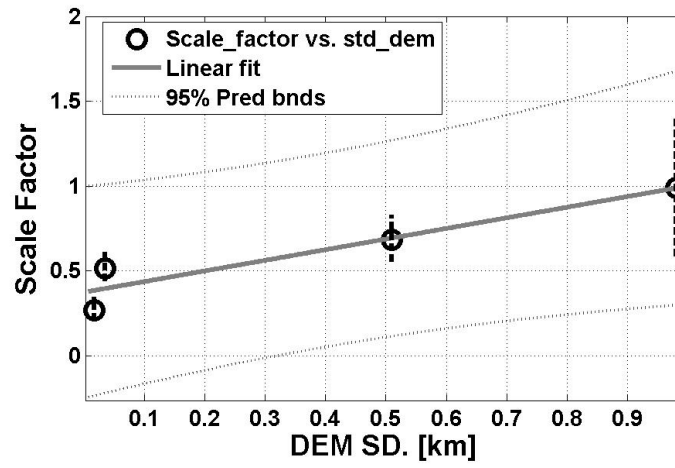


Figure 2.2 Linear relationship between DEM standard deviation (DEM SD.) σ_{DEM} and estimated scale factor \hat{a} in Eq. (2.6). Error bars indicate the uncertainty of the \hat{a} estimates.

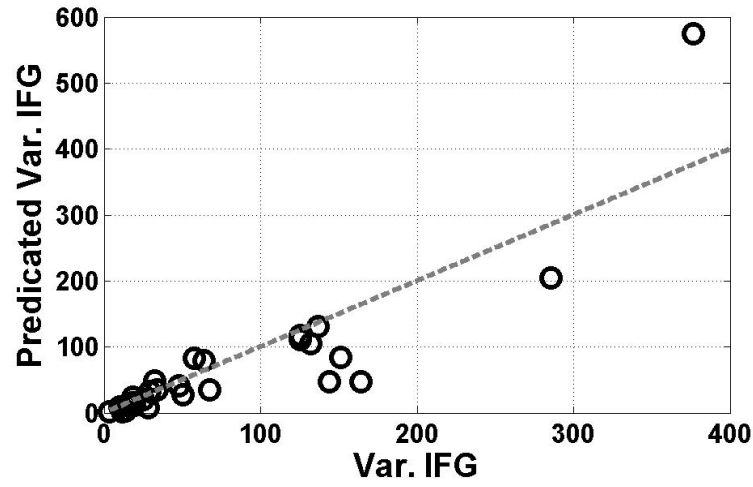


Figure 2.3 Empirical $(\sigma_{i,atm}^2)_{ifg,pred}$ with the scale factor \hat{a} predicated from model in Eq. (2.7) and the external $(\sigma_{i,atm}^2)_{nwp}$ vs. InSAR contained $(\sigma_{i,atm}^2)_{ifg}$. The black markers are data pairs and gray dashed line denotes reference line without bias and offset; x-axis is the true value of the atmospheric spatial variance derived by interferograms (Var. IFG); y-axis is predicted value from NWP products and the empirical function (Eq. (2.7)).

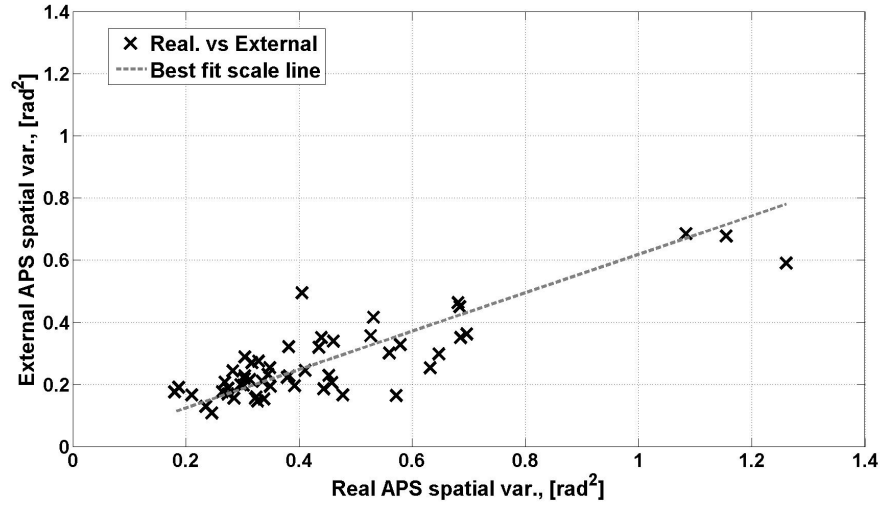


Figure 2.4 Example of synthetic data (black cross markers); $((\sigma_{i,atm}^2)_{ifg})$ (x-axis) and $(\phi_{p,i,s-atm})_{nwp}$ (y-axis); the best linear fit scale line is denoted by black dotted line).

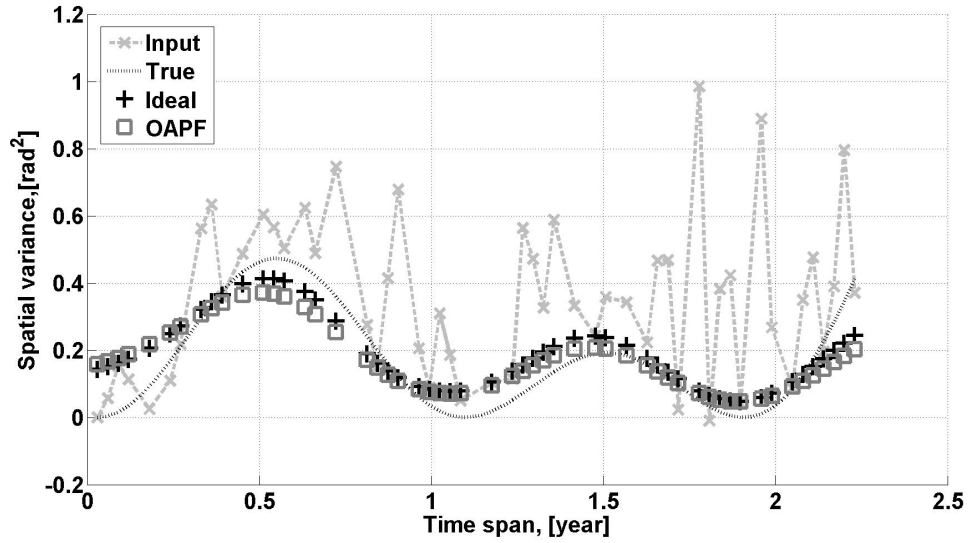


Figure 2.5 Comparison of σ_i^2 , $\sigma_{i,defo}^2$ and its estimates $(\sigma_i^2)_{lp_ideal}$ and $(\sigma_i^2)_{lp_f}$. In the plot's legend, Input denotes the spatial variance to the contaminated interferometric phase; True denotes the spatial variance of the deformation truth; Ideal denotes the spatial variance of the low-passed signal via ideal filter; OAPF denotes the spatial variance of the low-passed signal via the optimal filter.

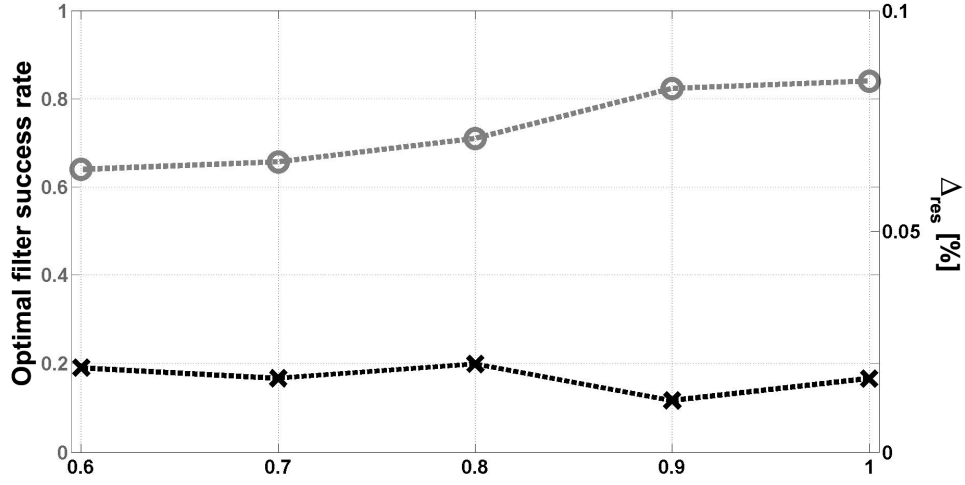


Figure 2.6 Dependence of convergence rate of the optimal phase filter algorithm on the quality of $(\sigma_{i,s-atm}^2)_{nwp}$, quantified by the R^2 (x-axis) between $(\sigma_{i,s-atm}^2)_{nwp}$ and $(\sigma_{i,s-atm}^2)_{ifg}$. The left y-axis values correspond to gray dashed line with circles for the success rate of determining \hat{T} ; the right y-axis relates to the black dashed line and denotes the residuals ratio Δ_{res} in [%].

Table 2.1 Results of linear regression of spatial variance at four test sites including Hawaii, Mexico city (Mexico), the Netherlands (NL) and South Australia (South Aus.). R^2 is the goodness-of-fit parameter; DEM. SD denotes the standard deviation of DEM with each test site.

Site Name	Slope \hat{a}	R^2	Sample No.	DEM SD. [km]
Hawaii	0.99 (0.57, 1.41)	0.67	8	0.98
Mexico	0.68 (0.54, 0.83)	0.83	6	0.51
NL	0.27 (0.19, 0.35)	0.72	9	0.017
South Aus.	0.52 (0.42, 0.61)	0.94	6	0.035

Table 2.2 Results of linear regression of spatial variance using WRF 3.5 and two different model lead times (column 1: 4-11 hours; column 2: 16-28 hours) for test sites Hawaii and Mexico City.

	Previously used lead times		Longer lead time	
	Hawaii	Mexico	Hawaii	Mexico
Slope \hat{a}	0.91 (0.64, 1.17)	0.65 (0.54, 0.76)	0.62 (0.49, 0.74)	0.59 (0.44, 0.74)
R^2	0.82	0.93	0.87	0.67

Chapter 3 Subtle Motion Long Term Monitoring of Unimak Island from 2003 to 2010 by Advanced Time Series SAR Interferometry³

3.1 Abstract

A seven year time series of satellite radar images over Unimak Island, Alaska has been processed using advanced model-free Persistent Scatterer Interferometry (PSI) techniques for a long term geodynamic study. Data processing was assisted by predicted radar signal delay maps derived from numerical weather prediction model to optimally extract the deformation only signals from atmosphere contaminated phase records. The reconstructed deformation time series maps are compared with historical and current Global Positioning System (GPS) measurements as well as Small Baseline Subset (SBAS) InSAR results for quality assessment and geophysical interpretation. Westdahl volcano, Fisher caldera and Shishaldin volcano have been actively erupting or producing ground deformation within recent decades (from the 19 century to present). A Mogi source model estimate for Westdahl volcano suggests a magma source 3.5 km north of Westdahl peak with a depth of chamber center at about 7.0 km beneath sea level through the entire study time span. The magma chamber volume change rate is slowing down compared to previous study results. The deformation field over Fisher caldera is consistent and linear across the full time period analyzed. It has continuous subsiding with a maximum velocity of approx. 16 mm/year in the Line-of-sight (LOS) direction. From the data analyzed here, very little deformation evidence could be found close to the Shishaldin peak. However, a region approx. 15 km east of Shishaldin and the other one at the Tugamak range show evidence of the movement towards the satellite with a temporal correlation with the 2004 Shishaldin eruption. The cause of these movements is unknown.

³ Gong, W., F. J. Meyer, C.W. Lee, Z. Lu, and J. Freymueller, Subtle Motion Long Term Monitoring of Unimak Island from 2003 to 2010 by Advanced Time Series SAR Interferometry, prepared for submission to Journal of Geophysical Research

3.2 Introduction and Motivation

Many volcanic eruptions are preceded by pronounced ground deformation in response to increasing pressure from magma chambers, or to the upward intrusion of magma [Dvorak and Dzurisin, 1997] triggered by deep magma intrusion. This has been considered as one of the main precursor indicators before an eruption begins [Dzurisin, 2003]. Surface deformation measurements can be used to determine the location and shape of a volcanic pressure source beneath the surface [Segall, 2010]. Due to its independence from daylight and weather conditions, predictable repetition cycle, and high spatial resolution, Synthetic Aperture Radar (SAR) Interferometry (InSAR) distinguishes itself as a suitable tool to conduct a long-term deformation monitoring over volcanoes. InSAR measures the uplift or subsidence movement associated with eruptions or magma intrusions as a phase change between repeated acquisitions captured in interferograms. Advanced InSAR techniques can extract these signals with cm-accuracy [Hanssen, 2001]. It is especially suitable for the monitoring of remote regions, for which maintaining in situ geodetic measurements are difficult.

In this paper, we document the observed deformation patterns over Unimak Island, the largest island of the Aleutian Island chain in Alaska [Wood and Kienle, 1990] (see Figure 3.1). It is home to several volcanoes including Roundtop, Isanotski, Shishaldin, Fisher, Westdahl and Pogromni from east to west. Three of these volcanoes (Shishaldin, Fisher and Westdahl) have recorded historical activity, for instance the latest eruption of Shishaldin was in 2004 [Neal *et al.*, 2005] and Westdahl last erupted in 1991 [Lu *et al.*, 2003]. Fisher has been less active than its neighbors since the 19th century, however previous studies observed continuing subsidence around the center of Fisher caldera, which is likely due to hydrothermal activity underneath [Mann and Freymueller, 2003]. Unimak Island is also seismically active. There were more than approx. 890 volcanic-tectonic earthquakes recorded during the period 2003 to 2010 around Westdahl and Shishaldin according to the *Alaska Volcano Observatory* [2009] volcano database. Therefore, Unimak Island is of particular interest to geoscientists.

The remoteness of Unimak Island has limited its geophysical studies, e.g. there were no GPS measurements around the active volcanoes in Unimak Island during 2001 to 2008 and seismic equipment failure led to a seismic data outage during the period of 2006 to 2008 [Buurman, 2013]. Hence, radar interferometric satellite remote sensing techniques were used to retrieve the surface deformation history of Unimak Island for the period of 2003 to 2010.

The value and applicability of InSAR for geodynamic monitoring applications is limited by temporal decorrelation, especially for non-urban areas, due to unstable and complex ground coverage, as well as electromagnetic path delay variations when the radar signal propagates through the atmosphere (ionosphere and neutral atmosphere), both reducing the sensitivity and accuracy of the technique [Hanssen, 2001]. Particularly problematic artifacts in radar images (e.g. C-band and X-band) are caused by seasonal to daily and other changes of weather conditions that can be significant on tall volcanic edifices [Gong *et al.*, 2010]. Also, snow coverage often limits the amount of useful coherent data in sub-arctic environments [Lu and Freymueller, 1998]. Thus, in the present study, an advanced InSAR technique, namely Persistent Scatterer InSAR (PSI), is used for deformation history reconstruction from C-band SAR image time series. The obtained results are further analyzed through volcano source model inversion.

Current advanced InSAR techniques can reduce the severity of aforementioned limitations [Hooper *et al.*, 2012], however their application to regions lacking prior knowledge of deformation has to be carefully handled in order to find the optimal balance between noise reduction and preservation of the deformation signal. Hence, in this study, both atmospheric artifacts and other non-deformation phase artifacts are treated through an advanced method that is combining information provided by a Numerical Weather Prediction (NWP) model [Gong *et al.*, 2011] with deformation model-free PSI techniques [Hooper *et al.*, 2012]. To further support our result, we also applied Small Baseline time series InSAR methods to the same SAR data set for comparison.

The extracted deformation result is validated by comparison to historical (1998-2001) and current GPS measurements within the limited temporal overlap period from 2008-

2010. Afterwards, the PSI-extracted deformation time series are used for volcano source model inversion over Westdahl and for a geophysical interpretation of the rest of the active volcanoes in Unimak Island.

Section 3.3 will briefly introduce the precious geodetic study history of Unimak. The details of the PSI method as well as the extracted time series are presented in Section 3.4, which also provides information about the input data set, including SAR imagery and auxiliary atmospheric delay maps from meteorological numerical simulations. In the same section, a brief introduction on the SBAS technique is presented and its results are compared to the PSI derived deformation measurements. In Section 3.5, for the three active volcanoes (Westdahl, Fisher and Shishaldin), PSI outputs are firstly compared with historical (1998 to 2001) and current (after 2008) GPS measurements and then used for the volcanic geophysical interpretation; the results over Westdahl Volcano are further used for volcanic source model inversion. A general discussion of the deformation on Unimak Island is summarized and finalized in the last section.

3.3 Unimak Island and Its Previous Geodetic Studies

Surface deformation on Westdahl Volcano was studied in previous efforts both from radar satellite remote sensing and GPS studies. InSAR techniques have been applied to study the post-eruption inflation from 1993 to 1998 [Lu *et al.*, 2000] and 1991 to 2000 [Lu *et al.*, 2003] after its eruption in 1991. These studies suggested Westdahl Volcano was inflating in an exponentially decaying fashion. Mann and Freymueller [2003] used GPS measurements acquired from 1998 to 2001 to analyze Westdahl's surface motion and characterized its magma chamber properties. The GPS determined volcanic source depth of Westdahl [Mann and Freymueller, 2003] is deeper than that of the InSAR result, nevertheless it suggested the volume change was slowing down compared to InSAR results from 1993 to 1998 [Lu *et al.*, 2000]. Both previous studies showed that the rate of magma supply to the pressure source has been gradually slowing down but was still ongoing as of 2001. There is a slight inconsistency in the horizontal location of the source chamber, with the GPS study finding a location slightly north of the InSAR study.

However, both studies suggested that a point source model [Mogi, 1958] was sufficient for modeling the deformation at Westdahl volcano.

Fisher caldera, which contains several active fumaroles and two large lakes, is one of the largest calderas in the Aleutian Islands [Lu, 2007] and is located east of Westdahl. The southern part of Fisher is covered by a thick layer of tephra, which offers the potential of achieving excellent coherence in our radar interferometric studies. Previous studies showed subsidence of up to 3cm during the period of 1993 to 1995 [Lu, 2007] measured with InSAR techniques and 1998 to 2001 from GPS measurements [Mann and Freymueller, 2003] (square markers in Figure 3.1), which may be due to the contraction of the magma body underneath and the depressurization of the corresponding hydrothermal system.

In the center of Unimak Island, Shishaldin Volcano, a stratovolcano that is the highest peak of the island, has 28 recorded eruptions during recorded history. The last four eruptions were in 1995, 1997, 1999 and 2004 [Alaska Volcano Observatory, 2009]. However, previous satellite InSAR studies observed no significant deformation in the coherent region for the two eruptions in the 1990s [Moran *et al.*, 2006], which suggests rapid magma re-filling and transportation that compensated for the pre-eruption inflation, and a very shallow depth magma chamber [Lu, 2007; Moran *et al.*, 2006].

3.4 Techniques, Background and Data Processing

In this study, special attention has been paid to separate the deformation field from non-deformation artifacts in the InSAR data processing of this study. Strong atmospheric artifacts have been observed in this region that can mimic volcano inflation. For example, atmospheric delays contaminated the deformation map and interfere with geophysical interpretation and inversion around Shishaldin Volcano [Gong *et al.*, 2010].

The PSI technique can largely overcome the problem of ground decorrelation in areas of natural ground cover over a long time interval. We apply a deformation model free PSI method given its reliable performance for applications in the natural environment [Hooper *et al.*, 2012]. The processing parameter optimizations in PSI data processing,

especially the optimal temporal filter determination, need to be carefully carried out to ensure that most accurate results are generated to preserve the subtle deformation field [Gong and Meyer, 2012]. Thus, the NWP produced atmospheric delay map statistics at the image acquisition time are used to assist PSI processing (Chapter 2).

In this study, 23 scenes of Environmental satellite (ENVISAT) Advanced Synthetic Aperture Radar (ASAR) data acquired in descending mode during the period of July, 2003 to August, 2010 are used for deformation history reconstruction. Specifically, only the snow-free season scenes, mainly acquired from May to October, are used in the experiment due to their favorable seasonal ground coverage condition that improves the interferometric coherence. The image acquired on September 22, 2006 was discarded from the PSI processing due to its large spatial baseline.

3.4.1 Advanced Time Series InSAR Processing Strategy

3.4.1.1 Phase Components Decomposition

The unwrapped differential interferometric phase components at pixel p in interferogram i can be written as Eq. (3.1) [Ferretti *et al.*, 2000; Hooper *et al.*, 2012].

$$\phi_{p,i} = \phi_{p,i,topo} + \phi_{p,i,defo} + \phi_{p,i,orbit} + \phi_{p,i,atm} + \phi_{p,i,noise} \quad (3.1)$$

where $\phi_{p,i,topo}$ is the residual due to the inaccuracy of the terrain model used in the differential interferogram formation, $\phi_{p,i,defo}$ is the contribution of ground deformation, $\phi_{p,i,orbit}$ denotes the residual error from the satellite orbits, $\phi_{p,i,atm}$ is the atmospheric distortion that consists of a slave component $\phi_{p,i,s-atm}$ and a master component $\phi_{p,i,m-atm}$, and the last term $\phi_{p,i,noise}$ is the phase noise component (e.g. system thermal noise and decorrelation noise) that is presumed to be relatively small for a phase stable pixel in PSI studies.

Phase components $\phi_{p,i,topo}$ and $\phi_{p,i,m-atm}$ are removed following the standard model free PSI processing [Hooper *et al.*, 2007; Kampes, 2006]. As the main purpose of this study is for volcanic motion monitoring, $\phi_{p,i,orbit}$ is modeled by a long wavelength plane

ramp and subtracted from $\phi_{p,i}$. After removing those components (referring as pre-processing in this paper), the remaining phase signal ($\tilde{\phi}_{p,i}$) contains $\phi_{p,i,s-atm}$, $\phi_{p,i,defo}$, and the nuisance term $\varepsilon_{p,i}$ as shown in Eq. (3.2). $\varepsilon_{p,i}$ contains residuals of the largely eliminated signals of $\phi_{p,i,topo}$, $\phi_{p,i,m-atm}$, and $\phi_{p,i,orbit}$.

$$\tilde{\phi}_{p,i} = \phi_{p,i,defo} + \phi_{p,i,s-atm} + \phi_{p,i,noise} + \varepsilon_{p,i} \quad (3.2)$$

Afterwards, $\phi_{p,i,defo}$ is separated by applying an atmospheric filter optimization with the assistance of NWP produced atmospheric delay maps [Gong and Meyer, 2012] (see Chapter 2).

21 single master interferograms were formed and processed for deformation monitoring and 89,778 phase stable pixels were found through PSI processing. The corresponding image acquisition time, baseline information and spatial variances of differential atmospheric delays computed from NWP products (var_{aps}) are listed in Table 3.1. The data set shows strong atmospheric distortions (e.g. August 13, 2004 and October 17, 2005) and large time gaps ranging from 245 to 420 days over winter that leads to a small data stack over a large time span with severe atmospheric artifacts.

3.4.1.2 Advanced Atmospheric Signal Mitigation

The Weather Research and Forecast (WRF) model [Skamarock *et al.*, 2008] (version 3.5) was used to model the atmosphere in three dimensions (3D). Initial boundary conditions from National Center for Environmental Prediction (NCEP) Final (FNL) data [UCAR, 2013] were used as input for the WRF runs. We use an approximately 9 hour forecasting period and 1km horizontal resolution setup for model outputs. The refractivity index is computed at each resolution grid cell and integrated in the satellite Line of Sight (LOS) direction to produce integrated absolute atmospheric delay maps. Afterwards, the simulated atmospheric phase screens (APSs) are computed through differential delay maps corresponding to the SAR image acquisition times, and the temporal mean is subtracted from every simulated APS to approximate the master component subtraction;

a linear planar trend also is removed from the simulated APSs. In the end, the NWP simulated APSs are resampled to the 300m resolution grid in radar coordinates then finally used to compute $\sigma_{i,nwp}^2$ that assists the extraction of $\phi_{p,i,defo}$ from $\tilde{\phi}_{p,i}$.

After pre-processing, the conventional PSI separates $\phi_{p,i,defo}$ from $\tilde{\phi}_{p,i}$ (Eq. (3.2)) through a spatial-temporal low-pass filter based on the expectation that atmospheric signals are temporally decorrelated and spatially correlated over a small scale, while deformation signals are correlated both in time and space [Hanssen, 2001]. In order to implement the temporal filter optimization as described in previous studies [Gong and Meyer, 2012], the pre-processed PSI phases are resampled to the 300m resolution grid in radar coordinates so that the multi-looked phase $\tilde{\phi}'_{p,i}$ has the same resolution as the NWP produced delay maps and has minimum $\phi_{p,i,noise}$ contribution. The mathematical representation of temporal low pass filtering is written in Eq. (3.3), in which t is the temporal baseline for each interferogram and $g(t, T)$ is a low pass temporal filter with length T . The low pass signal $(\tilde{\phi}'_{p,i})_{lp}$ is the estimate of the deformation component.

$$(\tilde{\phi}'_{p,i}(t))_{lp} = \sum_{\tau=0}^t \tilde{\phi}'_{p,i}(\tau) \cdot g(t - \tau, T) \quad (3.3)$$

The optimal low pass filter length \hat{T} is chosen to maximize the linear correlation between $\sigma_{i,nwp}^2$ and the spatial variance ($\sigma_{i,hp}^2$) computed from high passed signal $(\tilde{\phi}'_{p,i})_{hp}$, where $(\tilde{\phi}'_{p,i})_{hp} = \tilde{\phi}'_{p,i} - (\tilde{\phi}'_{p,i})_{lp}$. After applying an iteration approach, the optimal low pass filter length \hat{T} (175 days) is determined through the same algorithms as described by Gong *et al.* [manuscript in preparation]. Afterwards, the optimal temporal filter length \hat{T} is applied to control the standard model free PSI processing [Hooper *et al.*, 2012]. Finally, the estimated deformation time series is shown in Figure 3.2, which shows subtle but continuous areas of deformation across Unimak. The detailed evaluation and geophysical interpretation of the results will be presented in Section 3.5.

3.4.2 Small Baseline Time Series InSAR

As mentioned before, within the study time span there are few other geodetic observations for validation, thus we also applied the Small Baseline Subset (SBAS) InSAR technique to the same data set for PSI deformation maps validation. In this case, the SBAS result is used as a reference only, as comparison of the techniques for the deformation detection and long term monitoring is beyond our scope. A technique comparison can be found in previous literature [*Shanker et al.*, 2011]. The SBAS method first divides the unwrapped interferograms into two stacks, including a low quality and a high quality subset. The latter are used for correcting the phase unwrapping errors in the low quality interferograms then both used together for displacement estimation. The implementation steps include the small baseline interferogram generation and selection, phase unwrapping, phase inversion through singular value decomposition (SVD) and mitigation of non-deformation signals through mathematical modeling and iteration processing (for detail please refer to [*Lee et al.*, 2010]). In the processing, 42 small baseline interferograms were generated, within which 21 interferograms were selected as the high quality subset and one frame was discarded due to its un-favorable coherence conditions. In the end, the displacements at the 21 single-look-complex images (SLCs) acquisition time (all referring the earliest acquisition) were processed and recovered. In Figure 3.3, the recovered linear deformation velocity maps in geographic coordinates from PSI and SBAS are plotted in the similar grid size for visual comparison. Figure 3.3a only has the phase stable pixels plotted, while Figure 3.3b is an un-masked map that includes most of the low quality points plotted as well.

In Figure 3.3, both methods detected common deformation features with similar deformation velocity as denoted by the color counter: a subtle movement towards satellite around Westdahl and a stronger subsidence region over Fisher caldera. The snow and ice cover in the high elevations (e.g. the tops of Shishaldin and Westdahl) and vegetation at lower elevation (e.g. the northwest region of Unimak Island) [*Alaska Volcano Observatory*, 2009] hamper the PSI from targets extraction. Those regions behave as low confidence pixels in the SBAS derived deformation velocity map. Overall, the PSI

reconstructed the average velocity map shows similar quality to the one from SBAS method at coherent pixels.

Figure 3.4 shows an example of point wise comparison for Fisher caldera that compares the extracted maximum subsidence captured by the PSI and SBAS methods. A coherent target in SBAS method has been selected randomly in the center of Fisher caldera and the surrounding region, an area of approx. 200 m radius was searched for PSI points and 5 targets are found within the searching area. The averaged time series of the SBAS (gray dashed line with square marker) and PSI points (black dashed line with circle marker) are plotted in Figure 3.4. All the time series are relative to the image acquired on September 7, 2007 and are spatially referenced to the spatial average of overall displacement computed from each measurement separately. The time series agree well with each other with a correlation coefficient of approx. 0.99 and only larger residual between each other at the beginning of the time series.

3.5 Geophysical Study Based on InSAR Result

Based on the deformation time series maps in Figure 3.3 and velocity fields in Figure 3.6, we can identify subtle movements towards the satellite around Westdahl and observe subsidence type signals over Fisher caldera. Moreover, it is notable that the area of the Tugamak Range as well as the east side of Shishaldin also show a very subtle deformation (Figure 3.3) while the rest of the island is relatively less active in producing ground deformation. In this section, the PSI results are further compared to historical and current GPS measurements, and are used jointly with them for a geophysical interpretation. Focusing on Westdahl volcano, a point source model inversion is applied and presented in Section 3.6.

3.5.1 Comparison with In Situ Geodetic Measurement

There are two sets of GPS velocity measurements available over Unimak, including the historical GPS data covering the time from 1998 to 2001 and current GPS measurement covering the time from 2008 to present. The two data sets involve different sites and there were no measurements between 2001 and 2008. It is possible that the rate

of deformation was different during the two time periods. The PSI results are compared to both of them to better understand the overall deformation history.

3.5.1.1 Comparison with GPS Measurement Before 2001

There were 7 GPS campaign sites around Westdahl and 5 around Fisher Caldera during the period from 1998 to 2001, plotted in Figure 3.1 as square markers [*Mann and Freymueller, 2003*]. The GPS measurements were computed in the International Terrestrial Reference Frame 1997 and velocities were referenced to the site KATY at the east end of the island [*Freymueller and Beavan, 1999*]. The details of the comparison between the GPS and PSI measured LOS motion velocities are shown in Table 3.2 together with the GPS sites' location, the number of selected PSI points nearby and the average distance from the PSI points to each GPS station. The distance thresholds are determined adaptively with 50 m per step to guarantee at least two PSI points are chosen. The PSI results from 2003 to 2010 are adjusted so that the mean LOS displacement over each image is zero (Table 3.2). Note, that the SAR image has no sensitivity to the ground motion parallel to the satellite track (azimuth direction) because it records only the motion in the LOS direction, perpendicular to the descending satellite track (shown in Figure 3.1). Hence, the 3D velocity of GPS records as well as its uncertainty (see Table 3.2) given by *Mann and Freymueller* [2003] was projected into the SAR LOS direction for comparison with PSI measurements.

The uncertainties of the PSI results are the standard deviation of the velocities at the PSI points within the given distances. Two GPS sites (WESS, PANK) are not included in Table 3.2 because there were not sufficient PSI points in nearby areas, or the site was outside of the image spatial coverage. GPS sites named with the prefix 'WE' as well as site SCAP surround Westdahl peak and the prefix 'FC' denotes the sites around Fisher Caldera.

First of all, the bias introduced by the different reference frames of the PSI and GPS velocities needs to be removed. However, due to the fact that the majority of PSI points are close to active volcanoes and there is no SAR image coverage over the GPS reference point KATY at the east end of the island, we applied an alternative method to determine

the reference difference between the GPS and PSI velocities. We computed the difference between the velocities of GPS site FC02 and its surrounding PSI points and assume this difference is only from the spatial reference difference. This method is implemented based on the following considerations: (a) the GPS result for FC02 has very high quality and the smallest average distance to the surrounding PSI points; (b) this area has a high PSI point density in the original SAR images and a high deformation-to-noise ratio; and (c) as suggested in previous studies [*Mann and Freymueller, 2003*], Fisher caldera is subsiding linearly. As shown in the PSI and SBAS comparison in Figure 3.4, the deformation rates over Fisher caldera from both studies are linear in time. Thus, if there is any difference caused by the reference frame difference between PSI and GPS results, it should be linear in time. Therefore, the velocity offset of about 0.1 mm/year (PSI minus GPS) caused by the reference frame difference is calculated and the corrected PSI velocities are listed in the sixth column of Table 3.2. Such a small correction is not a surprise, because the GPS study [*Mann and Freymueller, 2003*] suggested that most of the island did not move relative to KATY.

Comparing the corrected PSI velocities after 2003 and GPS measurements from 1998-2001 (Table 3.2 column 6), the inflation rate of Westdahl volcano is decreasing. Most of the region is still moving towards the satellite (the LOS direction), with a velocity less than one centimeter per year. The subsidence rate of Fisher caldera is faster and more consistent compared to Westdahl region. Around Fisher caldera, the difference between the PSI velocities and the historical GPS measurement is less than 2 mm/ year except for FC05. This difference is well within the error bound of the GPS results.

3.5.1.2 Comparison with GPS Measurement After 2008

Since 2008, the Plate Boundary Observatory (PBO) includes a continuous GPS network [*UNAVCO, 2013*] on Unimak Island that mainly covers Westdahl and Shishaldin volcanoes. Site locations are plotted in Figure 3.1 and the corresponding geographic information is listed in Table 3.3. There are 13 sites available with three years (2008 - 2010) of overlap with the PSI study time period. This section compares the time series computed from PSI and GPS. The time series are compared in Figure 3.6 for Westdahl

and Figure 3.7 for Shishaldin. The number of PSI points near each GPS site is listed in Table 3.3, including their average distance from the GPS site.

In Figure 3.6 and Figure 3.7, the time series of GPS daily measurements projected into the LOS direction are given by dashed gray lines and the 10 day average is represented by bold black lines; the time averaged GPS measurements with corresponding error bounds at the SAR acquisition dates are highlighted by blue lines with cross markers and the time series inverted from PSI techniques are denoted by red lines with circle markers. The GPS error bounds in the LOS direction are computed from the uncertainties of the GPS 3D positions and the PSI error bound is the standard deviation of the PSI points surrounding the GPS instrument locations. Due to impacts of snow accumulation on the GPS antenna [Freymueller, Personal Communication], GPS records during the winter period (December to next year May) for AV27, AV29 AV35, AV37 and AV39 are removed from figures and analysis. Given that all the SAR acquisitions are during the local Alaska summer period, this only affects AV37 and AV39 by reducing one or two GPS records from the overlapping sample set.

All the time series are referenced to the earliest date of the temporal overlap between the PSI and GPS. The PSI time series are referenced so that the spatial average displacement in the every interferogram frame is zero, while the PBO GPS measurements are relative to a North America fixed reference frame based in ITRF2008 (NAM08). To put the PSI and GPS in the same reference frame, the linear rates of the GPS and PSI from 2008 to 2010 are computed separately from their measurements at the common time interval. The rate differences (GPS rate minus PSI) are shown in Figure 3.5 by square markers and the posterior error bound is denoted by black vertical bars. Site AV40 is excluded from this comparison due to large residuals in the PSI processing, and will be discussed later in this section. The remaining 12 sites are used to compute the weighted average velocity shift between the GPS and PSI (0.98 mm/year) shown in Figure 3.5 denoted by the dashed gray line. This average rate difference is taken as the spatial reference frame difference between the GPS and PSI, and is removed from PSI displacement time series. The PSI results given in Figure 3.6, Figure 3.7 and Table 3.3

are measurements after the spatial reference compensation. This reference frame difference determination method is applied due to the difficulty in defining a proper reference area in the PSI measurements given that most of PSI points are near active volcanoes and is based on the following assumptions: (1) The reference frame difference is assumed to be linear in time; and (2) all linear rate differences between the GPS and PSI are due to the different reference frame or random noise.

In Figure 3.6, the PSI and GPS measurements are plotted together for interpretation. The time series are given as one-way displacement, with motion toward the satellite (satellite direction is shown in Figure 3.1) being positive. Around Westdahl Volcano, the station AC10 hardly shows any linear trend during the overall time span (Figure 3.6). For instance, the AC10 time series in Figure 3.6b indicates a slight movement away from the satellite before 2009, which is also confirmed in the SBAS derived deformation rate map in Figure 3.3b. The AC10 GPS time series shows that the site moves towards the west and slightly to the south. The negative trend in the LOS velocity is caused by the site moving away from the satellite. Both the sites AV24 and AV25 demonstrate an overall linear trend with total motion toward the satellite of approximately 20 mm from 2003 to 2010. For sites AV26 AV27 and AV29, the continuous deformation with total motion toward the satellite is more obvious, about 30 to 50 mm over 7 years. For site AV26, the InSAR measurements accumulating from 2009 to 2010 show a lower slope than GPS. These motions are upward and away from the volcano, so both the GPS and PSI confirm the inflation of Westdahl since 2003.

The comparison of sites around Shishaldin is shown in Figure 3.7, where an interesting phenomenon is captured by the PSI measurements. First of all, the time series of sites AV34, AV35, AV38 demonstrates a negative trend before the middle of the year 2004 followed by a positive trend after that. This matches the time of the 2004 Shishaldin eruption from Feb 17 to May 14 [*Alaska Volcano Observatory*, 2009]. However, these sites are located more than 15 to 30 km away from Shishaldin. The sites on Shishaldin volcano, AV36, AV37 AV39 and AV40 show no change in motion at that time. The first three sites would be expected to record a stronger volcanic motion from a volcanic source

underneath Shishaldin if that caused the deformation at AV34, AV35 and AV38. Thus the cause of these motions is not clear. The motion signals at AV37 and AV39 are rather similar, while the PSI measurements at AV39 are relatively noisier. Neither the GPS nor PSI provides any indication of a co-eruption signal. An earlier study showed that Shishaldin volcano did not have significant co-eruptive ground motions during both its 1995-1996 and 1999 eruptions [Moran *et al.*, 2006]. This study covered the areas around the sites AV36, AV37 and AV39. Thus, the behavior we see in our study confirms that within the same area there is no obvious volcanic motion. Site AV40 is close to the coast south of Shishaldin. As shown in Figure 3.3a, the point density over this region is very low and far away from the other PSI points, which might introduce phase unwrapping errors in the reconstructed deformation time series around AV40 as shown in Figure 3.7g. The observations after 2007 seem to be stable, however.

3.5.2 Comparison with Different PSI Parameter Setting

We also compare the GPS measurements with PSI time series computed using different temporal filter settings. The same procedure for reference frame difference compensation was applied to the results from the 70 days setting. The statistics, residual offset and standard deviation (sd.) at every GPS site, computed from the GPS and PSI time series over the common time interval are listed in the last two pairs of columns of Table 3.3. From the residual offset, it's notable that there is more underestimation for site AV26 both for 70 days and optimal window setting.

As listed in the last column of Table 3.3, the optimized window provides smaller residual standard deviations at 10 out of 13 GPS sites with an average improvement of less than 1 mm per site. This suggests that the window length has only a small effect on the results at the GPS site locations. Outside the GPS temporal coverage, an example of a 70 days window setting result is shown in Figure 3.7h, which introduced two different linear trends in 2004 and 2005 that might be artificial features introduced from the failure in atmospheric anomaly reduction. This indicates the optimal filter is able to balance the noise-reduction and the motion recovery, while there is only very small improvement in this study.

3.6 Source Model Inversion of Westdahl Volcano

In this section, we apply a volcano source model inversion to the PSI-derived motion time series maps of Westdahl Volcano. According to the study of *Mann and Freymueller* [2003], there is no significant strain accumulation due to the locked subduction zone across the entire island, so the contribution from non-volcanic sources over the Westdahl region is assumed to be small. Hence, without compensating deformation from any other source, the one-way displacement time series derived from PSI are used as input for estimation of a volcano source model.

Previous studies [*Mann and Freymueller*, 2003; *Lu et al.*, 2003; *Lu et al.*, 2000] suggested that a Mogi source [*Mogi*, 1958] is sufficient for describing the volcanic deformation at Westdahl volcano. The Mogi model treats the magma chamber as a spherical point source with the assumption of an elastic homogeneous half-space. The point source approximation is valid if the chamber radius $a \ll$ source depth d . The volume change ΔV of the source leads to horizontal displacement and ground elevation change $d(e, n, u)$ at the free surface. A rectangular region around Westdahl volcano was selected for the inversion and the PSI results were multi-looked by a factor of 4 in range and 20 in azimuth to further reduce noise. We define a three dimensional local Cartesian coordinate system with axes pointing east-north-up and the upper left of the cropped region as the origin (shown in Figure 3.8). Given a chamber location of x_o (x_{eo}, x_{no}, x_{uo}), the predicted displacement $d(e, n, u)$ at point x ($x_e, x_n, x_u = 0$) due to the volume change ΔV can be written as Eq. (3.4) [*Dzurisin*, 2007].

$$\begin{pmatrix} e \\ n \\ u \end{pmatrix} = \beta \cdot \Delta V \cdot \frac{1}{R^3} \cdot \begin{pmatrix} x_e - x_{eo} \\ x_n - x_{no} \\ -x_{uo} \end{pmatrix} \quad (3.4)$$

in which R is the radial distance between the surface point x to the chamber center and β is the source physical constant that is a function of Poisson's ratio ν of the half-space and can be simply written as $(1-\nu)/\pi$. The suggested value of $\nu = 1/4$ is used in our study [*Dzurisin*, 2007; *Mctigue*, 1987]. On the right side of Eq. (3.4), it is noticeable that the

horizontal displacement is scaled by the distance between the source and surface point, while the vertical displacement is scaled by the source depth. Based on the original definition of the Mogi model, the topography of our study area is not considered in the inversion.

The inversion was realized through the MATLAB nonlinear least squares optimization toolbox routine 'lsqnonlin'. There are seven unknown parameters for the model, the four source model parameters (x_{eo} , x_{no} , x_{uo} , ΔV) and three phase ramp parameters (North-South slope, East-West slope, and static-residual). The static parameter also accounts for any difference between the model velocity reference and the PSI stack velocity reference. The original PSI displacement time series are used for the inversion, which have the average displacement field being zero within the cropped imagery. The average displacement of the model is subtracted from the model predictions during the inversion process, minimizing the difference between PSI measurements and Mogi model numerical simulations. Moreover, the displacement time series derived from PSI processing should already minimize non-deformation artifacts. For instance the orbit residual, which behaves as a large scale ramp signal throughout the image, should be relatively small.

The bounds used for the constant parameter of the ramp can have a significant impact on the inversion. This parameter reflects the average difference between the reference frame of the data and model, plus the impact of any non-volcanic motions. Two sets of inversions are applied to PSI displacement time series: the first one is to determine the horizontal location of the Mogi model and the second one is to optimize the remaining volcano source parameters. The source model parameters are given relaxed bounds that extend beyond the detected source centers in previous studies [Lu *et al.*, 2003; Mann and Freymueller, 2003], e.g. the initial bounds of depth are from 3 to 12 km and the corresponding ramp parameter setting will be discussed below. This procedure is required because of the difficulties of InSAR measurements in estimating all seven parameters in the inversion, which are: (1) the area close to Westdahl peak has no data due to loss of coherence (as shown in Figure 3.2); (2) InSAR measurements only provide displacements

in the LOS direction; and (3) there is only subtle deformation (less than 10 mm/year) observed around Westdahl.

The first inversion is applied to the seven-year average displacement rate. The average rate is least affected by noise in the time and therefore provides the most accurate estimates of average source location. It has minimized the temporal uncorrelated residual left from PSI processing. The slope ramp parameters are fixed to zero in this case and the static-residual is given large bounds from -50 to 50 *mm*.

The horizontal location of the best fitting Mogi source is at $164.65\text{W} \pm 0.04\text{km}$ $54.55\text{N} \pm 0.05\text{km}$ (red circle in Figure 3.8), less than 3.5 km north of Westdahl peak (black cross sign), or the InSAR suggested volcano source location from the period 1991 to 2000 [Lu *et al.*, 2003]. Our estimate is within 125m southwest of the location determined in the previous GPS study for the period 1998 to 2001 by Mann and Freymueller [2003] (black plus sign in Figure 3.8).

The depth and ΔV estimates show the volcano source is located 7.0 ± 0.18 km underneath seal level with $4.3 \pm 0.1 \times 10^6$ m³/yr of volume change. This result is approx. 200 meters above the previous GPS study at $7.2^{+2.3}_{-1.2}$ km [Mann and Freymueller, 2003] and the annual ΔV from our study is about two thirds of the GPS result at $6.7^{+3.3}_{-1.8} \times 10^6$ m³/yr. The difference in source depth is not significant at the 95% confidence level, thus the source location at Westdahl appears to vary. However, the difference in ΔV is significant.

For the second inversion, we keep the horizontal source location fixed and invert the time series of displacements. As shown in Figure 3.2, the differences between the computed cumulative displacements at different months within the same year are very small. Hence, we have averaged the displacement results for every study year and applied an inversion for source parameters to the yearly averages. The yearly increment inflation signal isn't used for the inversion study due to the subtle deformation signal as well as the low signal-to-noise ratio (SNR). Instead the cumulative displacement time series relative to the first acquisition year (2003) is used as inputs of the second set of inversion.

The first attempt of the inversion for time series had only horizontal location fixed. The static residual bound is set to the same as in the first inversion. We relax the bounds on the slope parameters within a small bin -0.5 to 0.5 *mm/km* to adjust the larger non-volcanic signals in the yearly averages. This is needed because (1) fixing the source location will reduce the flexibility of inversion; and (2) the SNR of the yearly averages is not as good as that of the full time span temporal average in the first inversion.

The estimates of ΔV , source depth and static residuals from the first attempt of the second inversion are listed in Table 3.4, where the average value of the static-residual and slope trend in the center of the cropped image are provided. There are variations of the estimated source depth, particularly in the first three years (2004 to 2006), which is also correlated to the center point residual (Table 3.4). This hampers the inversion from estimating the other volcano source parameters.

Hence, by assuming the vertical location of volcano source also remains stable through the study time span, we use the source depth from the first inversion and only attempt to compute the ΔV and the three ramp parameters from the yearly cumulative displacement time series. Results are shown in Table 3.5. Comparing to the standard deviation of ΔV estimates listed in Table 3.4, there is a clear reduction (Table 3.5) for the inversion with fixed source depth. The value of the static residual at central point is in a range of 0 to 5 mm (Table 3.5), which is not surprising given predicted deformation signals and InSAR measurements have the same spatial reference. The estimates on the two slope ramp parameters are within the initial search bounds setting for all cases but the one in 2008.

The inverted cumulative ΔV is modeled as a function of time. *Lu, et.al* [2003] proposed that ΔV is an exponential decaying function of time. With all the cumulative ΔV estimates referenced to the first SAR acquisition time on July 25, 2003, their model can be written as Eq. (3.5).

$$\Delta V_j = \left(1 - e^{-k \cdot t_j}\right) \cdot Q_0 \cdot k / \beta \quad (3.5)$$

where t is the time interval between July 25, 2003 and the rest of acquisitions, β is the constant defined in Eq. (3.4), Q_0 is the initial magma flux into the reservoir and k is a physical parameter that describes the frictional loss factor, magma viscosity, steady state change in magma reservoir volume, and length as well as the radius of the conduit ($1/k$ is the so called time-constant) [Dvorak and Okamura, 1987; Lu *et al.*, 2003]. Similar to previous studies, k is treated as a single parameter and estimated with Q_0 by searching through the parameter space of k . The best fitting solution for Eq. (3.5) is found at $k = 0.20$ and $Q_0 = 33.8 (\times 10^6 \text{ m}^3/\text{yr})$, which has an R^2 of 0.96, indicating an excellent fit to Eq. (3.5). The modeled cumulative ΔV is plotted in Figure 3.9a with a black dashed line and the cumulative ΔV time series estimated from Mogi source inversion are denoted by gray dots with corresponding error bounds denoted by gray bars. A linear regression through the origin is also applied to the same data set, which provides the estimate of the weighted linear rate of volume change in time of $3.5 \pm 0.5 \times 10^6 \text{ m}^3/\text{yr}$ with R^2 of 0.83.

Thus, the cumulative ΔV time series is better explained by the exponential model than the linear model. For better comparison to the previous study, we also take the same reference date as proposed by Lu *et al.* [2003], and use their model estimates ($k = 0.17$ and $9.2 (\times 10^6 \text{ m}^3/\text{yr})$) into our measurements. However, the R^2 indicates a poor fit. A hypothesis can be made here that a single exponential decaying function is sufficient to explain the volume change of Westdahl over the full time span since the 1991 eruption.

Moreover, from both Table 3.5 and Figure 3.9a, it is noticeable that there might be three stages of volume change with two obvious breaks in 2006 and 2009, where the refilling of the magma source nearly stopped before restarting in the year after. This episodic pulse hypothesis resembles what was at Okmok volcano, where three distinct inflation episodic pulses could be identified observed [Fournier *et al.*, 2009]. A speculation can be made here that the volcanic inflation at Westdahl is pulsed, rather than decaying steadily. We applied the model with three separate linear functions through the origin to the same data set to model the linear rates in these different stages, the result is plotted in Figure 3.9b, from the left to the right the computed values of ΔV rate are $5.6 \times$

$10^6 \text{ m}^3/\text{yr}$, $3.8 \times 10^6 \text{ m}^3/\text{yr}$ and $3.2 \times 10^6 \text{ m}^3/\text{yr}$. By taking into account the previous volume change rate estimate from previous studies, e.g. the GPS result of $6.7^{+3.3}_{-1.8} \times 10^6 \text{ m}^3/\text{yr}$ from 1998 to 2001 [Mann and Freymueller, 2003], this again implies that the rate of volume change is decreasing with time and explains the good fit to the exponential decaying model.

3.7 Geophysical Discussion

Based on the deformation time series maps extracted and analyzed above, the deformation observations from 2003 to 2010 over the three active volcanoes in Unimak can be summarized as follows:

Although Westdahl Volcano is still inflating, its average LOS velocity over coherent areas is now less than 1 cm/yr . This is much smaller than the approximate rate of 2 cm/yr from 1998 to 2001 [Mann and Freymueller, 2003]. The point source model inversion indicates a magma source 3.5 km northeast of Westdahl peak with an inflation source center at approx. 7.0 km below sea level. The location agrees well with the previous GPS studies from 1998 to 2001 [Mann and Freymueller, 2003]. The volume change time series shows a clear slowing of inflation at Westdahl since 1998. Our result supports the model proposed by Lu *et al.* [2003] that the magma refilling rate of Westdahl can be modeled by an exponentially decaying function. However, a single exponential function does not fit all the data from the 1990s to 2010. Our results also suggest that the slowing of volume change rate with time of Westdahl is characterized by two noticeable pauses at 2006 and 2009 where only little magma was added into the volcano system. While consistent with the GPS results, the source model location estimated in this study differs from previous InSAR results published in [Lu *et al.*, 2003]. This difference also impacts the temporal model of volcanic change. It is necessary to study other geological or geophysical data to confirm and understand if this discrepancy is caused by a shift of the volcano source from underneath Westdahl peak to approx. 3.5 km north of it, or if the difference between the estimates can be explained by other reasons. Also, one should also

re-examine the historical SAR data [Lu *et al.*, 2003] and SAR acquisitions used in this study to jointly estimate the change of volcano source parameters in time.

The step-linear rate model fit the volume change estimates very well. Together with the previous study on the volume change [Lu *et al.*, 2003], we can consider a scenario of magma refilling between any two eruptions of Westdahl (Figure 3.10): after an eruption stops, the volcano source begins to refill in pulses, producing several longer term exponentially decaying processes.

The motion field over Fisher caldera is more consistent and linear with time, and subsidence has continued with a maximum LOS velocity of approx. 16 mm/year. This result has been confirmed through both PSI InSAR and SBAS InSAR techniques, which are both in good agreement with historical GPS results from 1998 to 2001 [Mann and Freymueller, 2003]. This suggests that the volcano pressure source underneath the Fisher caldera is stable and causes continuous deformation. Mann and Freymueller [2003] suggest that the subsidence and contraction over the center of the Fisher caldera can be explained by a historical magma both degassing and cooling, which can be modeled by rectangular dislocation source at shallow depth. Our results support this conclusion.

Shishaldin Volcano has a more active eruption record compared to the other two volcanoes discussed above, however with a puzzling lack of deformation. A previous attempt to use the InSAR technique at Shishaldin volcano was not able to detect significant deformation [Moran *et al.*, 2006], which suggests a fast re-filling system and shallow magma source. However, the deformation detected in regions east of Shishaldin (approx. 15 km away) and north of Fisher caldera (the Tugamak range, approx. 30 km away) contain some deformation signals, also confirmed by GPS measurements after 2008 [UNAVCO, 2013]. They are also temporally correlated to Shishaldin eruption. At the current time, we do not have enough information to conclude if these signals are due to a deep volcanic pressure source underneath Shishaldin, nor do we have enough information to explain the absence of a deformation signal around Shishaldin peak.

3.8 Summary and Conclusions

We present a study that is using advanced satellite radar interferometry methods for long-term volcano monitoring at Unimak Island, Alaska. An advanced time series InSAR technique was developed by integrating an external numerical weather prediction model with PSI Interferometry techniques to optimally mitigate atmospheric artifacts. The PSI reconstructed velocity map was compared to SBAS processed results, and the PSI deformation time series were compared to both historical and current GPS time series measurements. The results demonstrate that this InSAR method is able to mitigate atmospheric signals with high quality and improve the quality of the reconstructed deformation time series.

The PSI-derived deformation fields are used for geophysical interpretation for three active volcanoes, namely Westdahl, Fisher and Shishaldin. The conclusions listed below can be made from our quantitative study.

- (1) Westdahl volcano is still inflating but at a lower rate than in the period before 2001. The study confirms the magma source location suggested by a previous GPS study [Mann and Freymueller, 2003] and is approximately 3.5 km north of Westdahl peak. Its magma source can be described by a Mogi model, whose volume change is varying in an exponentially decaying manner. Although this confirms the descriptions made in previous literature [Lu *et al.*, 2003], our study hypothesizes that a single exponential function is insufficient to model its volume change through the full time span after its eruption in 1991 through the end of our study period in 2010.
- (2) Fisher Caldera continues subsiding with a linear and constant rate since the 1990s that is caused by its historical magma source degassing.
- (3) Shishaldin volcano shows no observable deformation signals near its peak. However, deformation fields more than 30 km away from Shishaldin peak on the Tugamak range and approx. 15 km towards the east of Shishaldin are observed. However, the source of those movements is not clear. Further studies on Shishaldin and these regions are suggested.

3.9 Acknowledgement

This work was supported by the NASA Headquarters under the NASA Earth and Space Science Fellowship Program - Grant NNX10AO70H. ASAR data is provided by European Space Agency.

3.10 References

- Alaska Volcano Observatory, (2009), <https://www.avo.alaska.edu/>
- Buurman, H. (2013), Volcano Seismicity in Alaska, University of Alaska Fairbanks.
- Dvorak, J. J., and A. T. Okamura (1987), A hydraulic model to explain variations in summit tilt rate at Kilauea and Mauna Loa volcanoes, in *Volcanism in Hawaii*, edited by W. T. L. Decker R.W., Stauffer P. H., U.S. Geological Survey, Washington.
- Dvorak, J. J., and D. Dzurisin (1997), Volcano geodesy: The search for magma reservoirs and the formation of eruptive vents, *Review of Geophysics*, 35(3), 343-384.
- Dzurisin, D. (2003), A comprehensive approach to monitoring volcano deformation as a window on the eruption cycle (vol 41, pg 1001 , 2003), *Review Geophysics*, 41(2).
- Dzurisin, D. (2007), *Volcano deformation : geodetic monitoring techniques*, 441 p. pp., Springer-Praxis Berlin; New York; Chichester, UK.
- Ferretti, A., C. Prati, and F. Rocca (2000), Nonlinear subsidence rate estimation using permanent scatterers in differential SAR interferometry, *IEEE Transactions on Geoscience and Remote Sensing*, 38(5), 2202-2212.
- Fournier, T., J. Freymueller, and P. Cervelli (2009), Tracking magma volume recovery at Okmok volcano using GPS and an unscented Kalman filter, *Journal of Geophysical Research: Solid Earth*, 114.
- Freymueller, J., and J. Beavan (1999), Absence of strain accumulation in the western Shumagin segment of the Alaska subduction zone, *Geophysical Research Letters*, 26(21), 3233-3236.
- Gong, W., and F. J. Meyer (2012), Optimized filter design for irregular acquired data stack in persistent scatterers synthetic aperture radar interferometry, paper

- presented at 2012 IEEE International Geoscience and Remote Sensing Symposium Munich, Germany, 22-27 July 2012.
- Gong, W., F. J. Meyer, and S. Liu (2011), Numerical Weather Model Assisted Time Series InSAR Processing for Geophysical Application, paper presented at ESA FRINGE Workshop, European Space Agency Frascati, Italy, 19-23 September
- Gong, W., F. J. Meyer, P. Webley, and Z. Lu (2010), Tropospheric correction of InSAR time-series with the weather research forecasting model: an application to volcanic deformation monitoring, paper presented at American Geophysical Union, Fall Meeting 2010, San Francisco.
- Gong, W., F. J. Meyer, S. Liu, and R. Hanssen (manuscript in preparation), Robust Atmospheric Filtering of InSAR Data based on Numerical Weather Prediction Models.
- Hanssen, R. (2001), *Radar Interferometry: Data Interpretation and Error Analysis*, 1 ed., Kluwer Academic Publishers, Netherlands.
- Hooper, A., P. Segall, and H. Zebker (2007), Persistent scatterer interferometric synthetic aperture radar for crustal deformation analysis, with application to Volcán Alcedo, Galápagos, *J. Geophys. Res.*, 112(B7), B07407.
- Hooper, A., D. Bekaert, K. Spaans, and M. Arıkan (2012), Recent advances in SAR interferometry time series analysis for measuring crustal deformation, *Tectonophysics*, 514–517(0), 1-13.
- Kampes, B. (2006), *Radar interferometry: persistent scatterer technique*, 211 pp., Springer, Dordrecht, the Netherlands.
- Lee, C. W., Z. Lu, H. S. Jung, J. S. Won, and D. Dzurisin (2010), Surface deformation of Augustine Volcano, 1992–2005, from multiple-interferogram processing using a refined small baseline subset (SBAS) interferometric synthetic aperture radar (InSAR) approach, in *The 2006 eruption of Augustine Volcano, Alaska: U.S. Geological Survey Professional Paper 1769*.
- Lu, Z. (2007), InSAR imaging of volcanic deformation over cloud-prone areas - Aleutian Islands, *Photogrammetric Engineering & Remote Sensing*, 73(3), 245-257.

- Lu, Z., and J. Freymueller (1998), Synthetic aperture radar interferometry coherence analysis over Katmai volcano group, Alaska, *Journal of Geophysical Research*, 103(B12), 29887-29894.
- Lu, Z., T. Masterlark, D. Dzurisin, R. Rykhus, and C. Wicks, Jr. (2003), Magma supply dynamics at Westdahl volcano, Alaska, modeled from satellite radar interferometry, *Journal of Geophysical Research*, 108(B7), 2354.
- Lu, Z., C. Wicks, D. Dzurisin, W. Thatcher, J. T. Freymueller, S. R. McNutt, and D. Mann (2000), Aseismic inflation of Westdahl Volcano, Alaska, revealed by satellite radar interferometry, *Geophysical Research Letters*, 27(11), 1567-1570.
- Mann, D., and J. Freymueller (2003), Volcanic and tectonic deformation on Unimak Island in the Aleutian Arc, Alaska, *Journal of Geophysical Research*, 108(B2), 2108.
- McTigue, D. F. (1987), Elastic Stress and Deformation near a Finite Spherical Magma Body - Resolution of the Point-Source Paradox, *Journal of Geophysical Research*, 92(B12), 12931-12940.
- Mogi, K. (1958), Relations between the eruptions of various volcanoes and the deformations of the ground surfaces around them, paper presented at Bulletin of the Earthquake Research Institute, Earthquake Research Institute, University of Tokyo.
- Moran, S. C., O. Kwoun, T. Masterlark, and Z. Lu (2006), On the absence of InSAR-detected volcano deformation spanning the 1995–1996 and 1999 eruptions of Shishaldin Volcano, Alaska, *Journal of Volcanology and Geothermal Research*, 150(1–3), 119-131.
- Neal, C. A., R. G. McGimsey, J. Dixon, and D. Melnikov (2005), 2004 Volcanic Activity in Alaska and Kamchatka: Summary of Events and Response of the Alaska Volcano Observatory, USGS. <http://pubs.usgs.gov/of/2005/1308/#>.
- Segall, P. (2010), *Earthquake and volcano deformation*, xxiii, 432 p., [438] p. of plates pp., Princeton University Press, Princeton, N.J.

- Shanker, P., F. Casu, H. A. Zebker, and R. Lanari (2011), Comparison of Persistent Scatterers and Small Baseline Time-Series InSAR Results: A Case Study of the San Francisco Bay Area, *IEEE Geoscience and Remote Sensing Letters*, 8(4), 592-596.
- Skamarock, W. C., J. B. Klemp, J. Dudhia, D. O. Gill, M. Barker, K. G. Duda, X. Y. Huang, W. Wang, and J. G. Powers (2008), A description of the Advanced Research (WRF) Version 3 *Rep.*, pp82-83 pp, National Center for Atmospheric Research.
- UCAR (2013), NCEP FNL Operational Model Global Tropospheric Analyses, continuing from July 1999, edited, <http://rda.ucar.edu/datasets/ds083.2/>.
- UNAVCO (2013), GNSS Data Archive Interface Version 2 (DAI v2),, <http://facility.unavco.org/data/>.
- Wood, C. A., and J. Kienle (1990), *Volcanoes of North America : United States and Canada*, 354 p. pp., Cambridge University Press, New York.

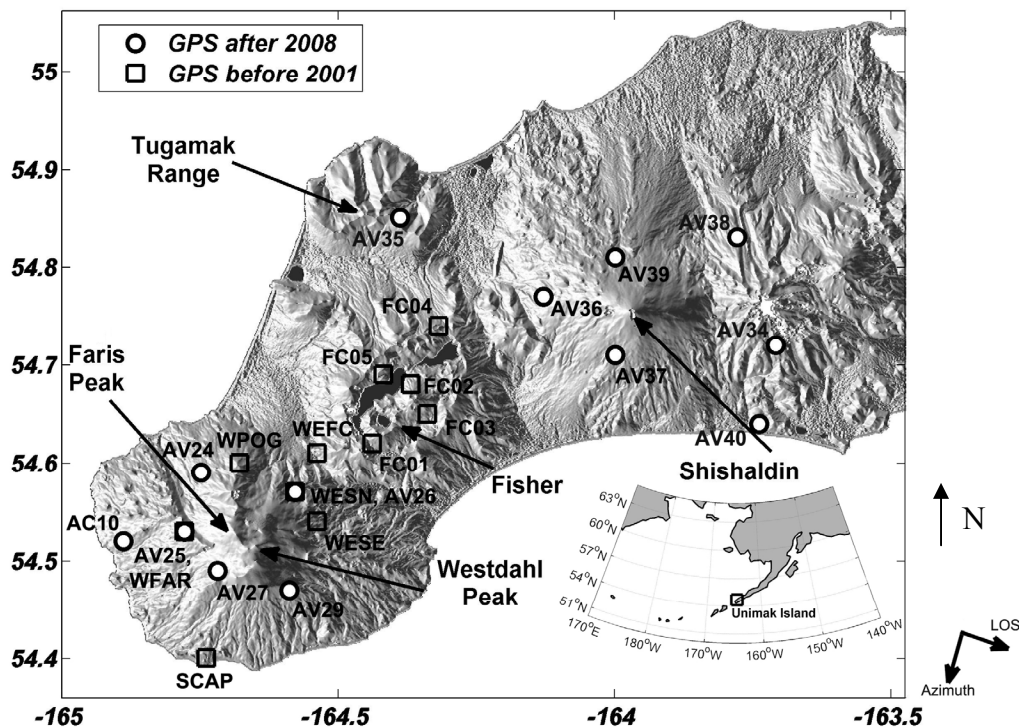


Figure 3.1 The location of the three studied volcanoes, Westdahl, Fisher and Shishaldin, and historical/current GPS sites in Unimak Island with shade relief topographic map as background. The satellite line-of-sight (LOS) direction and flight direction (azimuth) are denoted on the middle-bottom. The GPS observation sites between 1998 and 2001 [Mann and Freymueller, 2003] are denoted by black squares from south to north they are SCAP, WFAR, WESE, WESN, WPOG, WEFC, FC01, FC03, FC02, FC05, FC04; the ones that have records after 2008 are denoted by black circles with white filling, from the west to the east circle markers filled with white color denote GPS sites AC10, AV25, AV24, AV27, AV29, AV26, AV35, AV36, AV39, AV37, AV38, AV40 and AV34.

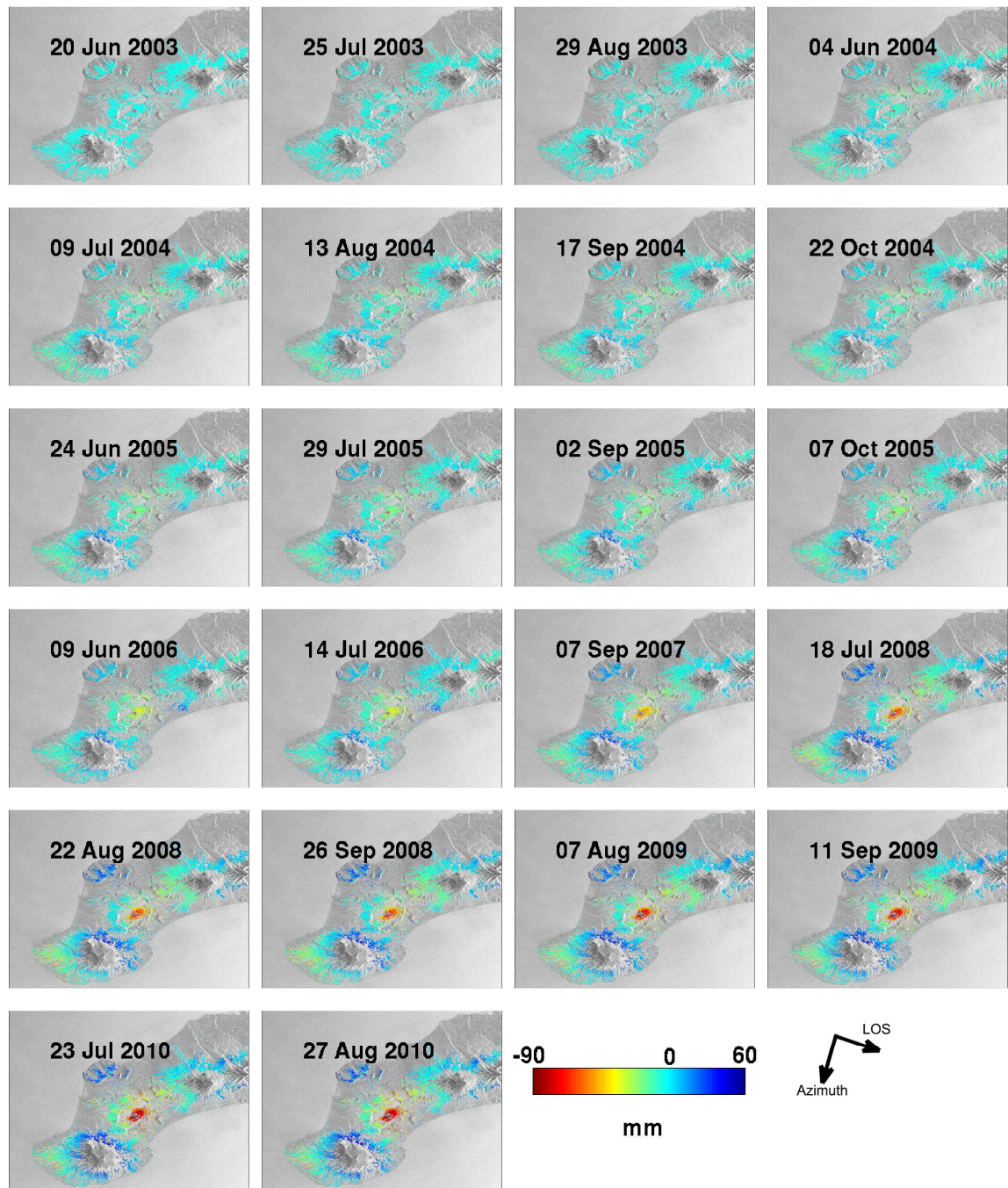
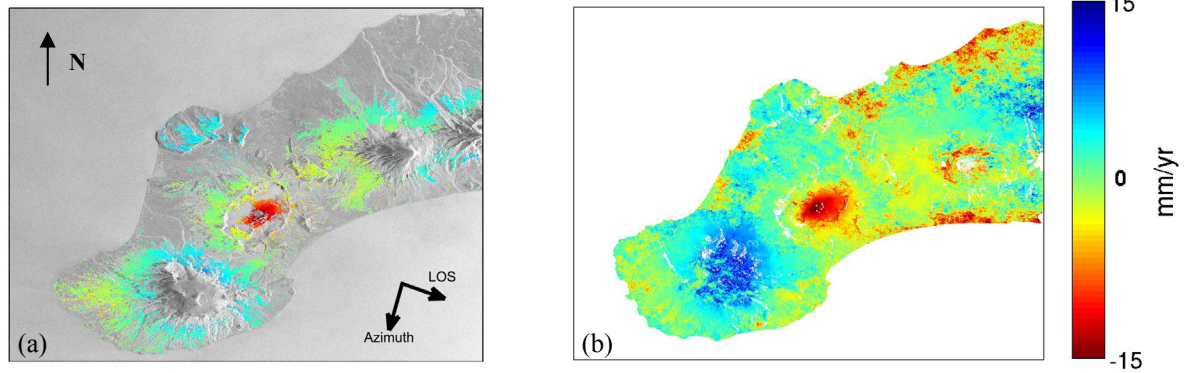


Figure 3.2 Deformation time series from 2003 to 2010, reconstructed from PSI data processing, all the values referenced to the average deformation of the all point stack.



(a) velocity map from PSI processing

(b) velocity map from SBAS processing

Figure 3.3 Velocity map provide from both PSI and SBAS method (x-axis-right point to east; y-axis-up to north)

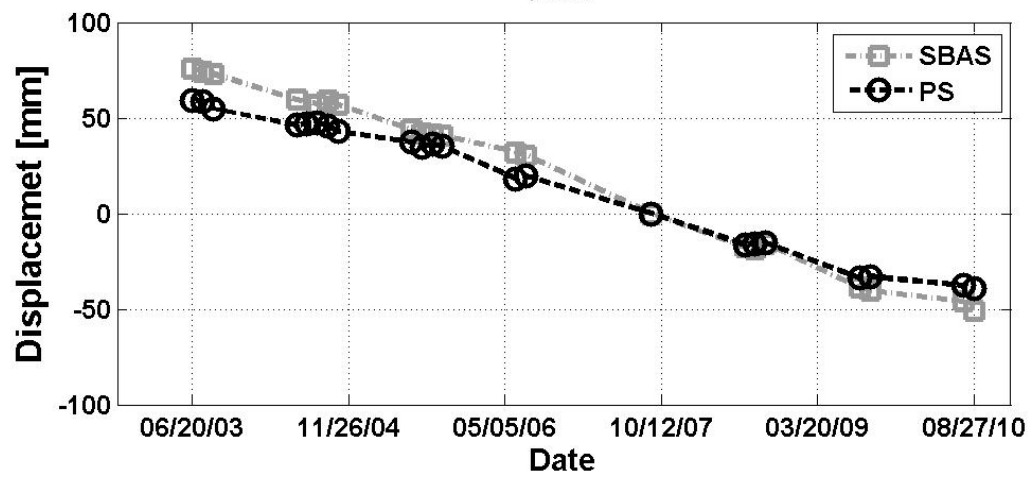


Figure 3.4 Subsidence (displacement in millimeters) observed in the center of Fisher caldera, from 2003 to 2010; SBAS is the result derived from Small Baseline Subset method and PS is the one from Persistent Scatterer Interferometry.

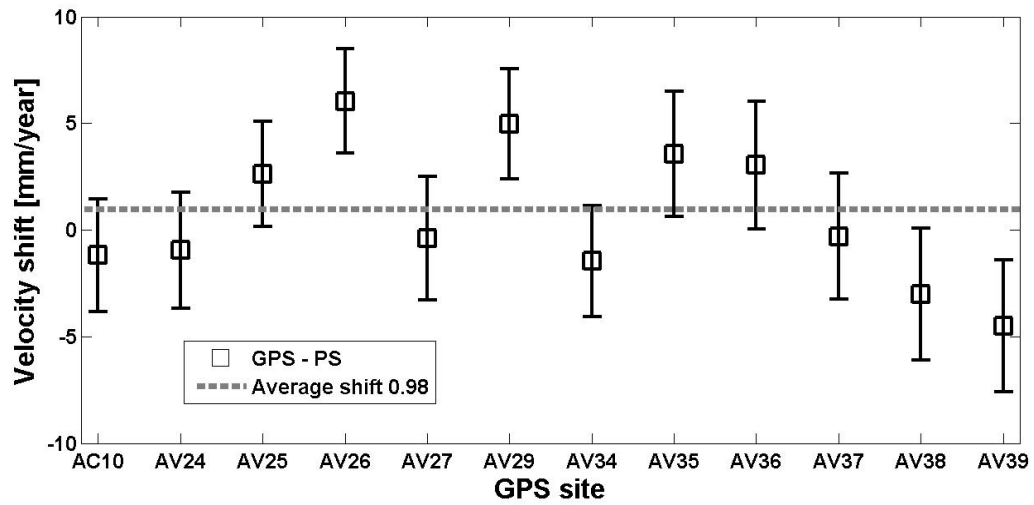


Figure 3.5 Shift in velocity (mm/year) computed from GPS and PSI with different spatial reference frame.

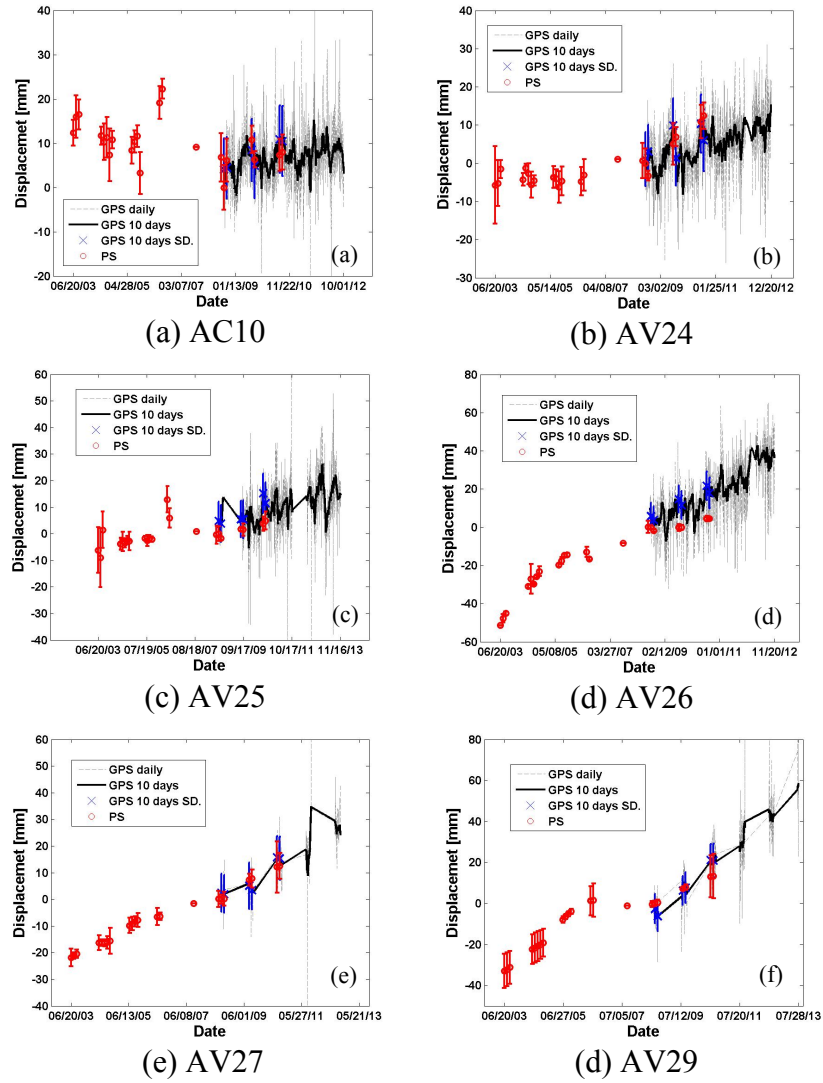


Figure 3.6 Comparison of GPS and PSI LOS motion time series measurements around Westdahl; x-axes date format is mm/dd/yyyy.

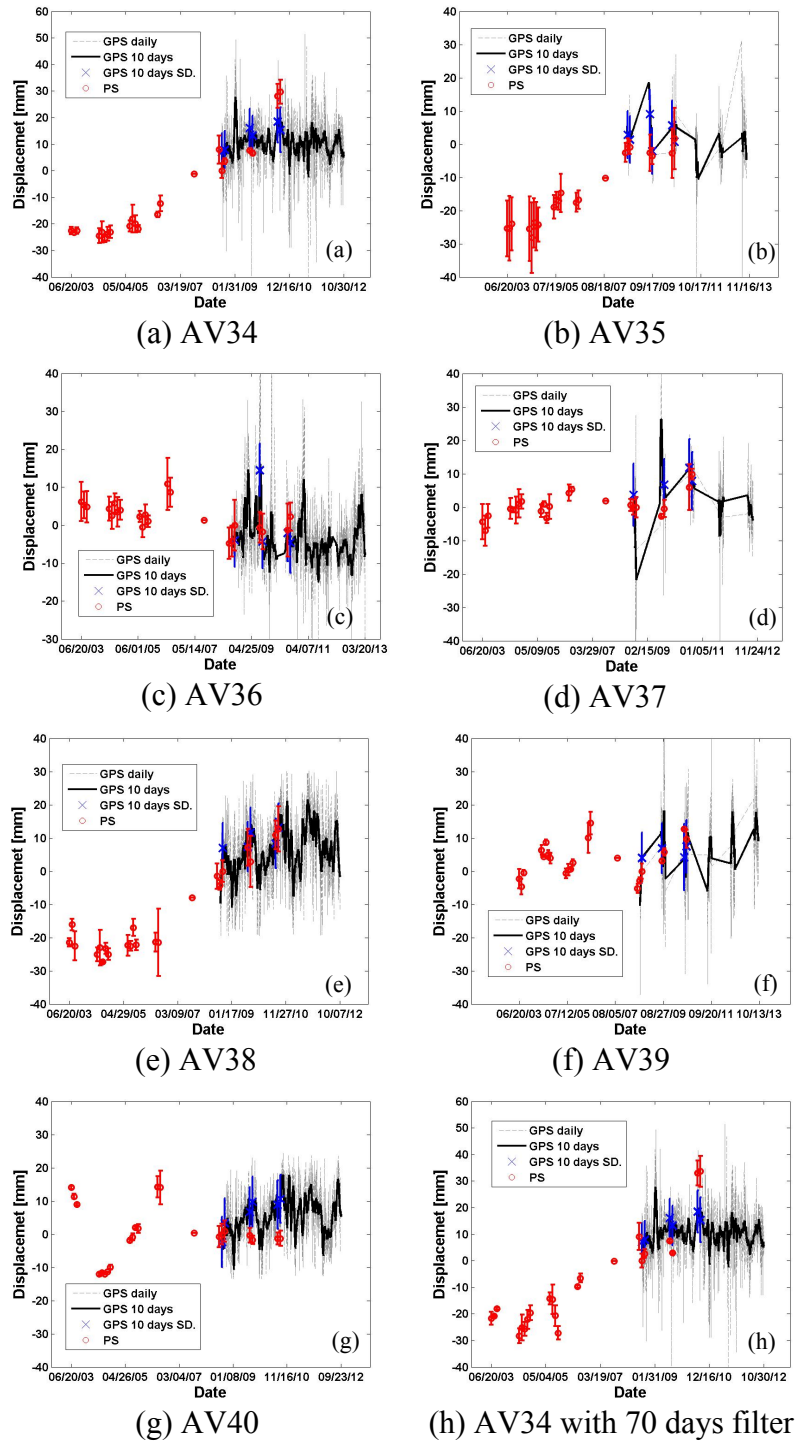


Figure 3.7 Comparison of GPS and PSI LOS motion time series measurements close to Shishaldin; x-axes date format is mm/dd/yyyy.

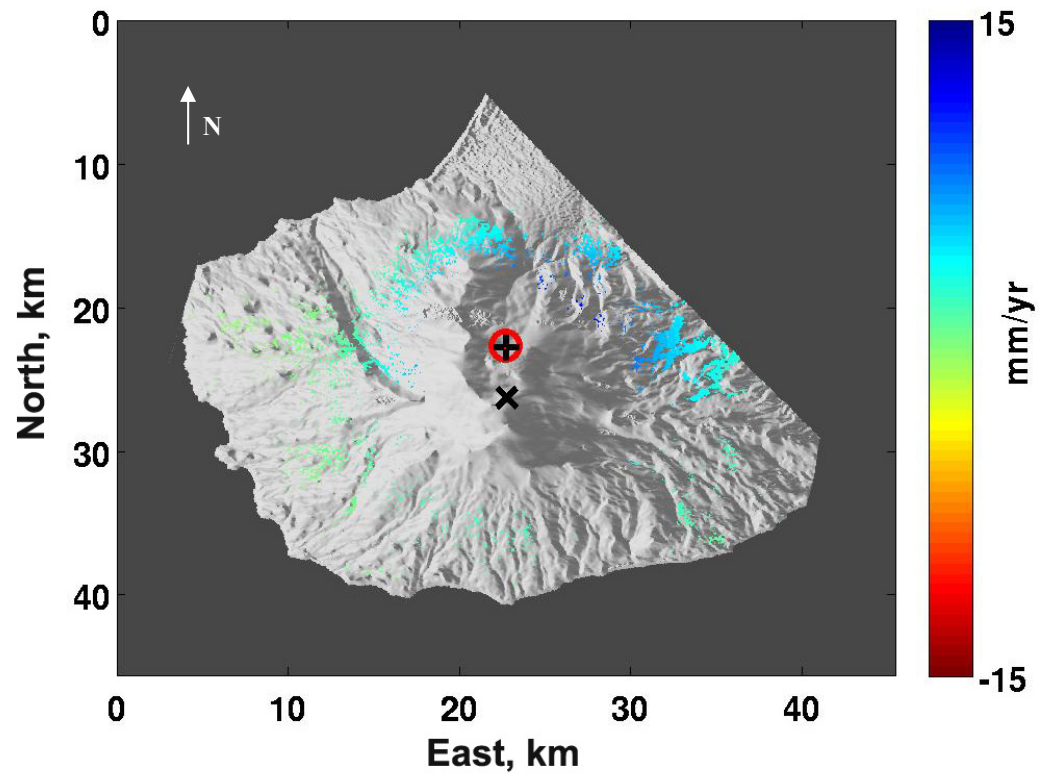
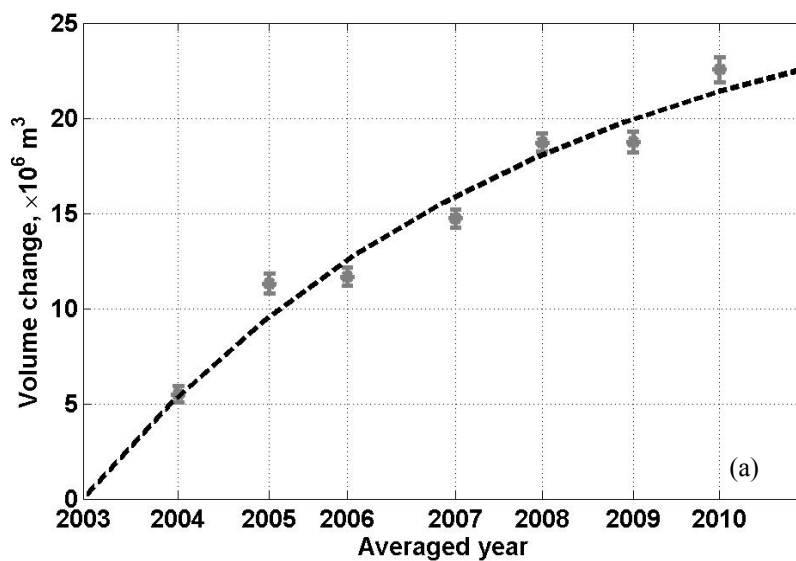
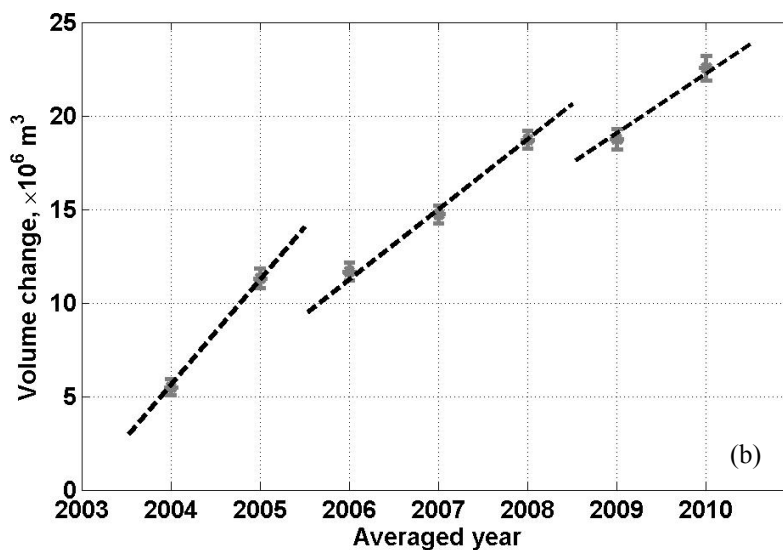


Figure 3.8 The result of point source model inversion results: the horizontal location and predicted annual inflation is plotted over background shaded relief topography; x (point to south) and y (point to east) axes are in kilometers with origin at upper left; the displacement references to origin.



(a) Modeling of cumulative volume change with exponential decaying function



(b) Modeling of cumulative volume change with step linear function

Figure 3.9 Volume change estimates and temporal model; x-axes are the averaged time interval within every year and reference July 25, 2003. The dashed line is the best fit of exponential decay model and step linear model

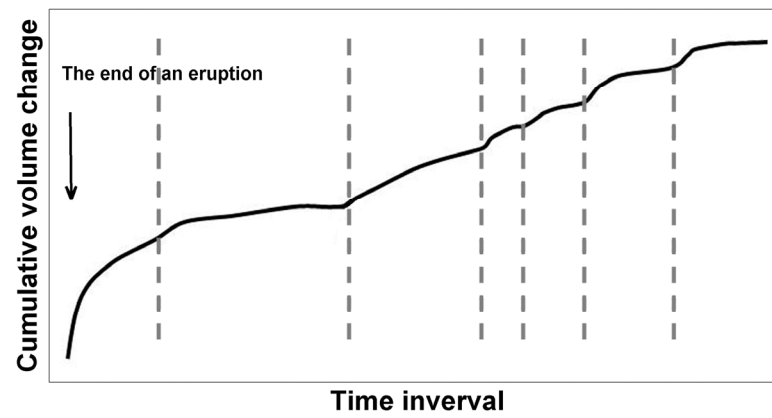


Figure 3.10 Magma refilling processing after an eruption of Westdahl volcano. Black curve sketch of the overall cumulative volume change over time. The dashed gray lines denote the rest period in magma refilling that leads to a change of ΔV velocity.

Table 3.1 Single master interferogram information

No.	Date	B_{\perp} [m]	B_t [day]	f_{DC} [Hz]	var_{aps} [rad ²]
1	June 20, 2003	-660	-1540	294	0.58
2	July 25, 2003	-775	-1505	254	0.09
3	Aug. 29, 2003	-258	-1470	218	0.62
4	June 04, 2004	-69	-1190	179	0.32
5	July 09, 2004	-521	-1155	185	0.30
6	Aug. 13, 2004	-626	-1120	167	10.57
7	Sep. 17, 2004	427	-1085	187	0.26
8	Oct. 22, 2004	-94	-1050	235	1.29
9	June 24, 2005	106	-805	160	0.29
10	July 29, 2005	-56	-770	211	0.21
11	Sep. 02, 2005	405	-735	211	1.14
12	Oct. 07, 2005	-687	-700	258	4.00
13	June 09, 2006	-674	-455	207	0.52
14	July 14, 2006	342	-420	224	0.14
15	Sep. 07, 2007 (master)	0	0	0	0
16	July 18, 2008	-261	315	229	0.24
17	Aug. 22, 2008	-58	350	223	0.46
18	Sep. 26, 2008	-728	385	205	0.23
19	Aug. 07, 2009	-404	700	222	0.58
20	Sep. 11, 2009	186	735	219	0.13
21	July 23, 2010	-721	1050	229	0.82
22	Aug. 27, 2010	-373	1085	228	0.54

Table 3.2 GPS velocity (mm/year) in LOS direction during 1998 to 2001 and PSI velocity during 2003 to 2010; ^a GPS LOS uncertainty is computed from its 3D uncertainties in one sigma; ^b PSI uncertainty is the standard deviation of the velocities at selected points.

Site	Lat.	Lon.	GPS V-LOS ^a	PSI V-LOS ^b	PSI V-LOS corrected	No. PSI	Mean distance [m]
SCAP	54.4	-164.74	5.3 ± 4.7	1.2 ± 0.5	1.3 ± 0.5	3	131
WESE	54.54	-164.54	5.0 ± 5.6	4.8 ± 0.1	4.9 ± 0.1	3	246
WESN	54.57	-164.58	19.9 ± 5.6	5.4 ± 0.5	5.4 ± 0.5	4	216
WPOG	54.6	-164.68	2.2 ± 3.7	1.3 ± 0.2	1.4 ± 0.2	2	430
WFAR	54.53	-164.78	1.3 ± 3.7	-0.3 ± 0.6	-0.2 ± 0.6	2	99
WEFC	54.61	-164.54	10.3 ± 3.8	2.5 ± 0.5	2.6 ± 0.5	2	235
FC01	54.62	-164.44	-3.8 ± 5.6	-1.9 ± 0.6	-1.8 ± 0.6	3	219
FC02	54.68	-164.37	-11.6 ± 3.8	-11.7 ± 0.6	-11.6 ± 0.6	4	33
FC03	54.65	-164.34	-11.1 ± 2.8	-10.7 ± 0.7	-10.6 ± 0.7	5	138
FC04	54.74	-164.32	-2.8 ± 3.8	-3.6 ± 0.4	-3.5 ± 0.4	4	236
FC05	54.69	-164.42	6.6 ± 4.7	-2.9 ± 0.03	-2.8 ± 0.03	2	74

Table 3.3 Statistical analysis of the displacement residuals from PBO GPS and PSI in the overlap dates; residuals computed from GPS minus PSI. Locations of GPS sites can be found in Figure 3.1.

Site name	Lat.	Long.	Height [m]	Points No.	Mean distance [m]	Residual offset [mm]		Residual SD [mm]	
						Opt. Win.	70days	Opt. Win.	70days
AC10	54.52	-164.89	170.45	3	115.61	0.77	0.76	2.74	2.78
AV24	54.59	-164.75	481.72	4	60.77	0.08	0.28	4.78	4.98
AV25	54.53	-164.78	651.94	3	78.19	6.00	5.87	6.55	6.43
AV26	54.57	-164.58	577.59	2	103.23	11.46	11.67	12.26	12.44
AV27	54.49	-164.72	977.91	3	413.48	0.67	0.13	3.01	3.46
AV29	54.47	-164.59	971.88	2	887.67	0.88	0.59	5.40	5.40
AV34	54.72	-163.71	636.38	2	366.69	0.41	-0.27	8.95	11.56
AV35	54.85	-164.39	646.98	4	357.12	4.30	4.32	6.12	6.36
AV36	54.77	-164.13	648.40	3	36.02	0.20	-0.04	7.70	7.84
AV37	54.71	-164.00	796.03	3	312.40	3.64	3.84	5.06	5.97
AV38	54.83	-163.78	492.29	3	29.58	2.74	2.23	5.14	4.91
AV39	54.81	-164.00	797.38	2	522.42	-0.71	-1.93	5.16	6.28
AV40	54.64	-163.74	413.94	2	589.40	6.79	6.83	8.56	9.36

Table 3.4 Time series of volcano source model inversion result from 2004 to 2010 with fixed horizontal location only; sd. denotes Standard deviation; Δ Volume denotes volume change; EW denotes East-West direction; SN denotes South-North direction.

	2004	2005	2006	2007	2008	2009	2010
Depth (km)	10.70	5.00	5.27	7.88	8.67	8.81	9.64
Depth sd. (km)	0.92	0.31	0.30	0.28	0.25	0.28	0.29
Δ Volume (10^6 m^3)	10.62	9.34	9.85	17.61	24.86	26.21	36.47
Δ Volume sd. (10^6 m^3)	1.73	0.24	0.26	0.70	0.93	1.10	1.66
Static-residual (mm)	-7.62	0.58	7.83	1.24	-1.89	2.87	16.46
EW slope (mm/km)	0.24	0.00	-0.16	0.16	0.50	0.27	-0.25
SN slope (mm/km)	0.18	0.02	-0.17	-0.11	-0.22	-0.24	-0.37
Center point residual (mm)	2.08	0.99	0.38	2.53	4.50	3.59	2.43

Table 3.5 Time series of volcano source model second inversion with fixed depth at 7 *km* and fixed horizontal location; sd. denotes Standard deviation; Δ Volume denotes volume change; EW denotes East-West direction; SN denotes South-North direction.

	2004	2005	2006	2007	2008	2009	2010
Δ Volume (10^6 m^3)	5.49	11.31	11.68	14.73	18.72	18.75	22.55
Δ Volume sd. (10^6 m^3)	0.43	0.51	0.49	0.46	0.48	0.54	0.65
Static-residual (mm)	-9.26	1.77	8.93	-0.08	-3.49	-0.19	11.19
EW slope (mm/km)	0.27	0.01	-0.15	0.18	0.50	0.31	-0.17
SN slope (mm/km)	0.23	-0.04	-0.22	-0.06	-0.15	-0.14	-0.21
Center point residual (mm)	2.10	0.98	0.38	2.54	4.51	3.62	2.49

Chapter 4 Conclusion and Future Work

4.1 Conclusions

Motivated by the need to improve current radar remote sensing techniques, especially radar interferometry (InSAR), for long term monitoring and geodetic studies, this study focused on the development of InSAR techniques and geophysical applications on *optimizing the quantity and quality of deformation signals extracted from InSAR time series stacks to facilitate volcano monitoring and the study geophysical signatures*. Specifically, the focus was on developing methods of mitigating atmospheric artifacts in interferograms by combining auxiliary atmospheric delay maps derived by Numerical Weather Prediction (NWP) models with advanced time-series InSAR processing scheme models for volcano long term monitoring.

In the first chapter, statistics produced by the atmospheric delay maps have been studied quantitatively and extensively. NWP models are widely seen as a promising tool for the mitigation of atmospheric delays as they can provide knowledge of the atmospheric conditions at SAR imageries acquisition times. However, there was an absence of thorough statistical analysis of using NWP productions in radar signal correction. The first chapter provided a quantitative analysis of the accuracy of operational NWP products for signal delay correction in satellite radar geodetic remote sensing. The study focused on the temperate, subarctic and Arctic climate regions due to a prevalence of relevant geophysical signals in these areas. The operational High Resolution Rapid Refresh over the Alaska region (HRRR-AK) model [ARSC, 2012], run by the Arctic Region Supercomputing Center (ARSC), was used and evaluated. Five test sites were selected over Alaska (AK), USA, covering a wide range of climatic regions that are commonly encountered in high latitude regions. The performance of the HRRR-AK NWP model for explicitly correcting absolute atmospheric range delays of radar signals was assessed by comparing HRRR-AK simulations to radiosonde observations. The predicted accuracy of the HRRR-AK in atmospheric delay corrections was derived and calculated based on error propagation theory. From this study, it was concluded that

the HRRR-AK operational products are a good data source for correcting signal delays of spaceborne geodetic radar observations, if the geophysical signal to be observed is larger than 20mm. It was also concluded that these corrections can be performed with a statistically identical performance across all seasons. The residual errors after delay correction are largely due to the uncertainties of predicted atmospheric water vapor concentrations.

In the second chapter, in order to detect subtle ground deformation, an advanced method was developed to find robust solutions to mitigate atmospheric phase delay distortions in SAR interferogram time series. NWP were studied from a statistical point of view by analyzing the capability of the NWP in providing realistic information of atmospheric statistical properties. This was accomplished by comparing NWP derived and InSAR extracted atmospheric phase screens. The two main findings of this study include (1) NWP are able to robustly predict statistical properties of atmospheric phase screens and (2) NWP underestimate these statistical properties by a scaling factor that depends on the area's surface topography but not on its climatic conditions. Based on these findings, a new concept for atmospheric mitigation was built that is using NWP-derived statistical parameters to condition the design of an optimal atmospheric phase filter in time series InSAR processing. The proposed scheme was tested via synthetic data sets and its efficiency and convergent dependence was evaluated through Monte Carlo experiments, both of which suggest a reliable performance of the algorithm. The algorithm's scheme is especially suitable for the applications with limited prior knowledge of the deformation signal.

In the final chapter, seven years of satellite radar images over Unimak Island, Alaska, have been processed using advanced Persistent Scatterer Interferometry (PSI) techniques. The data processing integrated the Persistent Scatterer Interferometry method and auxiliary numerical predicted radar signal delay statistics to optimally reconstruct the deformation history. The study was focused on characterizing geophysical signatures over three active volcanoes, Westdahl, Fisher and Shishaldin on Unimak Island, all of which have been actively erupting or producing ground motion within recent decades.

Comparisons were made between the reconstructed deformation time series and GPS measurements (historical records from 1998 to 2001 [*Mann and Freymueller, 2003*] and current records from 2008 to 2010 [*UNAVCO, 2013*]). They have been used together for interpretation of geophysical activity on Unimak Island. The result shows that the derived deformation field series over Unimak Island matches well with the GPS geodetic records (see Section 3.5.1).

Particularly, the volcano source model study was implemented for Westdahl to determine the model parameters of a Mogi source model. The result suggests that the horizontal location of the source center is approximately 3.5 km north of Westdahl peak with a depth of about 7.5 km below sea level, which agrees with the GPS result from *Mann and Freymueller [2003]* from 1998 to 2001. The volume change rate continued to slow down over time and is lower than that from previous studies for earlier periods [*Lu et al., 2000; Mann and Freymueller, 2003*]. The volume change time series fits well the exponential decaying model of volume change as proposed in a previous InSAR study [*Lu et al., 2003*], but a single exponential decay model cannot explain all time periods. The volume change at the Westdahl after its eruption in 1991 can be described through multiple exponential decaying functions. The Fisher caldera is deforming consistently and linearly in time. It has been subsiding with a maximum detected deformation velocity of approx. 16 mm/year in the LOS direction. Such activity is triggered by historical magma source degassing of its thermal system [*Mann and Freymueller, 2003*]. There was no evident deformation found near Shishaldin peak. Deformation signals east of Shishaldin peak and the Tugamak Range were detected, but the source of those movements is not clear.

It is my hope that my research will not only contribute to the development of satellite SAR time series data processing, but also contribute to the long term monitoring of volcanoes in Alaska and to a better understanding of the processes of arc volcanism.

4.2 Future Work and Improvements

I can see several potential topics for future work and new research avenues based on my thesis work, as listed below.

(1) *Conduct a further study on integrating operational Numerical Weather Prediction (NWP) products into the optimized atmospheric phase filter (OAPF) developed in Chapter 2.* The NWP products studied in Chapter 2 were customized with a user-defined lateral spatial resolution of 1 km. If operational NWP products can be used directly, it will simplify the procedure for obtaining atmospheric delay statistics, e.g. no special knowledge would be required in running numerical weather forecast models, and the computational cost for creating atmospheric information could be reduced. However, the resolution of current operational NWP products is coarser than the customized runs used in the thesis. Hence, their performance needs to be assessed. For instance, current high resolution operational NWP products can provide atmospheric conditions hourly with a 3 km lateral resolution, e.g. the High-Resolution Rapid Refresh (HRRR) [NOAA, 2012] for lower 48 US and HRRR for Alaska (HRRR-AK) [ARSC, 2012], used in Chapter 1. A preliminary study by *Gong et al.* [2011] showed that user-customized NWP products with 3 km spatial resolution were able to satisfy the linear correlation between NWP-provided and InSAR-derived atmosphere spatial variance described in Chapter 2. Thus, a further in-depth study on integrating current operational NWP products with similar resolution condition into the OAPF is necessary. This study would provide the potential to develop a prototype time series InSAR (TS-InSAR) plug-in for atmospheric correction that can be directly used by end-users for various purposes, without requiring extensive experience in TS-InSAR data processing and/or weather modeling.

(2) *Apply the OAPF theory to the other TS-InSAR approaches.* In the thesis, the OAPF was applied and tested with one of the TS-InSAR methods, the Persistent Scatterer SAR Interferometry (PSI) method. The OAPF algorithm can be modified to assist other deformation model-free TS-InSAR approaches, such as Small Baseline Subset (SBAS) InSAR methods. SBAS approaches have been applied to diverse applications and rely on different ground resolution elements as compared to PSI methods [*Hooper et al.*, 2012]. The choice of PSI or SBAS is based on the conditions of ground scatterers in the study area, the number, type and distribution of available data sets, and the application purpose.

Hence, integrating OAPF into current SBAS would potentially extend the usefulness of the OAPF and improve the current SBAS algorithms.

(3) *Integrate the GPS measurements and PSI results for the overlapping time period, 2008 to 2010 for a joint source model inversion at Westdahl volcano.* A proper weighting scheme of the GPS and PSI deformation data needs to be determined for a joint inversion of these two data sets. For example, researchers have optimally combined GPS and InSAR measurements by considering both the spacing of GPS networks and deformation signal characteristics [Wei *et al.*, 2010]. The GPS measurements contain three dimensional deformation measurements at a limited number of locations, while InSAR measurements provide deformation signals at coherent targets with a much higher spatial density, but in the line-of-sight direction only. Hence, I expect a joint inversion would improve the accuracy of volcanic source parameter estimation of Westdahl. For instance, the inversion would rely less on the initial bounds setting of the ramp parameters, given InSAR measurements are contaminated by slope-ramp residuals while GPS records are not.

(4) *A further study on the region east of Shishaldin volcano and the Tugamak range is necessary.* As concluded in Chapter 3, the source of the deformation in these two regions is unclear. Although detected deformation signals appear to be correlated in time with the Shishaldin eruption in 2004, the region around Shishaldin peak lacks observable deformation signals. Given the high activity Shishaldin volcano, e.g. with 1 eruption (in 2004) and 9 periods of lesser activity since 2000 [Alaska Volcano Observatory, 2009], a continuing study combining all available geodetic measurements (e.g., from current SAR missions and continuous GPS) and other geological or geophysical observations, e.g. the seismic data, is needed.

4.3 References

Alaska Volcano Observatory, (2009), <https://www.avo.alaska.edu/>

ARSC (2012), ARSC High Resolution Rapid Refresh (HRRR), Arctic Region Supercomputing Center <http://weather.arsc.edu/HRRR/>

- Gong, W., F. Meyer, and S. Liu (2011), Numerical Weather Model assisted time series InSAR processing for geophysical application, paper presented at ESA FRINGE Workshop, European Space Agency Frascati, Italy, 19-23 September
- Hooper A., D. Bekaert, K. Spaans, M. Arıkan (2012), Recent advances in SAR interferometry time series analysis for measuring crustal deformation, *Tectonophysics*, Volumes 514–517, pp1-13.
- Lu, Z., T. Masterlark, D. Dzurisin, R. Rykhus, and C. Wicks, Jr. (2003), Magma supply dynamics at Westdahl volcano, Alaska, modeled from satellite radar interferometry, *Journal of Geophysical Research*, 108(B7), 2354.
- Lu, Z., C. Wicks, D. Dzurisin, W. Thatcher, J. T. Freymueller, S. R. McNutt, and D. Mann (2000), Aseismic inflation of Westdahl Volcano, Alaska, revealed by satellite radar interferometry, *Geophysical Research Letter*, 27(11), 1567-1570.
- Mann, D., and J. Freymueller (2003), Volcanic and tectonic deformation on Unimak Island in the Aleutian Arc, Alaska, *Journal of Geophysical Research*, 108(B2), 2108.
- NOAA (2012), The High-Resolution Rapid Refresh (HRRR), <http://ruc.noaa.gov/hrrr/>
- UNAVCO (2013), GNSS Data Archive Interface Version 2 (DAI v2), <http://facility.unavco.org/data>
- Wei, M., Sandwell, D., and Smith-Konter, B., 2010, Optimal combination of InSAR and GPS for measuring interseismic crustal deformation, *Advances in Space Research*, v. 46, no. 2, p. 236-249.